Study of Integrated Optical Phased Array System

by

Da Chuan Wu

A dissertation submitted in partial fulfillment
of the requirements for the degree of
Doctor of Philosophy
(Electrical, Electronics, and Computer Engineering)
in the University of Michigan-Dearborn
2023

Doctoral Committee:

Professor Yasha Yi, Chair
Professor Selim Awad
Associate Professor Joe Fu-Jiou Lo
Professor Weidong Xiang

Acknowledgements

Earning a Ph. D degree is always a tough journey for everyone. During my Ph. D, I received a lot of support from many people. I want to say thank you to everyone who used to help me!

Here I want to express a sincere thank you to Professor Yasha Yi, my dissertation advisor, for his help and guidance during my Ph. D journey. Without his help, this dissertation can never be completed.

Also, I want to show my appreciation to Dr. Mao Ye, and all my other colleagues, who accompany me during my Ph. D and encouraged me to complete this tough journey; and to Kevin Owen, Shawn Wright, Pilar Herrera-Fierro, Vishva Ray, Brian Armstrong, Sandrine Martin, and all the other staffs in the Lurie Nanofabrication Facility, who gave me strong technical support in sample fabrication.

At last, thank all the people who ever gave me a hand during the research work during my Ph.D.

Table of Contents

List of Tables

List of Figures

Abstract

This dissertation comprises three research projects focused on the Integrated Optical Phased Array (OPA) device, which has been extensively researched for its potential applications in LiDAR. Chapter 1 in this dissertation serves as an introduction of the OPA research. The **first** project is introduced in Chapter 2, it examines the waveguide grating coupler in SOI-based OPA devices and identifies a limitation in beam steering range of approximately 15° per 100nm wavelength range. To overcome this challenge, the author proposes a compound period grating coupler structure that generates a second beam by combining two electrical field perturbations. The simulation results indicate that this approach can achieve a combined beam steering range of over 26° per 100nm wavelength range. Furthermore, the addition of a DBR structure at the device's bottom can also reduce the leakage of light power through the substrate. The study also investigates the device's fabrication tolerance. The **second** research project is introduced in Chapter 3, it deals with a conflict between the need for a large emitter aperture and the excessive number of phase shifters required to suppress the aliasing effect associated with such an aperture. To address this issue, the author proposes a phase-combining unit (PCU) structure that utilizes the phase interference between two identical light modes with different phases. This structure allows for using N phase shifters to control 2N-1 emitters. Simulation results suggest that a PCU-assisted device with N phase shifters performs similarly to a non-PCU-assisted device with 2N-1 phase shifters.

Experimental results also support this finding. Chapter 4-6 introduces the **third** project, which focuses on addressing the optical efficiency challenges that have hindered the industry-level maturity of OPA. Chapter 4 presents an end-fire 3-D OPA device based on a multi-layer SiN/SiO platform, the phase shifting and emitting parts are numerically investigated. The findings reveal that the edge-coupler for emitters can achieve an impressive light emitting efficiency of around 80%, with the beam's wavelength tuning capability and steering sensitivity customizable based on the specific application. In Chapter 5, the author designs the input coupling portion of the whole 3-D OPA device, and an experimental proof-of-concept whole device is fabricated and tested. The results demonstrate that the optical efficiency at both the input and output ends is significantly improved using the multi-waveguide-layer configuration. Finally, in Chapter 6, the author proposes and experimentally verifies a new fabrication method for the 3-D OPA using a single-lithography deep etching process. This method overcomes the limitations of the traditional multi-layer fabrication process, such as back control on gap thickness and layer misalignment.

Chapter 1 Photonic Integrated Circuits for the Optical Phased Array

1.1 Introduction

The photonic integrated circuit (PIC) has been proposed and studied since early 1980s, when researchers began to explore the potential of using photonic devices for in-formation processing and communication. PICs offer a number of advantages over electronic integrated circuits, such as higher speed and lower power consumption, both coming from the massless nature of photon. These devices are used in a wide range of applications, including telecommunications, data center interconnects, biomedical imaging, and sensing. As the demand for high-speed data transmission and processing continues to grow, photonic integrated circuits are becoming increasingly important in the development of next-generation communication and computing systems.

On the other hand, the optical phased array (OPA) is a device that controls the phase of light waves to obtain a desired beam propagation property without the need for moving parts. This is achieved by an array of optical emitters placed every several microns in a plane. When the emitting phase of every emitter can be controlled, the phase profile in the whole plane can be casually decided. Thus, the beam propagation property can be controlled. The OPA can steer the direction of the beam, change its shape, or even create com-plex patterns of light. Because of its versatile functionality, OPAs have many applications, including in LiDAR (light detection and ranging), wireless communication, and optical imaging. They offer a number of advantages over traditional

mechanical beam-steering systems, such as faster response time, higher accuracy, and lower power consumption. As the demand for high-speed, high-precision optical systems continues to grow, OPAs are becoming an increasingly important technology in a variety of fields.

OPAs with micron-level emitters can be realized by liquid crystal, metasurface, and solid-state photonic integrated circuits (PIC). Among these technologies, PIC-based OPA has drawn significant research efforts due to its advantages in faster response time and CMOS-compatible production method. Several review papers have been published over the years to introduce the OPA and LiDAR technology from different perspectives [1-6]. In this chapter, the authors attempt to offer an up-to-date review of the OPA technology with emphasis on component-level designing concerns and system-level progresses. The authors acknowledge that undertaking a comprehensive survey of a rapidly evolving field is exceedingly difficult, if not impractical. As a result, the authors apologize in advance to any researchers or institutions whose work may have been unintentionally omitted.

1.2 Basic Configuration of PIC-OPA

In most studies, researchers use either an external tunable laser or an on-chip active laser as the light source. After generating the light, it is distributed across multiple channels. Three types of light distribution networks are commonly used: MMI/Y-splitter trees, star-couplers, and cascaded direction coupler arrays. Later sections will discuss the advantages and disadvantages of each type. Once the light is distributed across multiple channels, the phase of the light mode in each channel must be modulated. This modulation determines the phase profile when the light is

emitted. The phase profile can be tailored to the specific application. For instance, beam steering is a commonly studied application for OPAs. In this case, the phase profile is designed to vary linearly with the emitter position. As a result, a flat equal-phase plane can be formed in the freespace, thus, a beam with the best spatial convergence can be generated perpendicular to the equal-phase plan. Furthermore, if the emitting phase profile can be accurately controlled, the beam's propagation direction can be adjusted without the need for any mechanical moving parts.

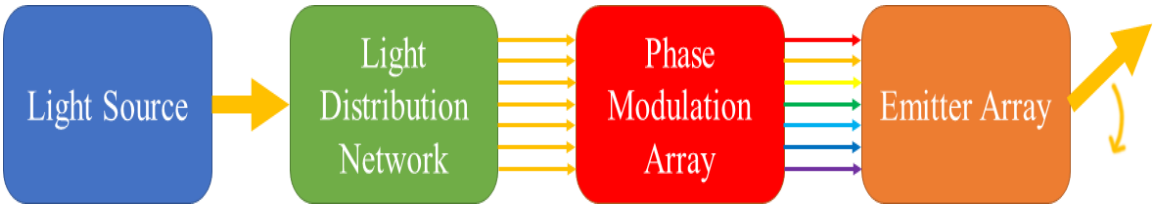

Figure 1: Basic Configuration of PIC-OPA.

1.3 Component Level Designing Concerns

A high-performance PIC requires careful optimization of every component including the coupler, waveguide bending, power splitters, and any other necessary elements. OPA is one of the most complex PICs currently known, a thorough optimization of every com-ponent is necessary for optimal performance. In this section, the authors review the com-ponent-level innovations from the published articles, including unique designs in emitter array, phase shifters, and on-chip light sources.

1.3.1 Emitter Array

The emitter array plays a crucial role in an OPA as it determines the intensity and phase profile of the emitting plane, ultimately affecting the interference of light in free space. The accurate control of light interference is essential for the excellent performance and versatile functionality

of PIC-OPAs. Therefore, the emitter array can be considered the most significant component of an OPA.

1.3.1.1 Emitter Type

There are 3 typical configurations of the emitter array, the end-fire emitter array, the waveguide grating array, and the nano-antenna array. Figure 2 illustrates the 3 types with examples from published papers.

1.3.1.1.1 End-Fire Array

The simplest design for an emitter array is the end-fire configuration [7-10]. In this setup, the light is divided into multiple channels with precisely controlled phases, then each channel waveguide terminates with an air interface that serves as a basic edge coupler toward the free space. With the end-fire configuration, the light emission doesn't depend on diffraction, which allows for achieving high efficiency across a broad spectrum. Fabrication is also simplified as the waveguide layer in an end-fire OPA can be defined with just one lithography step, unlike the other two types that require at least two litho-graph steps for the waveguide layer. However, there is a downside to this design. Since most PICs use a single-waveguide-layer setup, the end-fire array can only provide a 1 X N array that produces a beam that converges horizontally but diverges vertically, resulting in a fan beam as shown in Figure 2a-b.

1.3.1.1.2 Waveguide Grating Array

The most commonly investigated configuration is the waveguide grating array [11-15], as shown in Figure 2c-d. This configuration operates in a manner similar to the end-fire array, where

the light is also divided into 1 X N channels. However, instead of terminating the waveguides towards free space, this configuration features a grating coupler region. In this region, waveguide gratings with a certain length are situated along each waveguide. Once the light reaches the grating region, it undergoes diffraction and is emitted in a certain direction. When the grating period is determined, the diffracted light will constructively interfere to converge in a specific direction, providing beam convergence in that direction. In an OPA with a waveguide grating array, the diffraction gratings converge the emitted light beam in the waveguide direction (usually labeled as θ in related publications) and the waveguide array converges the beam through interference in the perpendicular direction (usually labeled as ψ in related publications). With a configuration that is only slightly more complex than an end-fire OPA, the waveguide grating array OPA can emit a 2-D converged beam, making it highly desirable for LiDAR applications.

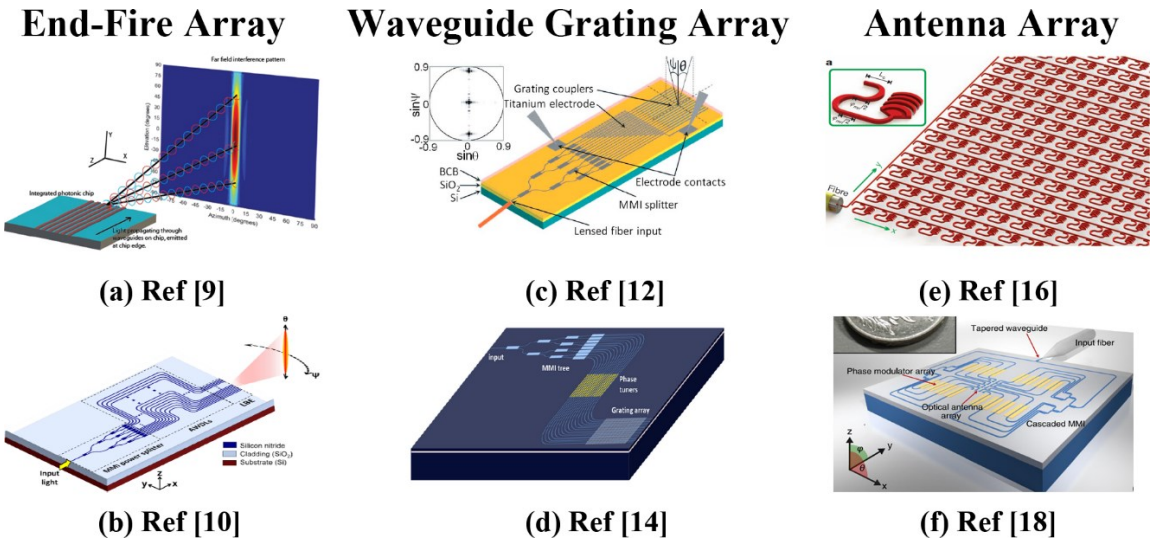

(a) Ref [9] **(c) Ref [12]** **(e) Ref [16]**

(b) Ref [10] **(d) Ref [14]** **(f) Ref [18]**

Figure 2: Three types of Emitter Array. (a-b) End-Fire Array [9, 10]. (c-d) Waveguide Grating Array [12, 14]. (e-f) Nano-Antenna Array [16, 18].

However, the waveguide grating array has a downside, which is the limited emitting

efficiency. This is due to the fact that the grating coupler emits light through diffraction, resulting in the emission of an upward beam as well as a downward leakage beam to the silicon substrate. This symmetric diffraction causes about half of the light power to be wasted. On the other hand, in this configuration, beam steering in the waveguide direction (θ) is achieved through wavelength tuning. However, when this type of OPA is used in an FMCW (frequency-modulated continuous wave) LiDAR system, the resolution in one di-rection (typically the vertical direction) cannot be maximized due to the wavelength de-pendency of the emitting angle. This results in the resolution being limited to the steering angle within the frequency modulation range.

1.3.1.1.3 Nano-Antenna Array

The end-fire array and waveguide grating array both have 1 X N channels, which implies that their phase profile can be controlled in only one direction. However, in the other direction, the end-fire array has no convergence, while the waveguide grating array has a predetermined phase profile that cannot be modulated. The proposed solution for having the ability to define the 2-D phase profile arbitrarily is to use the nano-antenna array OPA [16-18]. This setup distributes light into M X N channels, with each channel ending at a nano-antenna that emits light with a broad field of view. The light emitted from these antennas can then interfere in both directions (θ and ψ) in free space, allowing for the creation of a customizable 2-D phase profile. Compared to the waveguide grating array OPA, the nano-antenna array OPA has additional capabilities beyond beam con-vergence. For instance, a 64 X 64 antenna array OPA can produce complex patterns such as an "MIT" pattern [16] or a multi-beam pattern [17] in the far field. This is due to the fact that the

nano-antenna array OPA allows for more precise control over the phase profile of the emitted light than the waveguide grating array OPA.

On the flip side, it should be noted that implementing a nano-antenna array OPA is a more challenging task than the other two configurations due to its more complex layout. An M X N emitter array necessitates a larger space for the phase shifters and routing waveguides, making the layout more complicated than a 1 X N array. Additionally, the larger size of the nano-antennas compared to the typical waveguide dimensions results in a wider separation between emitters than in the 1 X N configuration, which leads to a stronger aliasing effect. Furthermore, the design of nano-antennas is based on diffraction from waveguide gratings, which also results in a roughly 50% power loss.

1.3.1.2 Emitter Envelope Function

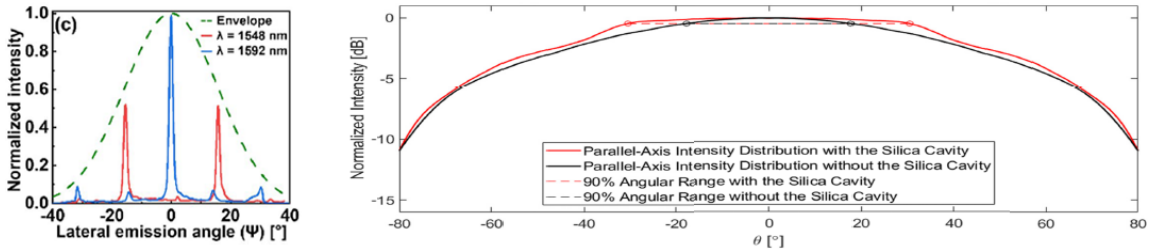

(a) Ref [10] **(b) Ref [19]**

Figure 3: Emitter Envelope Function. (a) The beam in the normal direction has the greatest intensity (blue curve), significantly higher than beams a certain degree away (red curve) [10]. (b) A relatively flat envelope function can be achieved [19].

OPA utilizes phase manipulation to determine the direction of constructive interference and shape a beam. However, its ability to steer the beam is limited to the range of a single emitter and the intensity of the beam in a particular direction depends on the emitter's envelope function. Typically, the envelope function is a Gaussian profile, which can result in significantly higher

intensity in the normal direction compared to other directions, as illustrated in Figure 3a. To address this issue, it is preferable to design emitters with a relatively broader envelope function by reducing the emitter size to promote more divergent emissions. Additionally, in the end-fire configuration, a low-index cavity such as a silica cavity can be added to broaden the center part of the envelope function [19], resulting in a plateau envelope as depicted in Figure 3b.

1.3.1.3 Emitter Arrangement

OPA's research begins with the arrangement of emitters at specific intervals, creating a periodic layout. In PIC-OPAs, waveguides are used to direct light to the emitters. How-ever, if the waveguide array is too dense, it can cause crosstalk between different channels, resulting in a distorted emitting phase profile. Therefore, the emitting pitch in a typical OPA design must be larger than roughly one wavelength. One consequence of having a large pitch is the occurrence of the aliasing effect, as shown in Figure 1.4a. When a target periodic signal (represented by the red curve) is sampled by periodic dots (represented by the blue dots) with a pitch that is too large (greater than half of the signal periodicity), the dots can form a different periodic signal with a different periodicity (represented by the blue curve). This is similar to what happens in periodic OPAs, where the distance between emitters is greater than half of the light wavelength. This causes grating lobes to appear in addition to the main lobe in the farfield, and the sparser the emitters, the denser the grating lobes. This phenomenon ultimately restricts the effective range over which the beam can be steered, thereby limiting the application of such OPAs in LiDAR systems.

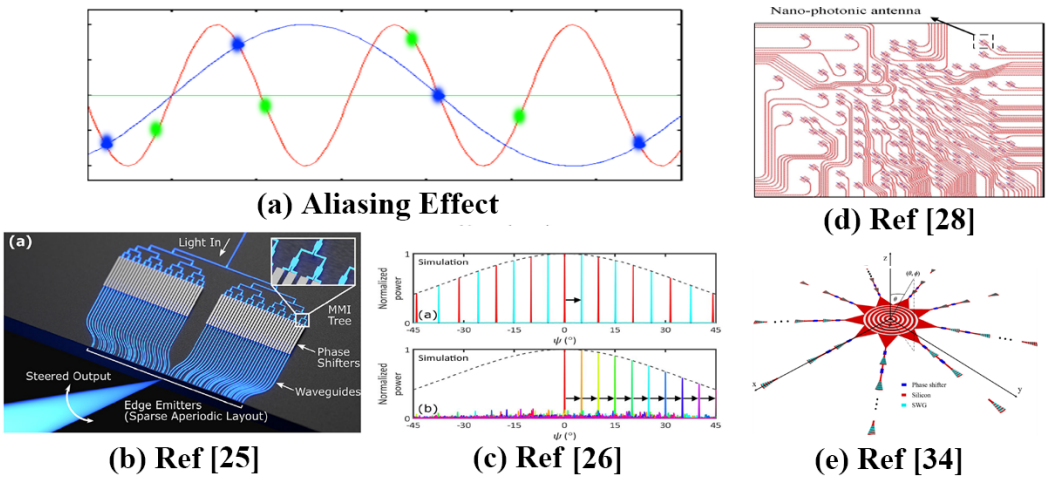

Figure 4: Aliasing Effect and Aperiodic OPA. (a) Illustration of Aliasing effect. (b) Aperiodic end-fire array OPA [25]. (c) The suppression of the aliasing effect by aperiodic arrangement [26]. (d) Aperiodic nano-antenna array OPA [28]. (e) Circular OPA [34].

1.3.1.3.1 Aperiodic Arrangement

A method to mitigate the issue of aliasing without challenging the half-wavelength limit is to utilize an aperiodic emitter arrangement. In Figure 4a, the periodic blue dots sample the target red curve but meanwhile create an aliasing blue curve, if using the green dots located at various positions, the target red curve can still be achieved while the aliasing blue curve is no longer supported. In the illustrated situation in Figure 4a, it is possible that the green dots may support another aliasing curve. However, it is theoretically feasible to create an aperiodic design where no more than two emitting dots support the same aliasing curve, therefore, the aliasing effect can be well suppressed.

This idea has been applied and extensively studied in PIC-OPA devices [20-30]. The design of aperiodic arrangements for OPA devices is highly dependent on factors such as emitter counts, spacing, and total aperture requirements, making it a case-sensitive process. Currently, there is no

analytical solution available that can guide the design of every aperiodic arrangement, if one even exists. The design of these arrangements can be based on either regular aperiodic patterns or purely irregular patterns [20]. In cases where an OPA needs to cover a larger emitting aperture with fewer emitters, the average spacing between emitters must be increased. In such cases, regular aperiodic patterns may not be effective [20], and the design process typically relies on optimization algorithms like particle sweep optimization, genetic optimization, etc. [21-23].

In a 1 X N channel OPA, the aperiodic arrangement effectively mitigates the aliasing effect in one direction (ψ), while the farfield performance in the other direction (θ) depends on the OPA configuration, whether it is an end-fire array or waveguide grating array [24-27]. Figure 4b depicts an end-fire array OPA, where the figure showcases the aperiodic arrangement of the emitter [25]. In Figure 4c, the simulation result of an aperiodic waveguide grating array OPA is shown [26]. The top figure displays a reference periodic OPA, which exhibits a strong aliasing effect, whereas the bottom figure always shows a single main lobe in the field of view, even when the beam is steered from 0° to 45°. Applying a 2-D aperiodic layout in a nano-antenna array OPA may enhance the system's complexity and design difficulty (as depicted in Figure 4d), but it has the potential to mitigate the aliasing effect in both the θ and ψ directions [28-30].

However, it is important to note that the aperiodic arrangement is not flawless. Its main purpose is to prevent the emitters from supporting the same aliasing function, thereby minimizing the appearance of grating lobes in the farfield. However, rather than eliminating the grating lobes, this method aims to flatten them out. Consequently, the noise level, commonly referred to as the

"side lobe level" in many publications, is higher in the farfield, as illustrated in Figure 4c. Furthermore, the power of light that was originally concentrated in the grating lobes in a periodic OPA is merely evenly distributed in the far-field in an aperiodic OPA, but not converging into the main lobe. Therefore, the aperiodic arrangement simply makes the main lobe the only noticeable beam, rather than enhancing the beam power.

The design of a 2-D aperiodic nano-antenna array OPA typically relies on an optimization method. All such methods can be categorized as improved exhaustive methods. However, a common challenge with these methods is that while the grating lobe level can be effectively suppressed for a specific beam direction during optimization, it may dramatically increase when the beam direction changes. This is attributable to the absence of circular symmetry in the rectangular OPAs. Circularly arranged OPAs have been pro-posed as a solution to this problem [31-35]. In addition to solving the issue of the grating lobe level increasing when the beam direction changes, circular OPAs offer another advantage. Light can be fed into them using a grating coupler situated at the center of the circle, which greatly simplifies the layout of the OPA, as illustrated in Figure 4e.

1.3.1.3.2 Challenge the Half-Wavelength Pitch Criteria

Although the aperiodic arrangement of emitters can effectively reduce the distortion caused by aliasing, resulting in only the main lobe being noticeable in the far field, it does not enhance the power of the beam. Careful optimization of the waveguide geometry can push the emitting pitch to 1.3um in the SOI (silicon on insulator) platform [36], which can suppress the aliasing

much better. However, to completely eliminate aliasing, it is necessary to use a half-wavelength pitch, but this can be challenging due to the crosstalk be-tween waveguides that are positioned too closely. Different methods have been proposed to mitigate crosstalk, such as using highly-confined waveguide modes and minimizing the propagation length when waveguides are at the half-wavelength pitch [9]. However, this approach is not easily scalable and is not appropriate for the waveguide grating array configuration since there is insufficient space to include a long grating coupler region, as the crosstalk suppression relies on a propagation length as short as 10um.

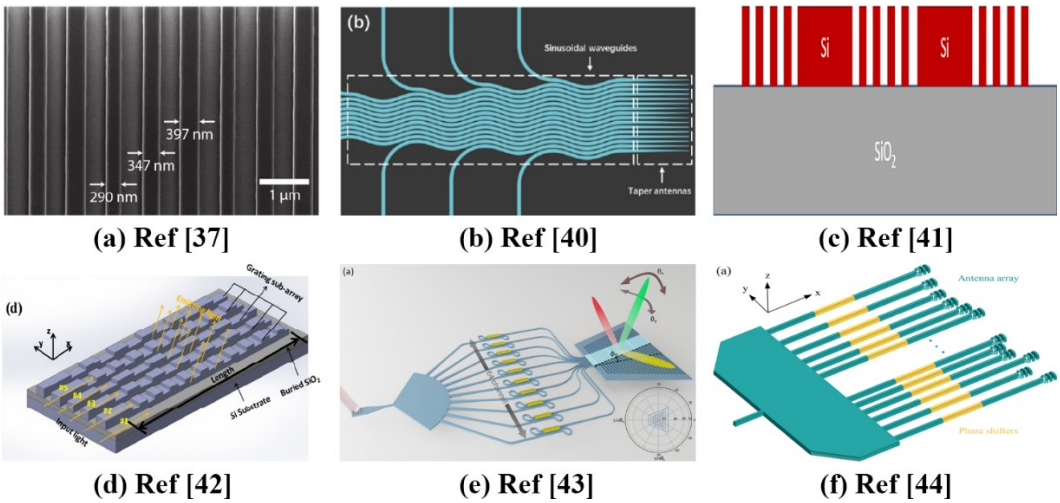

Figure 5: OPA designs with half-wavelength emitting pitch. (a) Different waveguide widths [37]. (b) Sinusoidal waveguide array [40]. (c) E-skid waveguides [41]. (d) Grating array superlattice [42]. (e) Slab grating region [43]. (f) Effective half-wavelength [44].

Several methods have been proposed to reduce crosstalk over a more extended propagation distance. Firstly, the use of waveguides with different geometries having different mode index can help suppress crosstalk by inducing index mismatch when such wave-guides are placed close to each other [37, 42], as shown in Figure 5a. Secondly, using a sinusoidal shaped waveguide array can break the symmetry along the centerline of the array, thereby keeping the difference between

the super-mode propagation constants of closely spaced waveguides at zero [38-40], as shown in Figure 5b. Thirdly, the use of extreme skin depth (e-skid) waveguides can significantly reduce the evanescent depth by employing high-index gratings at the waveguide spacings [41], as shown in Figure 5c. All these three designs can effectively suppress crosstalk between closely spaced waveguides, and approximately achieve the half-wavelength emitting pitch.

However, these methods rely on unique designs to suppress waveguide crosstalk, which significantly increases the complexity of the overall OPA device. In the first method, the emitting array comprises waveguides with varying widths, making it easy to achieve the end-fire array [37, 42], but challenging to apply to the waveguide grating coupler array configuration, thus difficult to obtain a 2-D converged beam. This is because that the different widths between waveguides effectively suppress crosstalk but also cause the propagation constant of the waveguide modes to differ, making it unsuitable to apply the same waveguide grating across the array. To make it work, the periodicity of the waveguide grating must be adjusted to the waveguide width so that the emitting angle from each waveguide remains the same [42], as shown in Figure 5d. However, designing such a grating superlattice is not as challenging as its fabrication, where strict accuracy is required. A more practical approach is to use a slab grating region [43]. As shown in Figure 5e, instead of having the light emitted from different waveguides and interfering at free space, a slab grating region allows the light from various channels to interfere firstly at a slab wave-guide region, then emit the interfered light by a grating region across the whole slab waveguide. On the other hand, in the second method, the sinusoidal waveguide array results in light propagation direction

varying at each position, making it unsuitable for the waveguide grating array configuration [38-40]. The third method uses high-index gratings to reduce the evanescent depth, which requires almost 10 times higher lithography resolution (with feature sizes as small as 36nm in the design [41]), significantly increasing the fabrication difficulty.

The three methods mentioned can produce an emitting pitch close to half-wavelength in a 1 X N configuration, which is suitable for end-fire or waveguide grating array OPA. However, in a M X N configuration for a nano-antenna array OPA, it is hard to achieve a true 2-D half-wavelength emitting pitch due to the limited footprint of the state-of-the-art nano-antennas. Nevertheless, an effective half-wavelength emitting pitch can be obtained in this configuration [44]. By arranging the nano-antennas back and forth, their projection in the x-direction can be spaced half-wavelength apart, while their projection in the y-direction forms a large aperture aperiodic arrangement. Together, they create a 2-D con-verged beam with true aliasing-free performance in the x-direction and aliasing-suppressed performance in the y-direction, as shown in Figure 5f.

1.3.1.4 Emitting Aperture and Intensity Profile

Although the term 'optical phased array' suggests that the phase is the critical factor in an OPA device because it determines how light interferes in free space, other factors such as the total emitting aperture and intensity profile also play crucial roles in light interference. Generally, a larger emitting aperture is preferred in an OPA device as it determines the maximum beam divergence that can be achieved [26,45,46]. This is often accomplished using a plane phase profile that emits a Gaussian beam, and the resulting beam divergence is described as $\Theta = (4\lambda)/(\pi D)$,

where Θ is the beam divergence in radian, λ is the wavelength of light, and D is the total emitting aperture [2]. As a result, the design of OPAs usually aim for a smaller emitting aperture for individual emitters to achieve a broader envelope function. At the same time, they aim for a larger total emitting aperture to minimize beam divergence. LiDAR is considered to be the most widely used application for OPAs. It typically requires a horizontal resolution of 0.1°, which is based on the size of a human at the braking distance of a car [2]. To have this level of resolution, an emitting aperture of over 1mm is required when the light beam is emitted in the normal direction. In addition, to maintain the same 0.1° horizontal resolution across the entire field of view, a even larger physical emitting aperture is necessary as the effective emitting aperture becomes smaller when the light beam is steered in other directions.

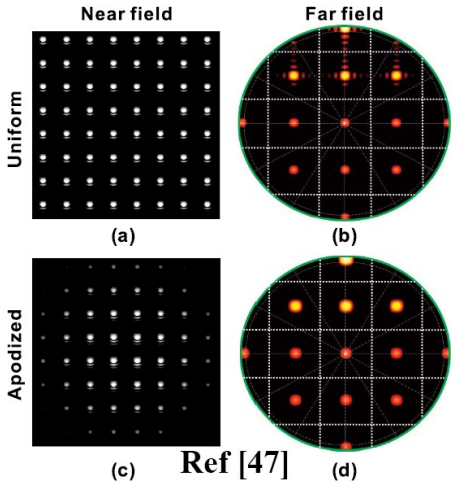

Figure 6: Simulation results of apodized intensity profile for OPA [47]. (a) Nearfield of uniform intensity profile. (b) Farfield of uniform intensity profile. (c) Nearfield of apodized intensity profile. (d) Farfield of apodized intensity profile.

For an OPA device with a 1 x N configuration, it is typically easier to achieve a larger emitting aperture in the direction across the N channels (ψ), while the emitting aperture in the other direction

(θ) is often constrained by the effective emitting length of the waveguide grating coupler. In section 1.3.5.1.2, the designs that address this issue are described in detail.

In addition to the phase, the intensity profile is also a crucial factor in light interference. While a uniform intensity profile is commonly used in most publications, it can lead to a common issue in phased array technology - side lobes - that occurs due to higher order interference. To mitigate this issue, the apodized intensity profile has been proposed as a solution in [17, 47]. This technique involves applying a Gaussian distribution to the emitted light intensity profile, which enhances the main lobe and reduces the occurrence of side lobes in the resulting interference pattern. However, this approach comes with a tradeoff - it reduces the effective emitting aperture, which leads to a larger beam divergence. The impact of both the suppressed side lobes and the larger divergence can be observed in the comparison between Figure 6b and 6d. Obtaining the desired intensity profile necessitates precise control over the power splitting of the light. One way to achieve this in a 1 X N channel OPA is to use a star coupler [26]. Alternatively, a directional coupler array can be utilized to achieve this in M X N channel OPAs [47].

1.3.1.5 Waveguide Grating Coupler Design

In the waveguide grating array configuration of OPA, the light is manipulated and directed by waveguide grating couplers in the θ direction. A typical waveguide grating coupler has gratings with a constant periodicity and duty cycle, which are fabricated using an additional lithography process or along with the waveguide patterning step [48]. The gratings cause the waveguide mode to fluctuate and generate a series of harmonic waves. One of these harmonic waves has a

propagation constant that matches the wavenumber of a radiation mode in a particular direction, allowing the light beam to be emitted in that direction. The coupling between the harmonic wave and the radiation mode can be described by the following equation.

$$k_0 \cdot sin\theta = \beta_0 + m \cdot (2\pi/\Lambda), \qquad (1.1)$$

where Λ is the periodicity of the gratings; θ is the emitting angle; k_0 is the free space wavenumber; β_0 is the propagation constant of the waveguide mode in the grating area; and m is the diffraction order, which in most cases is −1.

Unique designs have been proposed to improve the performance of waveguide grating coupler, including the beam steering range, beam convergence, emitting efficiency, etc.

1.3.1.5.1 Steering Range

Equation 1 can be derived as:

$$sin\theta = n_{eff} + m \cdot (\lambda/\Lambda), \qquad (1.2)$$

The emitting angle θ, can be adjusted by wavelength tuning. Although there is some dispersion of n_{eff}, the primary factor affecting the direction of the beam is the term $m \cdot (\lambda/\Lambda)$. To ensure that $\sin\theta \in (-1,1)$, a suitable value of Λ must be chosen. This means that the amount by which the angle θ changes in response to a change in wavelength λ, denoted as $d\theta/d\lambda$, is constrained by n_{eff}, while the value of n_{eff} is determined by the material platform used. SOI platform is one of the most extensively researched platforms for OPAs. This platform is characterized by a large index contrast between the waveguide and cladding, with indices of approximately 3.47 for Si and 1.46 for SiO2 at a wavelength of around 1550nm. For this platform, the value of $d\theta/d\lambda$ is limited

to approximately 15° per 100nm wavelength range around 1550nm [12]. On other platforms with lower index contrast, such as SiN waveguides with SiO cladding, the value of $d\theta/d\lambda$ is typically lower, approximately 7.4° per 100nm wavelength as described in reference [49]. This limitation significantly restricts the field of view (FoV) of an OPA system.

Various designs have been proposed to overcome this limitation, as described in references [50-57]. These designs can be divided into two categories. The first category in-volves ensuring that the grating coupler functions effectively as multiple normal grating couplers, which have a uniform periodicity and duty cycle [50-53]. By spatially combining two normal grating couplers, a compound period grating coupler can be formed, which can generate two emitting beams, resulting in a steering range of approximately 26° over a 100nm wavelength range - roughly double the original steering capability [50]. The multi-beam concept can be further developed to generate 9 beams from a single grating coupler, although this is more about detecting 9 points simultaneously rather than enlarging the steering range [51]. By utilizing 3 different modes and designing nano-gratings that create spatial fluctuation specifically for each mode, the steering range can be roughly tri-pled to approximately 40° [52]. Additionally, by incorporating a switch and two polarization rotators before the grating coupler, both directions (forward and backward) and both polarizations (TE and TM) can be selected, resulting in a steering range that is roughly 4 times greater, reaching 54.5° over a 100nm wavelength range [53]. The second category of attempts to mitigate the restriction on steering range involves manipulating the effective index (n_{eff}) by incorporating a photonic crystal waveguide [54-57]. In this type of waveguide, the n_{eff} can be

substantially increased at the spectral boundary of the photonic bandgap, resulting in a significantly greater dθ/dλ despite a limited wavelength range de-fined by the photonic band spectrum. This approach can achieve a steering range of 23° over a 29nm wavelength range [54]. All these designs are illustrated in Figure 7.

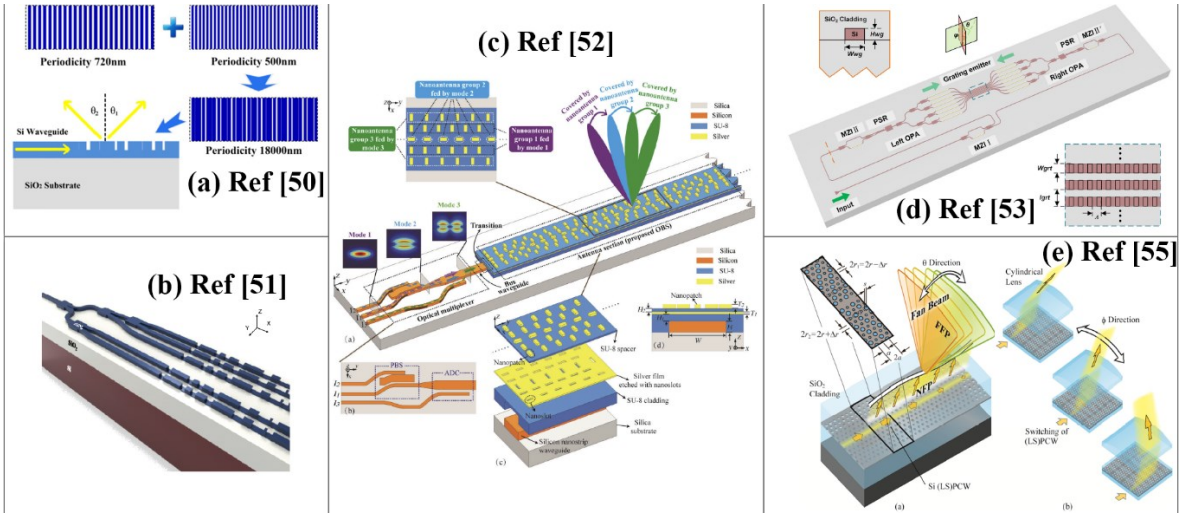

Figure 7: Waveguide GCs with larger beam steering range. (a) Compound period GC [50]. (b) Multi-beam GC [51]. (c) Polarization-division and spatial-division GC [52]. (d) Dual polarization and bi-directional GC [53]. (e) Photonic crystal slow light GC [55].

1.3.1.5.2 Effective Aperture

In a typical waveguide grating coupler, the periodicity and duty cycle of the grating are identical, causing each grating to emit an equal proportion of the rest light in the waveguide. As a result, the emitting intensity profile decays, and the effective emitting aperture is limited, which ultimately leads to poorer interference conditions in the θ direction. According to reference [12], the emitting power declines to $1/e^2$ after passing through 35 gratings, resulting in an effective emitting aperture of only about 20 microns, even though 50 gratings were fabricated.

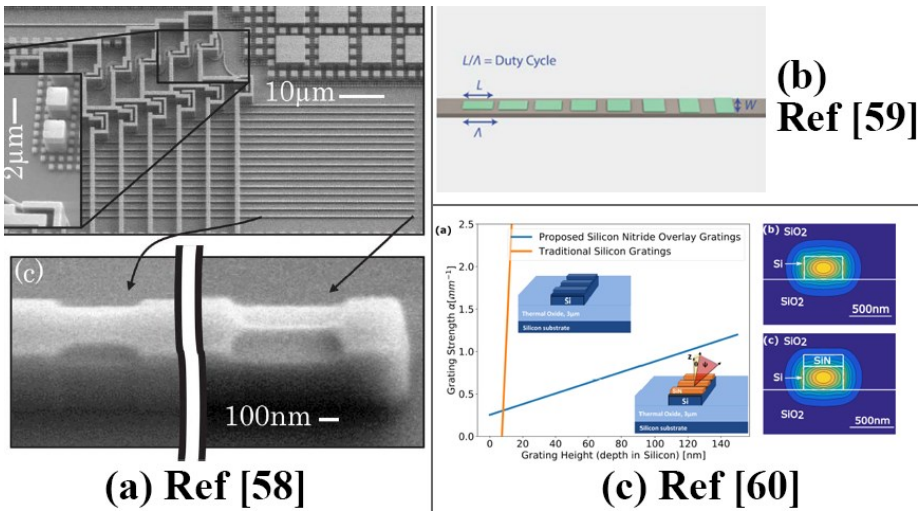

Figure 8: Waveguide GCs with increased effective emitting aperture. (a) Gradually adjusted GC [58]. (b) SiN GC on Si waveguides [59]. (c) Si and SiN gratings [60].

One effective way to address this issue is to perform a shallow etching of the grating, which can reduce the portion of light emitted per grating. Research has shown that even with identical periodicity and duty cycle, shallow etched gratings as thin as 16nm can achieve a 0.14° FWHM by a waveguide grating over a 1mm distance [26]. Another approach involves using gratings with gradually adjusted duty cycles, which can produce a uniform emitting intensity profile from a decaying waveguide mode. This method has been demonstrated to achieve a 3.3° FWHM with a small aperture of 32um, as depicted in Figure 8a [58]. However, while the silicon-on-insulator (SOI) platform offers a relatively larger beam steering capability, it also limits the effective emitting aperture due to the excellent mode confinement of silicon waveguides, which results in a greater amount of mode power being emitted per grating. On the other hand, silicon nitride (SiN) waveguides are better suited for effective emitting aperture, but their beam steering capability is limited. A combination of silicon waveguides and SiN gratings can provide the advantages of both.

As shown in Figure 8b and 8c, by placing SiN gratings with gradually adjusted duty cycles above the silicon waveguide, waveguide grating couplers with a uniform emitting pattern, large emitting aperture, and good beam steering capability (com-parable to 15°/100nm, typical value for SOI-OPA) can be achieved [59-61]. The beam con-vergence (FWHM) is proved to be approximately 0.089° for 1mm long waveguide gratings [59,60], and approximately 0.0435° for 3mm long waveguide gratings [61].

1.3.1.5.3 Emitting Directionality

Waveguide gratings have the ability to emit light through diffraction, but this process also reduces their efficiency, typically resulting in less than 50% of the light being emitted upwards due to the symmetrical downward emission. As a result, a significant portion of the light energy is lost to the substrate [50]. In LiDAR applications, this low optical efficiency limits the detection range, creating a major obstacle to achieving a mature product at the industry level.

To tackle this problem, two methods have been proposed [62-66]. The first approach involves using reflections at the interfaces between the waveguide layer and the top/bottom claddings [62-64], as shown in Figure 9a-c. With this method, detached gratings are fabricated at another layer above the waveguide, allowing the downward emission to be reflected at the top and bottom surfaces of the waveguide and the bottom surface of the buried oxide layer. By carefully adjusting the layer thickness, it's possible to optimize the efficiency of upward emission. The detached gratings can be fabricated on a low-index SiO2 layer on top of the waveguide to achieve an upward emitting efficiency of over 70% within a 100nm wavelength range and a steering angle of 15° [62].

Alternatively, the gratings can be fabricated on a high-index layer above the top cladding, where the waveguide mode is firstly coupled to the top grating layer and then emitted [63,64]. By fabricating the high-index gratings on an amorphous silicon layer, an efficiency of over 50% can be achieved within a broad wavelength range of 1480nm to 1620nm, along with a steering angle of 20.2° (comparable to 15° per 100nm wavelength range) [63]. However, this approach has a lower efficiency due to the angular dependence of light reflection. To optimize the directionality, the gratings can be fabricated on a top Si3N4 layer, limiting the beam steering to 8.6° per 100nm wavelength range, while achieving a directionality of over 86% within the wavelength range [64].

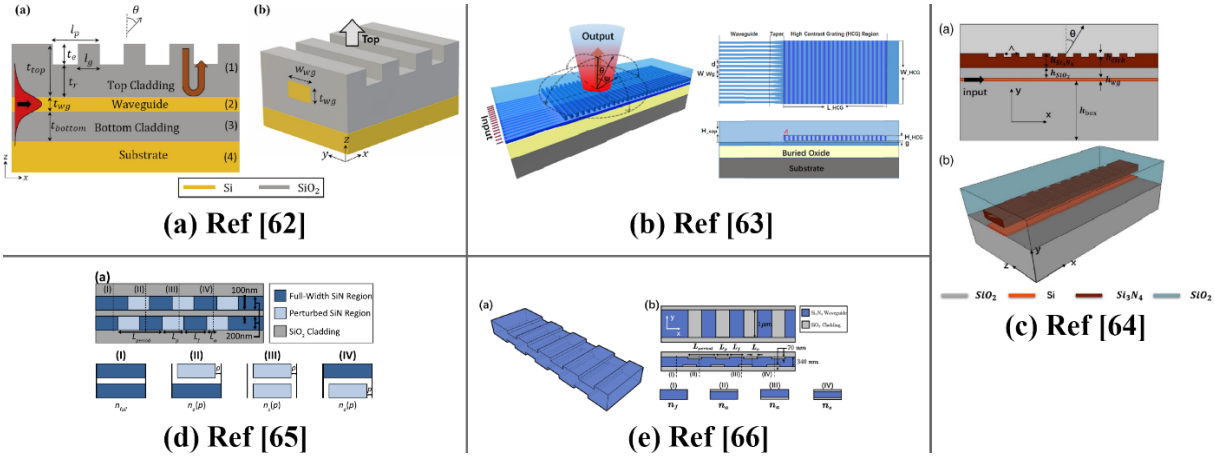

Figure 9: Waveguide GCs with increased emitting directionality. (a) Detached low index SiO2 gratings [62]. (b) Detached high index a-Si gratings [63]. (c) Detached Si3N4 gratings [64]. (d) Dual-layer Si3N4 gratings [65]. (e) Dual-layer-trench Si gratings [66].

The second method involves creating two different spatial fluctuations with a slight offset, which are dual gratings on the waveguide mode [65,66], as shown in Figure 9d-e.. These dual gratings generate separate upward and downward beams, with careful design to ensure that the two upward beams interfere constructively, and the two downward beams interfere destructively, resulting in high directionality. Dual gratings can be achieved through a dual-layer Si3N4

waveguide configuration [65] or by making different trenches on both the top and bottom surface of a silicon waveguide [66]. Both configurations can achieve an emitting efficiency of over 90% at the design wavelength (1550nm), although their broadband performance and beam steering capability have not been reported.

1.3.2 Phase Shifters

Typically, in OPA devices, a phase shifter is needed for each channel to regulate the emitting phase profile and control the farfield pattern. Thermo-optics and electro-optics effects are the two common options, as they both are effective in silicon [67]. An optimal phase shifter for OPAs should meet several criteria, such as being small enough to not re-quire a larger phase shifter array for a certain size emitter array, responding rapidly to enable high beam steering speed, being lossless to prevent affecting light power during phase tuning, being adequately isolated to avoid interference with adjacent channels, consuming low power to keep the total power for the entire OPA within reasonable limits, and being easily fabricable. It should also be capable of tuning the phase across the full 2π range, although phase shifters with insufficient tuning range can also be used [68]. De-signing a phase shifter that meet all the criteria is critical, if even possible.

1.3.2.1 Thermo-Optics Phase Shifter

The thermo-optic effect is present in nearly all materials, with a greater intensity typically observed in semiconductors compared to insulators. Silicon, in particular, exhibits a substantial thermo-optic coefficient. Additionally, the fabrication process for a thermo-optic phase shifter is relatively straightforward, as it does not require any doping or heterogeneous integration.

Consequently, TO phase shifters are commonly utilized in OPA systems. Typically, a conventional TO phase shifter is constructed using a conductor pad located a few microns above the waveguide. This allows the pad to heat the wave-guide material without affecting with the waveguide mode. However, this type of phase shifter has some limitations, such as a relatively slow response time (up to around 100kHz) and a higher power consumption (approximately 10-20mW/π), as it relies on heat conduction through the insulating cladding layer for heating and cooling [2]. To address these limitations, a potential solution is to explore more efficient heat transfer mechanisms, despite that it also leads to a more complex fabrication process in most cases. One approach is to use designs such as a contacted waveguide heater, which directly heats the waveguide without affecting the propagation mode, by leveraging the mode pro-file at waveguide bending [16] (as shown in Figure 10a). Alternatively, graphene heaters with an air trench [69] (as shown in Figure 10b) or polymer heaters [70] can also be employed to achieve improved heat transfer. Another possible approach to enhance the efficiency of the TO phase shifter is to increase the effective light path at the heater region. This can be achieved through the use of a resonance cavity [71] (as illustrated in Figure 10c) or a mode multiplexing system [72] (as shown in Figure 10d). However, it should be noted that this approach is usually wavelength dependent and could potentially affect the mode intensity during the phase tuning process, as either the resonator or mode coupling is sensitive to wavelength.

1.3.2.2 Electric-Optics Phase Shifter

Although there are various distinctive designs available to improve the efficiency of a TO

phase shifter, it remains a relatively slow method due to the slower heat transfer mechanism. In contrast, the electro-optics (EO) effect is faster, and therefore, an EO phase shifter is typically over 10 times faster than a TO phase shifter.

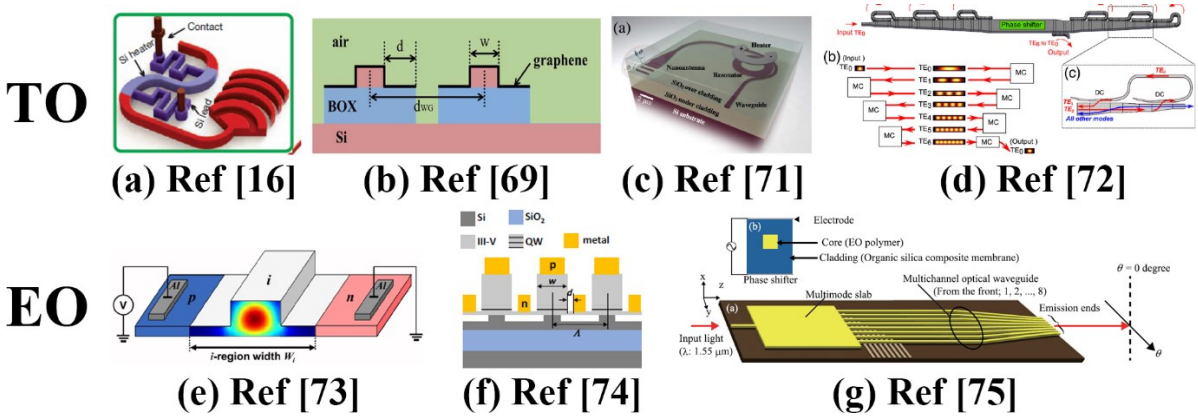

Figure 10: Phase shifters in OPAs. (a) Contacted heater [16]. (b) Graphene heater [69]. (c) Ring-resonator phase shifter [71]. (d) Mode multiplexing heater [72]. (e) PIN EO phase shifter [73]. (f) III-V phase shifter [74]. (g) EO polymer phase shifter [75].

However, silicon lacks a good electro-optics effect, and to construct a silicon based EO phase shifter, a PIN diode (as shown in Figure 10e, [73]) or PN diode must be built, then it can utilize the diode to adjust the free carrier density in the waveguide area. Nevertheless, both carrier depletion and carrier injection cause significant optical loss in the waveguide and are at least one order of magnitude larger than their thermos-optic counterpart in footprint. Moreover, building such EO phase shifters entails a doping process, which substantially increases the fabrication complexity. Despite all the disadvantages mentioned above, an OPA driven by EO phase shifters is several orders of magnitude faster than TO-OPAs. Therefore, it remains the preferred choice for applications that require a high scanning rate, such as LiDAR. In addition, there are alternative options available for EO phase shifters, such as heterogeneous integrated III-V phase shifters

(illustrated in Figure 10f, [74]) or EO polymers (illustrated in Figure 10g, [75]), which can be utilized if CMOS compatibility is not a critical requirement.

1.3.2.3 Reducing the Required Number of Phase Shifters

OPAs generally require an individual phase shifter for each emitter. While having more emitters in an OPA typically improves its performance, increasing the number of individual phase shifters may not always have only positive effect. Using too many individual phase shifters can result in excessive power consumption, as well as increased complexity in the driven circuit, and longer time consuming for the phase calibration process. Despite the attempts to having more individual phase shifters are always exist [76], the need to balance the number of emitters and individual phase shifters in an OPA has motivated significant research into developing configurations that enable the control of multiple emitters with fewer individual phase shifters, while maintaining consistent phase across all emitters.

To achieve this goal, two methods are employed. The first approach involves grouping multiple phase shifters into one drive. By using a triangular heater to proportionally heat multiple waveguides, the phase change across different channels can be made linear, as shown in Figure 11a [12, 77, 78]. Additionally, by using one drive to heat up phase shifters in one line, 2-D beam steering can be achieved using column and row phase shifters together, as long as the initial phase is able to converge the beam, as illustrated in Figure 11b [16, 17]. The cascaded or group cascaded shifters offer the same phase shifting to all channels, and along with passive phase shifting from waveguide length and power splitter, the phases at multiple emitters can align to form and steer

the beam, as shown in Figure 11c and 11d [58, 79, 80]. The other method involves leveraging the interference of waveguide modes. By combining two modes with the same propagation constant but different phases, a single mode can be formed with the same propagation constant and an average phase. By this approach, a M X N OPA with N2 emitters can be controlled by 2N phase shifters (Figure 11e, [81]), and a 1 X N OPA with N emitters can be controlled by (N+1)/2 phase shifters (Figure 11f, [82]). Nonetheless, these designs are susceptible to phase errors because they assume that the same passive waveguide path will always result in the same phase change, which may not hold true in real samples due to imperfections in the fabrication process. Consequently, it is imperative to develop designs and materials with better fabrication tolerances for these approaches [80].

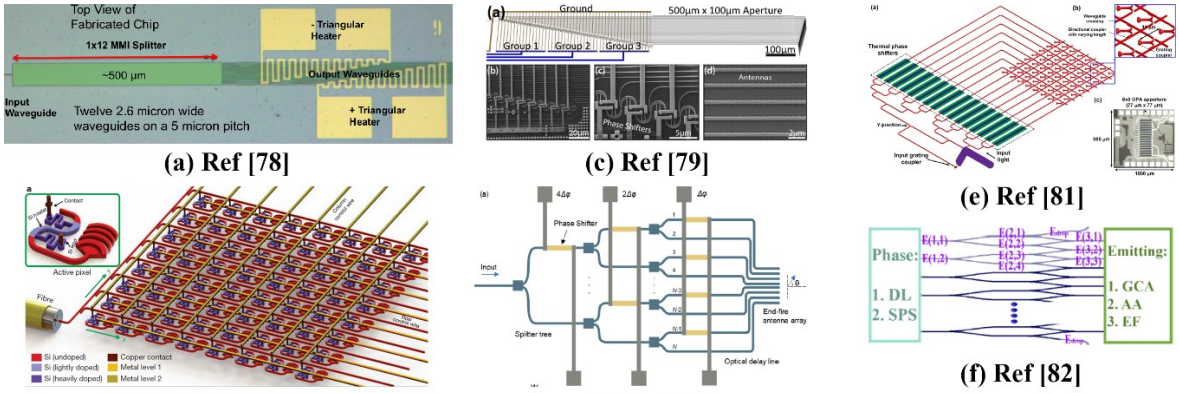

Figure 11: OPAs with fewer phase shifters than emitters. (a) Triangular heaters [78]. (b) Column phase shifters [16]. (c) Cascaded phase shifters [79]. (d) Grouped cascaded phase shifter [80]. (e) Interference based configuration for M X N OPAs [81]. (f) Interference based configuration for 1 X N OPAs [82].

1.3.3 On-Chip Light Source

While applying an on-chip light source can improve the performance of OPAs [83-89], its advantages over other types of PICs, such as optical transceivers or sensors, are not significant.

The challenges in implementing an on-chip light source on OPA are the same as those involved in developing a light source on a silicon platform, which is primarily due to the indirect bandgap of silicon. Nonetheless, researchers have reported the successful use of heterogeneous integrated InP light sources [83-86, 88] and Erbium-doped light sources [87] for PIC-OPAs. Integrating an on-chip light source can significantly reduce the size and complexity of the OPA system, eliminating the need for an external laser. This, in turn, has the potential to reduce the cost of OPA-LiDARs.

1.4 Phase Calibration and On-Chip Emitting Monitoring

Fabrication imperfection is a prevalent problem in PICs, caused by roughness and errors during the layer deposition and lithography processes. This can lead to propagation loss and phase errors in the passive waveguides. Additionally, in OPAs, fabrication imperfection can cause practical issues where the initial emitting phase profile is often irregular, regardless of the intended design for a regular phase profile. When faced with such scenarios, OPAs that possess an equal quantity of emitters and phase shifters can depend on their phase shifters to correct any passive phase errors. On the other hand, OPAs with fewer phase shifters must utilize designs and materials that allow for fabrication tolerance in order to compensate for such errors. Nevertheless, optimizing the phase compensation process that involves multiple variables can be a time-consuming task, even though the desired phase profile may vary according to the application, such as a linear phase profile for beam steering or a customized phase profile to generate an arbi-trary pattern [17,90]. Despite the fact that it is also feasible to conduct phase calibration at the wafer level [91], this procedure typically occurs at the chip level.

Numerous algorithms have been successfully utilized for phase calibration of OPAs, such as the particle swarm optimization (PSO) [84], deterministic stochastic gradient de-scent (DSGD) method [92], chaotic stochastic parallel gradient descent (CSPGD) method [93], rotating element vector (REV) method [94] or modified REV method [95], radix-p method [96], adjacent sampling principal component analysis (AS-PCA) method [97], and random phase modulation method [98]. Although these algorithms are much more effective than the exhaustive method, they are still numerical optimization algorithms, because they are unable to detect the phase difference directly between each pair of emitters. While it is indeed achievable by calculating the interference pattern [99], which can significantly reduce the time required for phase calibration.

Typically, a calibrated OPA includes an internal database that contains multiple sets of voltage values. Each of these sets is specifically calibrated to be applied to phase shifters and is effective at a particular angle. However, the OPAs are normally sensitive to environmental changes such as temperature [100]. An on-chip monitor can be applied to OPAs to track the emitting farfield pattern [84-86,101]. The reported on-chip monitors are all based on the 1 X N channels waveguide grating array OPAs. The fundamental concept involves allowing the waveguide gratings to leave a small portion of the light power and then coupling all channels directly into a slab waveguide area. The light from multiple channels will interfere in the slab waveguide in the same manner as it does in free space. By capturing the interference pattern in the slab area using a multi-output photodiode array, the farfield emitting pattern can be monitored at the cost of a lower-emitting efficiency.

1.5 System Level OPA Designs

OPAs have a versatile configuration, which makes them suitable for various applications. However, designing OPAs for different situations requires careful consideration of the entire system to ensure that they meet practical needs. Therefore, this section provides an overview of OPAs as a whole system, which aims to provide a more comprehensive understanding of OPA studies.

1.5.1 Passive OPAs

OPAs utilize control of the emitter phase profile across the emitter array to achieve functions such as beam shaping and steering. This usually involves the use of multiple phase shifters to attain the desired phase profile. However, as highlighted in section 3.2, employing a large number of phase shifters can result in practical challenges, such as high power consumption, operational difficulty, and a time-intensive phase calibration process. Consequently, efforts have been made to develop purely passive OPAs to mitigate these issues [102]. Unlike waveguide grating array OPAs, which are semi-passive and rely on wavelength tuning and electrical tuning to achieve steering in different directions (θ and ψ), purely passive OPAs have only one degree of freedom for tuning - wavelength. Passive OPAs require pre-coding of the emitting phase profile in the design, typically through the use of components such as waveguide length and symmetric power splitter networks. However, due to that active phase shifters no longer exist, this approach is much more susceptible to phase errors resulting from fabrication imperfections. To improve fabrication tolerance and mitigate the impact of phase errors, low-index materials like silicon nitride or silica are commonly

employed as waveguide materials in passive OPAs [10,103].

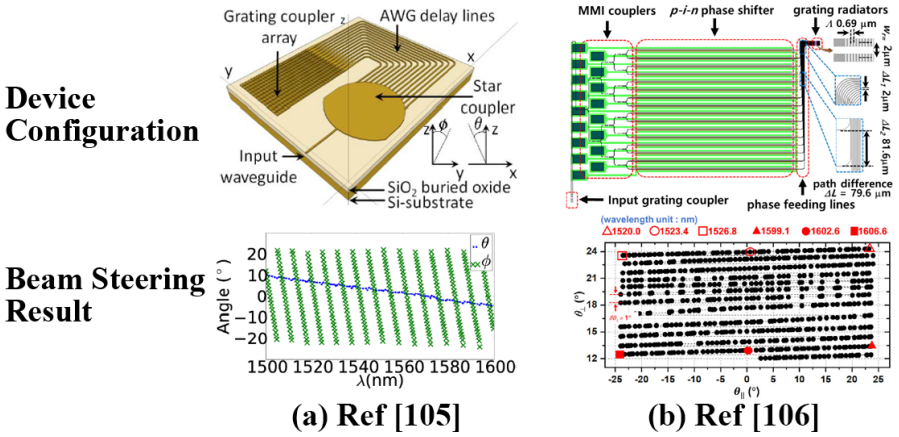

Figure 12: Designs of OPAs to achieve 2-D beam steering with only wavelength tuning. (a) Ref [105]. (b) Ref [106].

Achieving 2-D beam steering with only one degree of freedom is a significant challenge in passive OPAs. However, this issue can be addressed by leveraging the interference that can occur in multiple orders [46, 104-106]. The solution involves implementing relatively slower beam steering in one direction (θ), which can be achieved using waveguide grating couplers [46, 105, 106] or short delay lines across the channels [104]. In contrast, a much faster beam steering must be implemented in the other direction (ψ), which can be achieved using longer delay lines across the channels. As a result, the beam can be steered in θ across the entire wavelength range and steered in ψ at multiple smaller wavelength ranges, with each smaller range corresponding to a different angle in θ. This is illustrated in Figure 12.

1.5.2 Distance Detection for the LiDAR Application

The intense interest in OPA research is driven by the demand for solid-state Lidar, which is considered a key component in autonomous driving technology. This interest is not limited to the OPA itself, as system-level OPA-LiDAR is also being studied. Several successful distance

detection methods have been reported [79,107-110] on OPA-Lidar. Regardless of the number of degrees of freedom (depending on the number of individual phase shifters) an OPA uses for 2-D beam steering, an additional degree of freedom is required for distance detection.

A straightforward approach involves adjusting the light power to measure distance, as depicted in Figure 13a. This technique entails emitting a light pulse towards the target, followed by detecting a reflection pulse at a later time. The time interval between the two pulses can be used to compute the distance by measuring the time of flight (ToF) [107]. Nonetheless, this approach is prone to interference from ambient light. To ensure adequate differentiation of the reflection light, a relatively higher light intensity is required, leading to increased power consumption of the Lidar and raising concerns about eye safety.

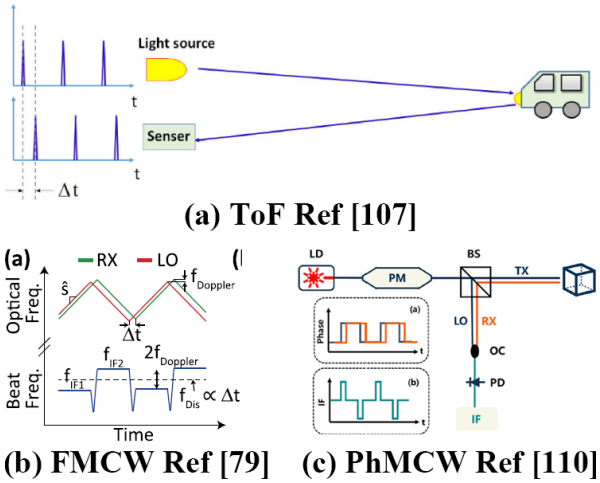

Figure 13: Distance detection methods. (a) Time of flight (ToF) [107]. (b) Frequency-modulated continuous wave (FMCW) [79]. (c) Phase-modulated continuous wave (PhMCW) [110].

Frequency-modulated continuous wave (FMCW) is proposed as an improved LiDAR approach [79, 107-109], as illustrated in Figure 13b. This method employs a continuous wave with periodic variations in frequency to compute distance by measuring the phase difference between

the emitted and reflected light. Moreover, FMCW Lidar is less susceptible to ambient light as a small fraction of the emitted light is directed towards the receiving end and oscillates with the reflected light (known as the local oscillator) to form a beat frequency, making it easier to distinguish the reflected light. Another advantage of FMCW over ToF is its ability to detect object velocity, thanks to the Doppler effect which induces a frequency shift in the reflected light. This frequency shift is also easily distinguished due to the local oscillation. In contrast to 3D mapping achieved by a ToF-LiDAR, an FMCW-LiDAR has the capability to perform a 4D mapping, which includes 3D mapping and velocity. Nonetheless, the resolution of the FMCW technique for detection is some-what restricted in an OPA-LiDAR, if that OPA utilizes frequency as a degree of freedom for beam steering. This is because the beam is not stationary in one direction during the frequency modulation. As an alternative, a phase-modulated continuous wave (PhMCW) method, as illustrated in Figure 13c, is proposed [110]. With this approach, the phase of the emitting beam is utilized as the degree of freedom for distance detection instead of frequency.

1.5.3 Other Material Platforms

Most of the PIC-OPAs are on the silicon platform such as SOI (silicon on insulator) or amorphous silicon [111]. In addition, OPAs on other material platforms are also studied for various purposes.

1.5.3.1 Silicon Nitride (SiN) and Germanium-Silicon (Ge-Si)

Silicon is a material well-suited for OPAs used in telecommunication wavelengths, while there is also a growing interest in researching OPAs for shorter wavelengths, including the visible

range. This is due to the potential applications in fields such as virtual reality displays, biomedical sensing, stimulation, etc. Silicon loses its effectiveness as a material for wavelengths shorter than 1.1um, but there is a viable alternative in silicon nitride (SiN). SiN is a good option due to its transparency in the visible and near-infrared spectrum, which is ideal for OPAs that require a wide range of operating wavelengths [114]. Moreover, SiN is CMOS compatible, which offers a possible cost-effective production method for SiN-OPAs. On the other hand, SiN also has certain limitations that need to be taken into account. One of the main issues is its low refractive index, which results in a low mode confinement in SiN waveguides, making it challenging to build a dense SiN waveguide array. Consequently, SiN-OPAs may suffer from a strong aliasing effect [45] or require the use of an aperiodic arrangement [25], which increases the complexity of the system. In addition, SiN is an insulator, lacking an effective electro-optics effect, and its heat transfer coefficient and thermos-optic coefficient are both about one order of magnitude lower than that of Si. As a result, its thermos tuning is relatively ineffective. While switching light between multiple OPAs with different passive targets may mitigate this issue, it can make the entire OPA device overly complex [115].

The limitations of SiN include its low refractive index and its properties as an insulator. However, these limitations can also offer advantages in other aspects. The low refractive index of SiN results in low mode confinement, which can be advantageous in terms of tolerance to fabrication imperfections. In lower-index waveguides, a certain sidewall roughness takes up less area of the waveguide mode, so that the fabrication errors result in lower phase error in such modes.

Thus, SiN is preferred for passive OPAs [10]. In addition, OPAs have been reported that use SiN for passive components, such as input couplers, power splitters, and waveguide bends, and use Si for the phase shifters [116-119]. This allows them to take advantage of SiN in passive components and also the effective modulation of Si at the same time. On the other hand, the fact that SiN is an insulator also means that it is free of two-photon absorption, which is a limitation when using Si to propagate high power light. SiN-OPAs can therefore handle high light power, making them desirable for achieving a longer detection range in LiDAR [119].

SiN is considered suitable for lower wavelength OPAs, whereas Germanium (Ge) is preferred for higher wavelength OPAs [120]. Ge has a wide transparent window that ranges from 2um to 14um. Ge's refractive index is higher than that of Si, which enables the direct fabrication of Ge waveguides on a Si substrate, without the need for a buried oxide layer. Moreover, the high refractive index of Ge facilitates the achievement of the half-wavelength criteria in a Ge-Si OPA.

1.5.3.2 III-IV Materials

Ge-Si is not the sole choice for optical parametric amplifiers (OPAs) operating at wavelengths greater than 1550nm. III-V semiconductor materials can also be utilized for OPAs, including the GaAs/AlGaAs platform [7, 11] and InP platform [92, 121]. In comparison to Ge-Si, InP offers additional benefits, aside from having a relatively wider transparent window [121]. InP is a direct bandgap semiconductor, which enables the availability of a widely-tunable on-chip light source in this platform. Furthermore, it is possible to integrate semiconductor optical amplifiers (SOA) into InP-OPAs to boost the optical power output, allowing for the emission of high-power beams.

Additionally, InP-based phase shifters can employ the current injection electro-optics effect, which provides a fast tuning speed of just a few nanoseconds [92].

1.5.4 Other Applications

The research on OPAs has gained momentum due to the emergence of autonomous driving technology, which requires solid-state LiDAR. However, OPAs can have multiple applications beyond autonomous driving, given their ability to precisely control the phase profile by using a sufficient number of phase shifters. These applications include emitting various types of beams such as orbital beams [122], quasi-Bessel beams [123], and focusing beams [124], as well as imaging by combining multiple scanning points [125-127]. OPAs can also function as receivers by detecting the emitting angle of a coming beam [128], allowing for the creation of directional reflectors [129] and OPA cameras [130]. By combining the receiving and emitting capabilities of OPAs, optical transceivers can be developed [131-133], enabling wireless communication with directional links [78,134-138]. Additionally, OPAs have potential in bio-applications, where a neural stimulation OPA [139] and a neural probe [140] have been developed.

1.6 3-D OPAs

The majority of OPA works utilize a single-waveguide-layer setup. This configuration is the most well-established platform for PICs, similar in concept to CMOS electronic inte-grated circuits which build fundamental components on the surface of a wafer (transistors for EICs and waveguides for PICs) and then create electrodes above it. However, in the case of PIC-OPAs, this configuration often results in significant insertion loss, primarily due to fiber-to-chip coupling and

diffraction-based emitters which are essential for 2-D converged beams. However, the efficiency of light plays a vital role in certain applications like solid-state LiDAR since it directly impacts the LiDAR's detection range and power consumption. Although various techniques can be utilized to alleviate the problem of optical efficiency and power consumption [12,16,17,58,62-66,76-82], the detection range remains a significant obstacle to implementing an OPA-LiDAR on an autonomous driving vehicle.

3-D OPA has been proposed as a potential solution to this issue [141-147]. The basic concept involves emitting the beam by the end-fire array that provides a broadband high efficiency. However, unlike the end-fire array in 2-D OPAs that can only emit 1-D con-verged beams, the end-fire array in 3-D OPA can emit 2-D converged beams [141,146]. This requires multiple waveguide layers (more than 2) at the emitting end, which is different from the single-waveguide-layer configuration of PICs and significantly increases the complexity of fabrication. By employing ultrafast laser inscription (ULI) to directly write 3-D waveguides in silica, a hybrid 2D/3D OPA has been demonstrated. This approach enables a transition between a 1X16 2D array and a 4X4 3D array [141], as shown in Figure 14a. Nonetheless, this technique is not compatible with CMOS, and the waveguides produced by ULI have a low index, necessitating a significant gap between them. As a result, a relatively strong aliasing effect occurs. Conversely, a CMOS-compatible, active 3-D OPA has been suggested [142], as shown in Figure 14b. This involves utilizing multiple waveguide layers and incorporating phase shifters on each layer, allowing the light beam to be emitted from the device's edge, with the phase profile being actively adjustable.

The potential fabrication process for such a device is also discussed [143].

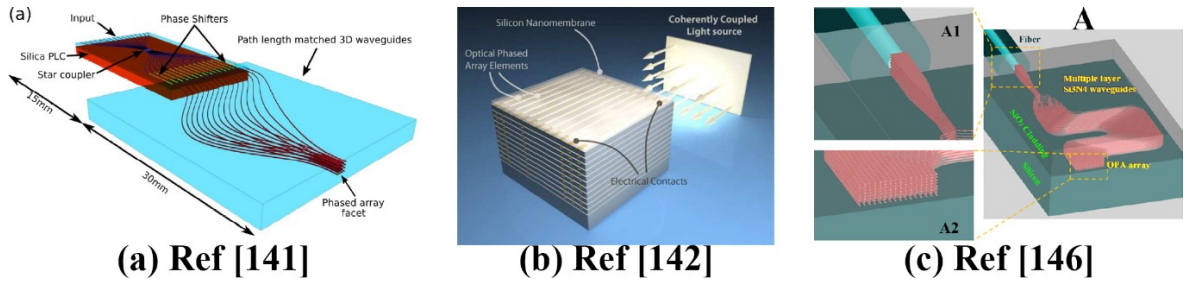

(a) Ref [141] **(b) Ref [142]** **(c) Ref [146]**

Figure 14: 3-D OPAs. (a) Hybrid 2D/3D OPA [141]. (b) Proposed active 3-D OPA [142]. (c) Passive 3-D OPA with proof-of-concept [146].

The manufacture of an active 3-D optical phased array (OPA) is either too challeng-ing or incompatible with CMOS technology. Conversely, a passive 3-D OPA can reduce the complexity of fabrication significantly while remaining compatible with CMOS technology [144-147]. A passive OPA with a multi-waveguide-layer design across the device can produce a 2-D converged beam through end-fire [144], as well as improve the cou-pling efficiency between fiber and on-chip waveguide [145], as shown in Figure 14c. Furthermore, a passive Ω-shaped region can enable beam steering via wavelength tuning, while an aperiodic arrangement can suppress the aliasing effect [146], eliminating the need to fabricate phase shifters on each layer and enabling fabrication. The manufacturing process is described in detail in [147].

1.7 Summary

The purpose of this paper is to provide an overview of the latest advances in photonic integrated circuit-based optical phased array (PIC-OPA) technology. The article begins by examining in detail the design considerations necessary to achieve optimal performance, such as larger steering capabilities, low aliasing, high optical efficiency, etc. It then delves into the phase

calibration process and outlines various system-level applications for OPAs. Finally, the article highlights a recently proven 3-D OPA configuration that has the potential to overcome a key obstacle in using OPA-LiDAR for autonomous vehicles by achieving high optical efficiency.

Chapter 2 Compound Period Grating Coupler for Double Beams Steering

2.1 Introduction

Emerging integrated photonics that studies the generation, processing, and detection of light in chip-scale optical media is one of the most important topics in modern optics research. One crucial topic in integrated photonics is the coupling of optical signals between optical fiber and photonic chips. With no need of exactly fine calibration compared to the butt coupler, an easy fabrication process compared to the prism coupler and the tapered butt coupler, the grating coupler has become a promising candidate [148-150]. A typical grating coupler on an SOI (silicon on insulator) wafer can be fabricated with two-step UV lithography [151].

Many studies have been done during the past decades, the traditional grating structure is modified in different ways to improve the fiber to chip coupling efficiency. For example, the whole gratings can be designed in shape of parabolas to focus light directly on the waveguide [152]. In [153], a binary period grating structure is applied to mimic the blazed grating. The polarization independence is achieved by a design of 2-D grating array [154], and also a non-uniform grating coupler structure [155]. In addition, the reflectivity of the substrate interface can be increased by a metal layer, and hence the directionality of the coupling is enhanced [156,157]. The thickness of the substrate can also be optimized to mitigate the leakage radiation [158]. Recently, a study is reported showing that the coupling efficiency can be as high as 93% [159].

In recent years, several research efforts utilizing the grating coupler to realize the coupling of light from photonic chips to free space have been undertaken, aiming at realizing spatial scanning with a beam generated from a photonic chip [12,86,54]. By designing an array of waveguide grating couplers, the 2-D scanning of free space is achieved [12,86]. In addition, with the help of photonic crystal to control the phase profile of the waveguide mode, the beam steering range (in unit of degree/nm for wavelength tuning steering) can be further enhanced [54], or even to eliminate the requirement of real gratings [55].

In this work, we report on a novel structure designed with a grating coupler of a compound period to generate two out-coupling beams simultaneously. The novel compound period grating coupler can generate two different series of surface harmonic waves at the same time; hence, the energy in the waveguide mode can couple into two different radiation modes. These two radiation modes both satisfy the grating diffraction equation, so they both will respond to wavelength tuning or refractive index tuning. Therefore, within a certain range of wavelength tuning, each of the two beams shows a steering range that is comparable to the range of the beam from a traditional single period grating coupler, the beam steering range of the new compound period grating coupler is approximately doubled compared to a single period grating coupler.

2.2 Coupling Mechanism

The traditional grating coupler has a single periodicity. In most studies concentrating on Si-based grating couplers, the device is on a SOI (silicon on insulator) wafer. Figure 15 shows the side cross-section of a typical SOI based grating coupler, it contains a 220 nm-thick Si waveguide

on top of an oxide layer with a thickness of 2 μm. This type of grating coupler is fabricated through two-step UV lithography. The Si layer of 220 nm is etched first to form the waveguide layout; secondly, waveguides are etched for 70 nm to form the grating structure on the waveguides.

The out-coupling angle of this grating coupler structure is governed by the grating equation, which is shown as [149]:

$$k_0 sin\theta = \beta_0 + m \cdot \left(\frac{2\pi}{\Lambda}\right), \quad (2.1)$$

where Λ is the periodicity of the gratings; θ is the out-coupling angle; k0 is the free space wavenumber; β0 is the propagation constant of the guided mode in the grating area; and m is the diffraction order, which in most cases is -1. This equation describes the phase match condition between the waveguide mode and the radiation mode. The term $k_0 sin\theta$ is the projection of the wavenumber of the radiation mode on the waveguide direction. When the propagation constant of the waveguide mode fits $k_0 sin\theta$, the energy will be able to couple from the waveguide mode to the radiation mode. The grating structure makes this possible as it generates a series of surface harmonic waves due to the periodical spatial fluctuation of the refractive index in the grating area, the electrical field distribution of the waveguide mode can be expressed as the sum of all the harmonic waves [150], that is:

$$\boldsymbol{E}_{grating} = \sum_{m=-\infty}^{\infty} \boldsymbol{S}_m \cdot e^{-j[\beta_0 + m(2\pi/\Lambda)]}, \quad (2.2)$$

where S_m is the amplitude of the mth order harmonic wave, β_0 is the propagation constant of the fundamental waveguide mode, and Λ is the periodicity. Here we label the term m(2π/Λ) as the altering factor of the harmonic wave. The propagation constant of the waveguide mode is altered

by this factor. In a typical grating coupler, one of these altered propagation constants exactly matches the wavenumber of a specific radiation mode, and the other propagation constants don't satisfy this phase match. Therefore, the energy in the waveguide mode is able to couple to this radiation mode, and the coupling efficiency tends to approach unity when the number of gratings increases. The reason that only one propagation constant satisfy the phase match condition is that the term sinθ in Equation 1 has to be in the range of (-1,1).

In principle, if a structure can generate different series of the surface harmonic waves with different periodicity, then the electrical field in the structure can be expressed as:

$$E_{grating} = \sum_{m_1=-\infty}^{\infty} S_{m_1} \cdot e^{-j[\beta_0 + m_1(2\pi/\Lambda_1)]} + \sum_{m_2=-\infty}^{\infty} S_{m_2} \cdot e^{-j[\beta_0 + m_2(2\pi/\Lambda_2)]} + \cdots + \sum_{m_n=-\infty}^{\infty} S_{m_n} \cdot e^{-j[\beta_0 + m_n(2\pi/\Lambda_n)]}, \quad (2.3)$$

In this case, there is a possibility that more than one harmonic wave can satisfy the phase match condition. Therefore, multiple out-coupling beams will be emitted from the structure.

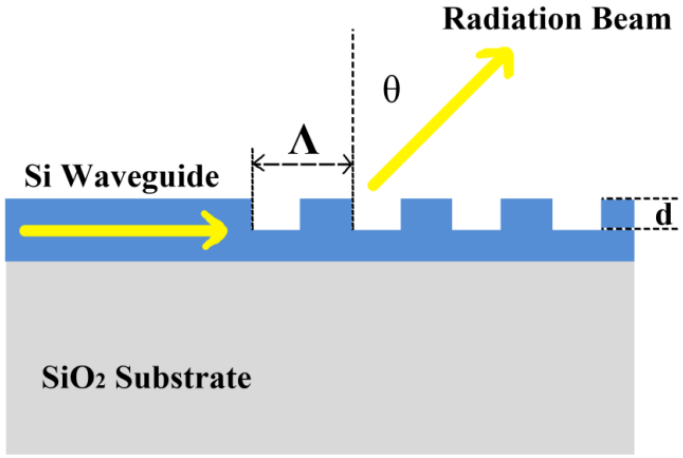

Figure 15: Illustration of single period grating coupler. Λ is the periodicity, d is the grating depth, and θ is the out-coupling angle.

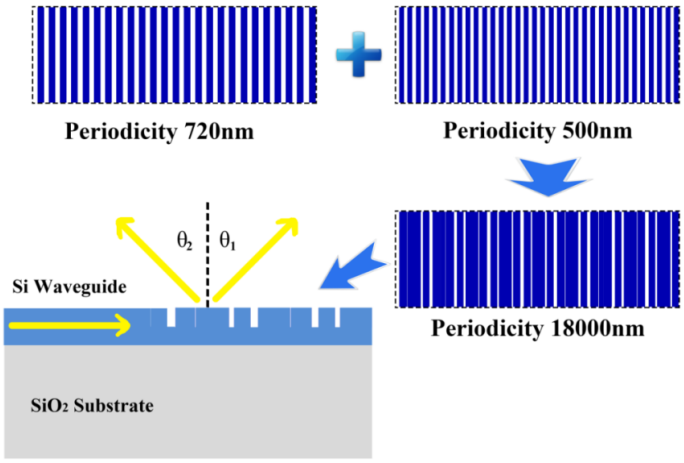

Figure 16: Illustration of the compound period grating coupler structure.

In this work, we design a grating structure in which the configuration of the grating is the combination of two gratings with different periodicities. Figure 16 shows the structure. We combine 25 gratings with periodicity of 720 nm and 36 gratings with periodicity of 500 nm to form a new grating structure with an envelope periodicity of 18000 nm; here we name the two gratings with single periodicity the component gratings and the new structure the compound period grating. This compound period grating is a mathematical union of the two component gratings. To ensure consistency with previous studies, the grating's thickness is 70 nm; the thickness of the waveguide layer is 220 nm; a 2 μm SiO2 substrate layer is placed below the waveguide layer; and only one envelope period of the compound period grating is considered in this work. The fill factor of the two component gratings is 0.5 and the new compound period grating has a fill factor of 0.64. The refractive index of Si and SiO2 are set to be 3.477 and 1.450 respectively at a wavelength of 1550 nm. In this work, the FDTD (finite difference time domain) is utilized. A sinusoidal pulse with TE polarization is applied to the Si waveguide for the simulation.

Because of the combination of the two periodicities, the electrical field distribution of the waveguide mode becomes the sum of two series of harmonic waves:

$$E_{grating} = \sum_{m_1=-\infty}^{\infty} S_{m_1} \cdot e^{-j[\beta_0 + m_1(2\pi/\Lambda_1)]} + \sum_{m_2=-\infty}^{\infty} S_{m_2} \cdot e^{-j[\beta_0 + m_2(2\pi/\Lambda_2)]}, \quad (2.4)$$

where Λ_1=720 nm and Λ_2=500 nm.

Hence, the phase match condition is satisfied between the waveguide mode and the two radiation modes at the same time. The first radiation mode forms a beam with an out-coupling angle θ_1 that satisfies:

$$sin\theta_1 = n_{eff} + m_1 \cdot (\frac{\lambda_0}{\Lambda_1}), \quad (2.5)$$

and the second radiation mode satisfies:

$$sin\theta_2 = n_{eff} + m_2 \cdot (\frac{\lambda_0}{\Lambda_2}), \quad (2.6)$$

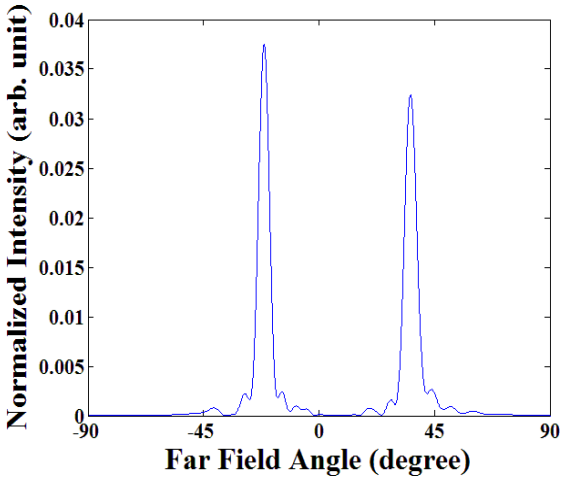

Figure 17: Far field simulation result of the compound period grating coupler with applied wavelength of 1550 nm.

Figure 17 shows the far field angle distribution of the compound period grating coupler at a wavelength of 1550 nm, calculated using the far field calculator. The intensity in the far field figure is automatically normalized and knowing how much energy is distributed in this far field pattern,

we are able to estimate the intensity of each beam. The ratio of the energy coupled to the air relative to the input energy for this wavelength is 31.60%; this ratio of the input energy is distributed in these two beams. The positive value in the far field angle is θ1 in Figure 16, and the negative value is the opposite, θ2.

As shown in Figure 17, when the input wavelength is at 1550 nm, two beams are generated by the compound period grating structure; the first has a far field angle of 35.67°, normalized intensity of 0.0324, and a FWHM (full width at half maximum) of 5.48°, while the second has a far field angle of -21.38°, normalized intensity of 0.0375, and a FWHM of 4.86°. The first beam is generated by the harmonic wave with the periodicity of 720 nm, and the second is generated by the harmonic wave with the periodicity of 500 nm, noted as Beam 1 and Beam 2 respectively. Beam 2 contains a slightly higher intensity and narrower FWHM, showing a better performance than Beam 1. This is because the 500 nm period grating has 11 more gratings than the 720 nm period grating. The SiO2 substrate has a higher refractive index than the air, so 56.86% of the input energy is coupled to the substrate, which is more than the energy coupled to the air (31.60%). Beside the energy coupled to the radiation modes, 4.86% of the light is transmitted; it keeps propagating inside the waveguide because the grating number of the structure is not large enough to couple out all the energy from the waveguide mode. 7.15% of the input energy is reflected, going to the opposite direction to the waveguide; this is because the spatial fluctuation created by the grating structure also forms a weak DBR (distributed Bragg reflector) structure, which results in the reflection.

To achieve solid-state beam steering, we utilize wavelength tuning in this work. Figure 18 (a) shows the far field angle contour map of the compound period grating structure versus the wavelength; we tested the wavelengths from 1300 nm to 1800 nm with an interval of 10 nm.

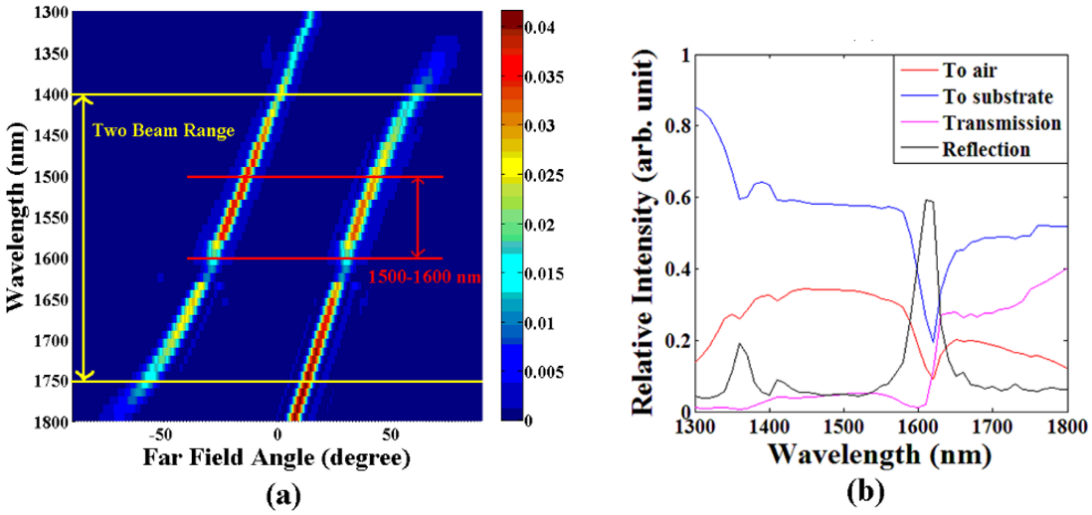

Figure 18: Performance of compound period grating coupler according to the applied wavelength. (a) Far field contour map; (b) Energy flow.

To be consistent with the previous studies, the beam steering range within wavelength of 1500 nm to 1600 nm is analyzed. As shown in Figure 18 (a), the red line indicates the beam steering range of the two beams at this wavelength range. Beam 1 varies from 42.59° at 1500 nm to 30.53° at 1600 nm and a beam steering range of 12.06° is achieved with only slight variation of FWHM (e.g. 5.73° at 1500 nm and 5.79° at 1600 nm). Beam 2 varies from -13.94° at 1500 nm to -28.08° at 1600 nm and the beam steering range is 14.14°. The FWHM of Beam 2 has a higher variation than Beam 1: it is 4.50° at 1500 nm and 5.85° at 1600 nm. While the maximum value of the FWHM of Beam 2, 5.85°, is still comparable with Beam 1, so the function of the compound period grating coupler will not be influenced by the slightly higher variation of the FWHM of Beam 2. The total

beam steering range is calculated by adding the two beam steering ranges is 26.20°. As a comparison, the previous study with a single period grating structure achieved a beam steering range of 14.10° in the same wavelength tuning range [12]. On the other hand, the two beams generated by the compound period grating structure have the steering range of 12.06° and 14.14°, they are both comparable to the single beam in the previous work [12]. Therefore, by using the compound periodicity of replace the single periodicity, the total beam steering range of the device is approximately doubled.

The yellow line in Figure 18 (a) indicates the total range of variation of the compound period grating structure. This range is selected because the intensity of both beams are sufficiently high. The total range of the wavelength is 1400 nm to 1750 nm. In this range, the far field angle of Beam 1 varies from 60.94° to 12.48°. When the wavelength is shorter than 1400 nm, Beam 1 gradually vanishes because Equation 5 is no longer satisfied. The FWHM of Beam 1 has a maximum value of 7.90° at 1400 nm in the two-beams range, and a minimum value of 4.53° at 1630 nm, so it can be observed that the Beam 1 is converged in the total two beam range. The far field angle of Beam 2 varies from 1.18° at 1400 nm to -58.02° at 1750 nm, and the whole steering range is 59.20°, which is 10.74° higher than Beam 1. This is because Beam 2 is created by the surface harmonic wave with periodicity of 500 nm, while the surface harmonic wave for Beam 1 has a periodicity of 720 nm. Therefore, according to Equations 5 and 6, the sensitivity of the far field angle to the wavelength of Beam 2 is higher than Beam 1. The FWHM of Beam 2 has a maximum value of 8.67° at 1750 nm and a minimum value of 4.07° at 1410 nm.

In summary, from 1400 nm to 1750 nm, Beam 1 covers the angle from 60.94° to 12.48° and Beam 2 covers from 1.18° to -58.02°; a total steering range of 107.66° is achieved with a wavelength tuning range of 350 nm (1400 nm to 1750 nm). In addition, the center angle range from 1.18° to 12.48 can also be covered in two approaches: one is to utilize Beam 1 at wavelengths higher than 1750 nm and the other is to utilize Beam 2 at wavelengths lower than 1400 nm.

The normalized intensity of the two beams is shown by the colormap in Figure 18 (a) which is calculated by the far field calculator. Figure 18 (b) shows the energy flow of the whole system where the red line is the energy coupled to the air and shows how much energy is distributed in the two beams according to the wavelength; the blue line is the energy coupled to the SiO2 substrate, which is higher than the energy to the air in the whole range; the pink line shows the transmission; and the black line shows the reflection.

In Figure 18 (a), both of the two beams are both weak at the wavelength around 1610 nm and Figure 18 (b) shows that a notable reflection peak appears at this wavelength where 59.29% and 58.61% of the energy is reflected at 1610 nm and 1620 nm, respectively. This may be because the two surface harmonic waves with periodicity of 720 nm and 500 nm both form a weak DBR structure and they both show a high refection at this wavelength, thus resulting in an especially high reflection peak at the wavelength at 1610 and 1620 nm. On the other hand, the lowest value of the energy coupled to the air is 9.00% at the wavelength of 1620 nm, while the highest energy to the air in the two-beams range is 34.30% at the wavelength of 1470 nm; thus, the lowest energy coupled to the air (9.00%) is 26.24% of the highest (34.30%). It can also be observed from Fig.

2.4 that when the wavelength is close to 1300 nm or 1800 nm, one of the two beams gradually vanishes, resulting in a reduction of the energy coupled to the air. When the energy to the air drops, the reduced part of the energy either couples to the substrate or stays in the waveguide mode. In summary, the compound period grating coupler shows a good performance in the whole two-beams range with an exception at 1610-1620 nm. Due to the high reflection peak, the intensity of the outcoupling beams show a minimum value at 1620 nm, which is approximately one fourths of the maximum intensity at 1470 nm. In real case, this issue may be a problem to some of the applications such as solid-state Lidar, which requires a high beam intensity to achieve a long detection range. So, in these kinds of applications, researches may want to avoid to utilizing the wavelength tuning at this wavelength range. While the fact that the minimum intensity is still about one fourths of the highest also shows the possibility that this wavelength range is still applicable in some case when the requirement of beam intensity is not extremely tight.

By using this compound period grating coupler, the energy coupled to the air is shared by two beams, so, if we assume the light source is constant, this fact means the increased beam steering range is achieved with a cost of decreased beam intensity. This gives us a chance to balance the tradeoff between the beam steering range and the beam intensity.

When this compound period grating structure is applied to some of the applications such as solid-state Lidar, an on-chip solution to distinguish the reflection signal from the two beams at the detection end will be necessary. In a previous study, an on-chip photodetector that can detect the direction of the incident light is reported [160]. In this work, a metal wall is integrated on the chip

that separate two adjacent photodiodes in the same area. When the incident signal has an angle to the normal direction, one of the photodiodes will be illuminated the whole area, while the other is only illuminated a part of the area because of the metal wall forming a shadow, so by carefully comparing the different response from the two photodiodes, the incident angle of the signal can be distinguished. In principle, this work can be applied to our work to distinguish the two beams generated simultaneously. Of course, this is only one of the data processing solutions for the practical Lidar application.

2.3 Compound Period Grating Structure with DBR Substrate

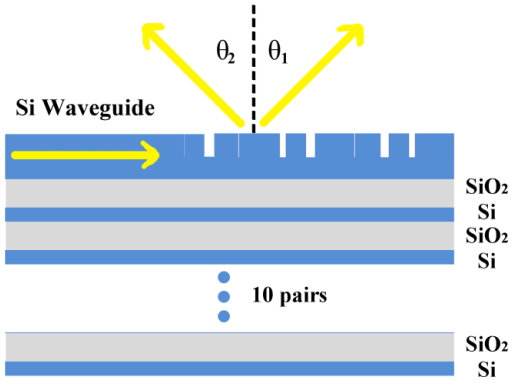

Figure 19: Illustration of the compound period grating structure with DBR substrate.

One serious problem of the grating coupler with SiO2 substrate is that when the energy is coupling from the waveguide mode to the air, the energy leakage to the substrate can reach over 50%. The reason for this problem is that the SiO2 substrate has a refractive index higher than 1, so it is easier for the energy to couple to the substrate than to the air. From Figure 18 (b) it can be observed that there is a considerable amount of energy coupled to the substrate. This problem also happens when the grating coupler is used for fiber to chip coupling, one possible solution for this

problem is to utilize a metal layer at the substrate to suppress the energy leakage [9,10]. In this work, we utilize the DBR (distributed Bragg reflector) structure as the substrate to achieve the energy leakage suppression and remain the device to be Si based only. Figure 19 illustrates the compound period grating structure with a DBR substrate.

In this work, Si and SiO2 are selected to create the DBR structure with a center wavelength of 1550 nm. The thickness of the Si and SiO2 layer are set to be 111.45 nm and 267.24 nm, respectively. Ten pair of the Si/SiO2 stacks are applied in this work. To fabricate such a device, a more complicated procedure will be need. First, DBR with ten pair of the stacks will be fabricated. Then, the top surface of a SOI wafer will be bounded to the DBR layers, and the buried oxide layer and substrate Si layer will be eliminated by dry etching. Ultimately, the grating coupler structure will be fabricated on the left Si layer. This complicated procedure will ensure that the grating coupler is fabricated from a single crystalline Si layer.

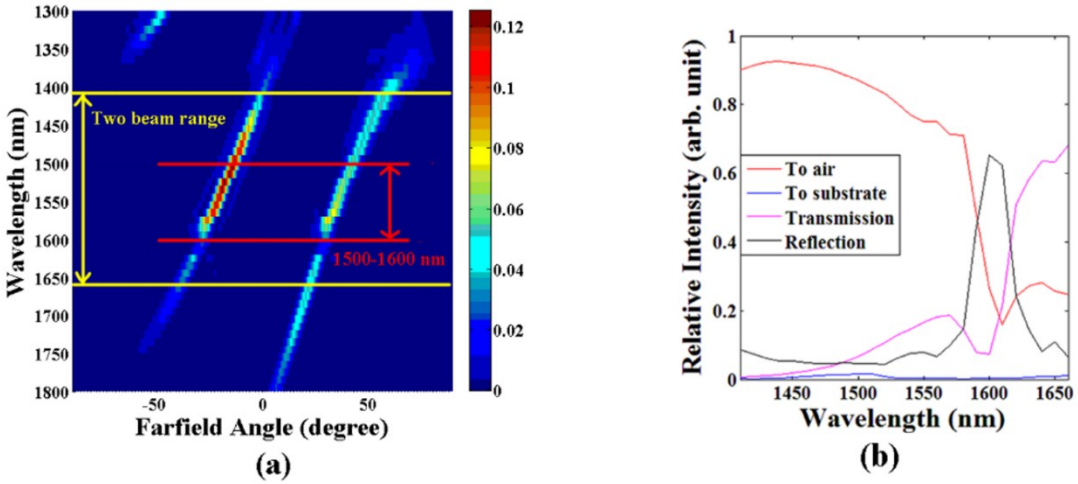

Figure 20: Performance of compound period grating coupler with DBR substrate according to the applied wavelength. (a) Far field contour map; (b) Energy flow.

Figure 20 shows the far-field angle contour map and the energy flow diagram of this structure.

From Figure 20 (a), it can be observed that the total two beam range is reduced, the beam steering range of the two beams is 73.70° in total. The red arrow shows the beam steering range of 26.67° within the wavelength of 1500 to 1600 nm is similar to the SiO2 substrate structure.

From Figure 20 (b), the most important advantage of the DBR substrate structure can be seen, namely, the energy leakage to the substrate is suppressed in the whole two-beam range. The DBR structure is a typical 1-D photonic crystal, as a result, the energy in the waveguide mode is almost impossible to couple to the radiation mode to the substrate. In this case, the intensity of the two beams coupled to the air is enhanced. It can be noticed from Figure 20 (b) that as the wavelength becomes greater, the grating coupler shows a reduced ability to couple the energy from the waveguide mode to the radiation mode, the energy in the transmission shows an increasing trend when the wavelength exceeds 1600 nm, that the energy stays in the waveguide mode; this problem could be solved by increasing the period number of the grating coupler, that the energy stays in the waveguide mode can be continuously coupled to the radiation mode by the addition gratings. In this work, the compound period grating contains 25 of the 720 nm periodicity gratings and 36 of the 500 nm periodicity gratings, and as a result, the transmission energy reaches over 50% when the wavelength is larger than 1590 nm. On the other hand, the two beams also vanish when the wavelength becomes shorter than 1400 nm, this is because that the coupling condition described by Equations 5 and 6 is no longer satisfied.

In summary, the compound period grating structure with DBR substrate shows an extremely low energy leakage, while the total beam steering range is also suppressed due to the enhanced

waveguide mode in the longer wavelengths. This gives us the potential to make a tradeoff between the beam intensity and beam steering range, depending on the real application of the device.

2.4 Fabrication Tolerance

In this work, the two component gratings are combined to form a compound period grating structure. However, the compound period grating structure contains several gaps whose widths are extremely small. The smallest gap has a width of 10 nm and considering that the depth of the grating is 70 nm, the aspect ratio of this gap is 7; structure with this high aspect ratio and small feature size is hard to fabricate using CMOS processing technology. On the other hand, the coupling between the waveguide mode and the radiation mode is achieved by the surface harmonic wave, therefore, the disappearance of some of the gratings in a large number of gratings will weaken the surface harmonic wave but not eliminate it.

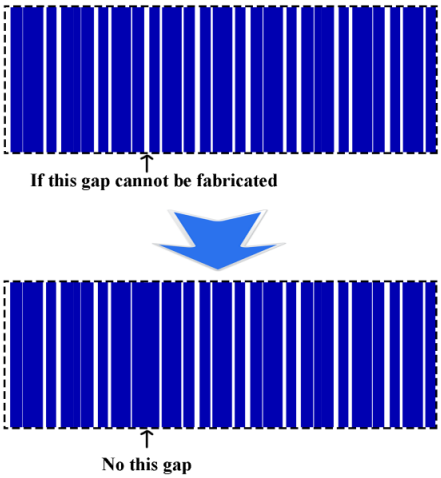

Figure 21: Illustration of the structure if some of the gaps cannot be fabricated.

Thus, we can predict that, if some of the narrow gaps cannot be fabricated, the whole performance of the device will not change too substantially. Figure 21 illustrates what the structure

is like if some of the gaps cannot be fabricated.

Figure 22 shows the far field contour map and the energy flow diagram when some of the gaps are not able to be fabricated. The traditional SiO2 substrate structure is considered in this result. Here we test all the gaps with a width under 100 nm, because a gap with 100 nm width and 70 nm depth can be in principle easily fabricated with E-beam lithography and dry etching in current COMS processing techniques.

x

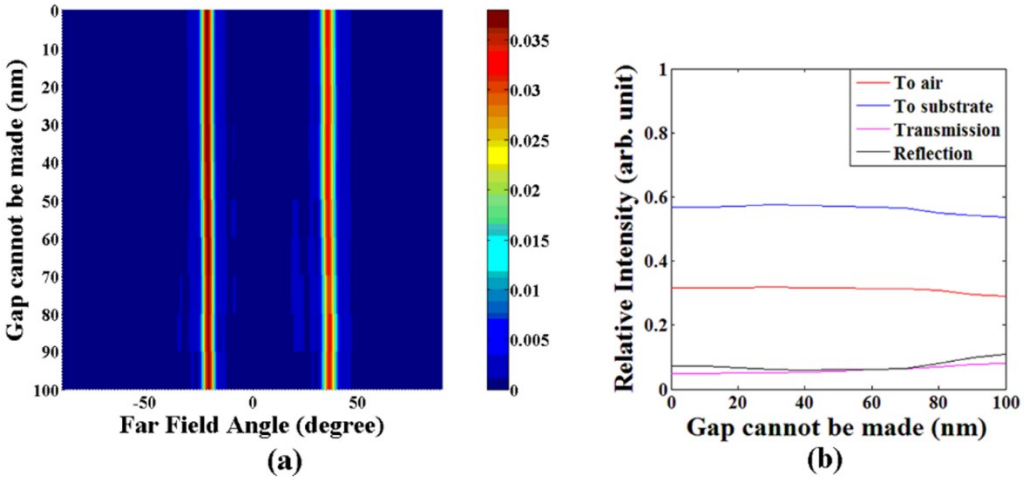

Figure 22: Performance of compound period grating coupler considering the fabrication tolerance of high aspect ratio gaps. (a) Far field contour map; (b) Energy flow.

Thus, we can predict that, if some of the narrow gaps cannot be fabricated, the whole performance of the device will not change too substantially. Figure 21 illustrates what the structure is like if some of the gaps cannot be fabricated.

Figure 22 shows the far field contour map and the energy flow diagram when some of the gaps are not able to be fabricated. The traditional SiO2 substrate structure is considered in this result. Here we test all the gaps with a width under 100 nm, because a gap with 100 nm width and

70 nm depth can be in principle easily fabricated with E-beam lithography and dry etching in current COMS processing techniques.

In Figure 22 (a), it can be observed that the far field angle of Beam 1 is 35.67° when all the gaps can be fabricated, and that it varies to 36.57° when all the gaps under 100 nm cannot be fabricated. A slight increase of the far field angle occurs because the total effective refractive index is also increased when the air gaps are replaced by Si. The FWHM of Beam 1 has almost no variation. Beam 2 has the same trend as Beam 1: the far field angle in Figure 22 (a) varies from -21.38° to -20.42°.

2.5 Conclusion

In this work, we propose and numerically it can be concluded that the compound period grating structure has a good performance in the whole two-beams range the compound period grating structure. With this design, the traditional grating coupler can be modified to generate two out-coupling beams simultaneously and because of the extra beam, the beam steering range of the device is doubled. A total beam steering range of 26.20° is achieved within a wavelength tuning range of 100 nm (1500 nm to 1600 nm). In addition, this result can potentially be improved through optimization and by combining with other studies, such as using the photonic crystal as the waveguide [11]. Furthermore, the DBR substrate structure study shows an enhanced beam intensity while the steering range is slightly suppressed. It is shown that there exists a tradeoff between the beam intensity and the beam steering range. The fabrication tolerance of the compound period grating structure is studied in consideration of cost efficiency and the result show

that the structure retains good performance even if all the gaps under 100 nm cannot be fabricated. Thus, the compound period grating structure has great potential for many applications such as telecommunication and sensing, especially for solid-state Lidar technology.

Chapter 3 Phase-Combining Unit for Aliasing Suppression in Optical Phased Array

3.1 Introduction

Integrated optical phased array (OPA) devices have attracted considerable research efforts in the past decades. Due to the promising performance in solid-state Lidar (light detection and ranging) technology, tremendous progress has been achieved in autonomous driving applications.

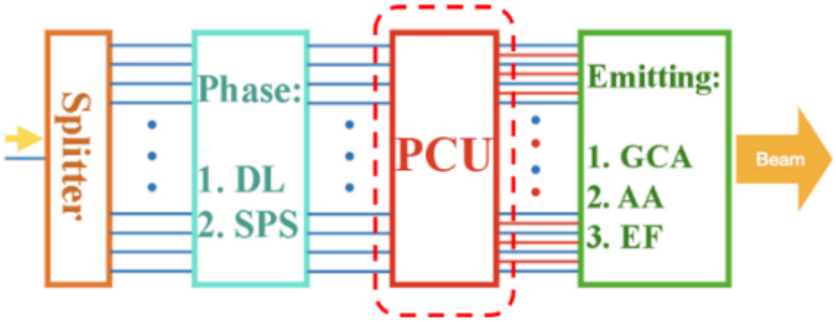

Figure 23: Illustration of an integrated OPA-based solid-state beam steering device. DL: delay length, SPS single phase shifters; GCA: grating coupler array, AA: antenna array, EF: end-fire emitter; PCU: Phase-combining unit.

Starting from the earliest study on an OPA beam steering device in Lidar applications in 2009 [12], many designs like ultra-high Q resonances in metallic structures [161] and novel tunable materials [162] have been proposed. A typical OPA based beam steering device can be illustrated in Figure 23 without the red circled part. From left to right, the starting point is a single light source, which is usually built with an external laser at NIR (near-infrared) wavelength with or without wavelength tuning capability. After the light is coupled from the fiber to the on-chip waveguide, the light will be split by a star-coupler or Y-splitter tree followed by the phase tuning part. Many

studies have been done for the phase tuning method. One simple approach is to utilize the dispersive effect by designing suitable delay lines in different waveguides [75,144]. This principle is further developed in [46] to get a sizeable emitting aperture. Compared to the wavelength tuning method, using individual phase shifters for every waveguide is a more comprehensive and practical approach; it leads to an N (phase shifter) to N (emitter) phase control. Progress has been made with this concept, including purely Si-based EOPS (electro-optics phase shifter) [73], optimization of waveguide thickness [36], single-chip optical and electronic approach [163], and ultra-efficient low-power TPS (Thermo Phase Shifter) [72]. Once the phase is well organized, the light is emitted by waveguide grating coupler array [50,54], grating antenna array [28,47], or end-fire emitters [141].

Individual phase shifters can offer the best phase tuning capability; however, this scheme comes with some issues. An OPA device would always be expected to have a large emitting aperture to achieve a high resolution. In addition, small pitches between emitters are also crucial to suppress the aliasing effect, enhancing the beam steering capability and the primary beam light efficiency [9,37]. Therefore, lacking sufficient emitters would normally result in a strong aliasing effect.

An obvious way to satisfy both large emitting aperture and small pitch is to have many waveguides and thus many phase shifters. However, having so many phase shifters is always impractical in design, fabrication, and operation; it requires complicated electronic hardware [76]. Despite presenting a much higher design difficulty, an aperiodic arranged emitter can also help the

aliasing suppression [20,26]. Another indirect approach to address this issue is designing an optics structure to enable the control of more emitters by using fewer phase shifters. Nevertheless, the emitters have their own phase requirement; such designs will not be trivial. One previous work has been done [81], which used 2N phase shifters to control N^2 emitters. Nevertheless, that structure works for antenna arrays, which cannot have the small pitch due to the footprint of antennas, and thus cannot present the best aliasing suppression.

In this work, we proposed a phase-combining unit (PCU) to help the aliasing suppression due to insufficient emitters. The PCU works in an OPA device after the phase tuning part and before the emitters, as illustrated by the red circled part in Figure 23. It enables the control of 2N-1 emitters using N phase shifters. The PCU is compatible with grating coupler array and end-fire emitters, so that a small pitch is possible.

3.2 Mechanism

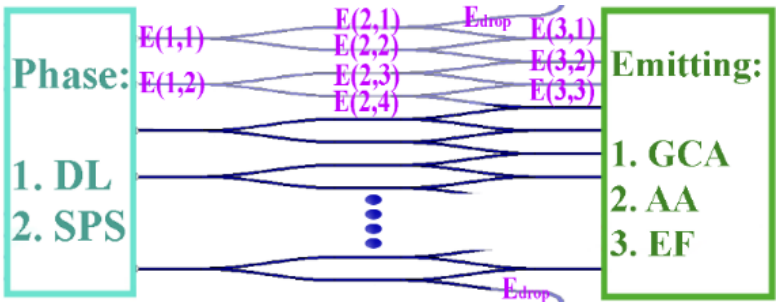

Figure 24: Illustration of the PCU. The device is in between the phase tuning part and the emitters.

The phase of light in each waveguide will be finely tuned to satisfy interference requirements in the phase tuning part. Then common OPA devices will directly emit the light, and the light will be converged in the farfield. However, a too-large emitting pitch may result in a strong aliasing

effect. As a comparison, in our design, the light will go through the PCU before being emitted.

The structure of the PCU is shown in Figure 24. It consists of two layers of Y-splitter; the output of the 2nd splitter layer will combine with the adjacent waveguides. All the Y-splitter must be symmetric to maintain the same phase change in the two outcomes in the design. According to the mathematical analysis in the supplemental material, every odd number output has the phase following the corresponding input; every even number output has the average phase of the two adjacent outputs. It can be described with the following equations:

$$E(3,1) = \frac{1}{2} \cdot E_m \cdot \exp(\varphi_1 + \varphi_{insertion}), \quad (3.1)$$

$$E(3,2) = \frac{1}{2} \cdot E_m \cdot \cos\left(\frac{\varphi_1 - \varphi_2}{2}\right) \cdot \exp\left(\frac{\varphi_1 + \varphi_2}{2} + \varphi_{insertion}\right), \quad (3.2)$$

$$E_{drop} = \frac{1}{4} \cdot E_m \cdot \exp(\varphi_1 + \varphi_{insertion}), \quad (3.3)$$

Therefore, all odd number outputs work as Eqn. 1, and all even number outputs work as Eqn. 2. The physical positions of the even number outputs are also right at the middle of the two adjacent outputs, so that the phases of these outputs exactly satisfy the OPA requirement. These even number outputs are the extra emitters created by the PCU layer. Because of these extra emitters, the PCU enhanced OPA device reduces the emitter pitch to half from its original design. This half pitch is very efficient in suppressing the aliasing effect.

Additionally, The PCU has almost no unique requirement in fabrication or operation. The only requirement is that the waveguides should be single mode with no crosstalk. Thus, PCU can potentially be designed with an output pitch as small as 1.3μm [36]. If this requirement is satisfied, PCU can help to suppress the aliasing effect without influencing any other performance in the

original OPA device.

Moreover, the PCU has two imperfections. Firstly, the intensity of the extra emitters is fluctuated by the term $\cos(\frac{\varphi_1-\varphi_2}{2})$, or $\cos(\frac{\varphi_{different}}{2})$ in Eqn. 2. Because of this, a PCU enhanced device works the best at the condition, $\varphi_{different} = 0^{\circ}$, when the beam is emitted in the normal direction. On the other hand, the device has the worst performance, at $\varphi_{different} = 180^{\circ}$; in such case, the device works just like there's no PCU with the total energy halved. Secondly, the PCU can only help with aliasing suppression but cannot offer extra beam steering capability. This is because the original phase shifters still control the extra emitters. The PCU enhanced device can suppress the aliasing effect as if it has half pitch but still steer the beam as itself.

Therefore, a PCU enhanced OPA device can use N phase shifters to control 2N-1 emitters. In conclusion, the performance of such a device (Device A) would be in between itself without PCU (Device B) and another device without PCU but has 2N-1 phase shifters (Device C). Device A would perform closer to Device C when it emits vertically, and closer to Device B when it emits to the side at $\varphi_{different} = 180^{\circ}$. Nonetheless, in the farfield emitting patterns, a PCU enhanced device (Device A) will never work worse than itself without PCU (Device B). In addition, considering the OPA devices usually only need to perform well in the center range, this drawback may not be too conspicuous.

3.3 Numerical Simulation

The PCU has been numerically studied by FDTD (finite difference time domain) simulation method. Device A, B and C have all been simulated for comparison.

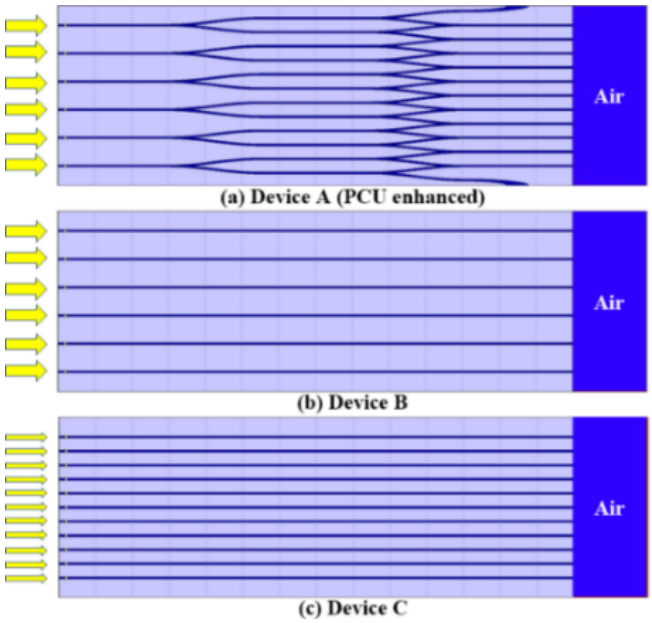

Figure 25: Illustration of the simulation structure. Light is coming from the left and emitting to the air on the right.

Figure 25 shows the structure of all 3 devices. Device B is a simple end-fire OPA device; Device A is the PCU enhanced version of Device B. Both Device A and B have 6 inputs so that they require 6 individual phase shifters to work. Device B has the same number of emitters, while Device A has 11 emitters, with 5 extra emitters created by PCU. Device C is set to be the comparison target which also contains 11 emitters; yet, since there's no PCU, it requires 11 phase shifters to work, almost doubled than Device A. The pitch for the input part of Device A and Device B is set to be 8μm, so the pitch for the emitter part of Device A and Device C is 4μm. It is worth noting that a relatively large input pitch of 8μm is purposely selected to generate more grating lobes so that it will be easier to observe the suppression of the aliasing effect. According to the theoretical analysis, the minimum pitch can be as small as 1.3μm at the emitter end [46]. Hence, it is expected that Device A would work better than Device B and perform close to Device C, meanwhile maintaining a much less requirement of phase shifters than Device C.

	$\pm 11.18^{\circ}$	$\pm 22.78^{\circ}$	$\pm 35.48^{\circ}$	$\pm 50.74^{\circ}$
DeviceA	6.99%	50.84%	7.16%	13.23%
DeviceB	93.70%	73.92%	47.19%	23.34%
DeviceC	0.71%	59.83%	0.28%	17.32%

Table 1: Power suppression ratio for simulated devices.

FDTD (finite difference time domain) method is utilized in the simulation. Besides the structure, all the other parameters, including material index, waveguide dimension, simulation mesh and duration are kept the same for the 3 devices. It is worth to note that the input number of 6 for Device A is selected due to the limited simulation capability. A comparison between simulation results with 4, 6 and 8 inputs has been made; the results are shown in the supplemental material. In summary, the results show that different input numbers have no influence on suppressing the aliasing effect. In other words, even though our simulated structure has only 6 inputs, the results and concept work for any number of inputs. For details, please check the supplemental material.

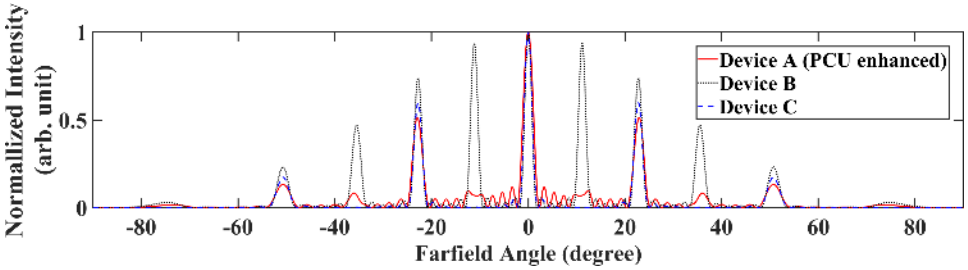

Figure 26: Simulation farfield's results for 3 devices with the main lobe at 0°. The intensity is normalized according to the main lobe.

Figure 26 shows the simulation result for the 3 devices at $\varphi_{difference} = 0^{\circ}$, so that the main lobe is emitted at 0°. The black dot line is the farfield result for Device B, which shows a strong

aliasing effect, grating lobes appear at ±11.18°, 22.78°, 35.48°, and 50.74°. The red line for PCU Device A and the blue dashed line for Device C shows a much higher similarity between each other than Device B; they both have the grating lobes at ±11.18° and 35.48° disappeared, while lobes at ±22.78° and 50.74° remains because of the 4um emitter pitch. Table 1 summarizes the power of the lobes as a percentage to the main corresponding main lobe for Device A, B and C when $\varphi_{difference} = 0^{\circ}$.

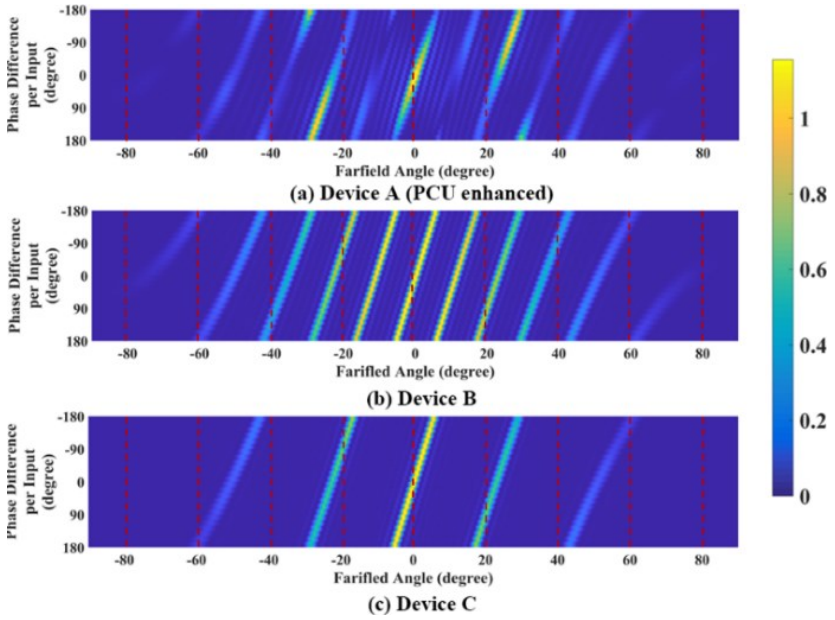

Figure 27: Simulation contour map for 3 devices with φ_different∈[-π,π]. The data are normalized in the same way as in Figure 26.

Compared to Device B, the PCU enhanced Device A shows an obvious aliasing suppression. Intuitively, its shape is similar to Device C, much more than Device B. From the data, the maximum aliasing suppression happens at the grating lobes at ±11.18°, the power of these two lobes is just 6.99% to the main lobe, compared to the 93.70% in Device B, about (93.70%-6.99%)/93.70%=92.54% of the power is suppressed. The grating lobes at ±35.48° also are

suppressed 84.83%. On the other hand, because of the 4um emitter pitch, the lobes at ±22.78° and ±50.74° only show the suppressions of 31.22% and 43.32%.

Figure 27 shows the simulation results for 3 devices with $\varphi_{different} \in [-\pi, \pi]$. With the change of $\varphi_{different}$, every lobe in all 3 devices steers linearly, the three main lobes all steer 5.3°. Device A shows an obvious aliasing suppression; the odd order grating lobes are suppressed much better than Device B, its performance is close to Device C at $\varphi_{different} = 0^{\circ}$, and close to Device B at $\varphi_{different} = \pm 180^{\circ}$. In summary, the simulation result agrees with the theoretical analysis.

3.4 Experiment Result

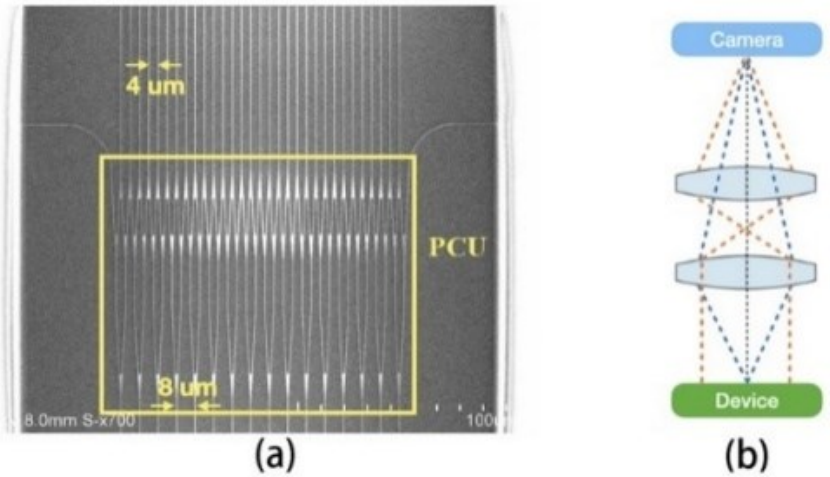

Figure 28: Illustration of the experiment. (a) SEM picture of the PCU before cladding. (b) Measurement setup, the blue line is for near field imaging, the orange line is for farfield capture.

The samples are fabricated in Lurie Nanofabrication Facility (LNF) at Ann Arbor, Michigan. Two samples according to Device A and B are fabricated for comparison. Both devices contain butt-coupling input couplers, 1×16 splitter tree, an Ω-shape delay-line region to enable wavelength tuning [46], and polished waveguide end for end-fire emitting. The delay length is set to be 20μm between each waveguide and the input pitch is set to be 8μm, which is consistent with the

simulation parameter. Device A contains PCU, so it has 31 emitters with 4μm pitch, while Device B has 16 emitters still with 8μm pitch.

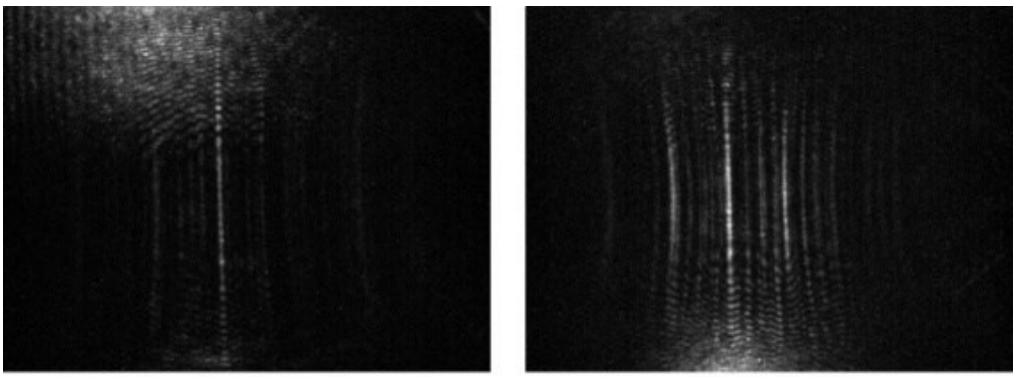

(a) Device A (PCU enhanced) (b) Device B

Figure 29: Farfield pattern of Device A and B with wavelength 1536nm.

The fabrication process is: first, the substrate SiO2 and the waveguide Si3N4 layers are deposited and patterned using LPCVD and optical lithography, then a cladding SiO2 layer is deposited by PECVD. The thickness of the substrate and the cladding SiO2 layers are set to be 2 um to eliminate potential leakage to the bottom Si wafer or the air, and the Si3N4 waveguide is set to be 600 nm thick and 650 nm wide. The last step is to dice the sample and polish the sidewall for light input and emitting. Figure 28a is the SEM picture of the PCU part in Device A before cladding. Figure 28b is the measurement setup, one lens is used for imaging the near field, and two lenses are used together to create a Fourier-optics field to capture the farfield. The detailed measurement setup is also introduced in the supplemental material.

There's only one waveguide layer, and the emitting is done by end-fire emitters, so that the devices indeed emit fan-beams. Figure 29 is the captured farfield result for the two devices when the input wavelength is at 1536nm. It is observed that Device A emits only 1 clear fan-beam inside

the FOV, whereas Device B emits 3 clear fan beams. In our measurement setup, we used butt couple for light input from fiber to waveguide, and because the fiber has a much larger diameter of field (~ 10μm, SMF-28-J9, Thorlabs) than the waveguide thickness (~600 nm), there are some scattering lights reach the camera through the cladding layer and the substrate layer, they can be observed at the top of Figure 29 (a) and bottom of Figure 29 (b).

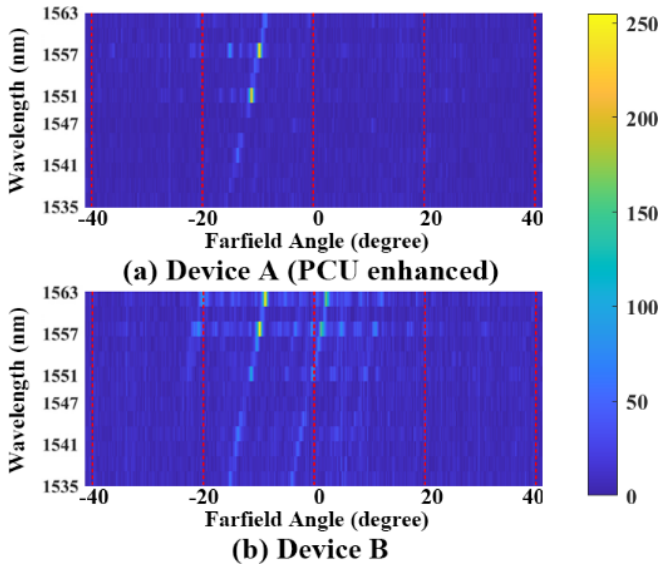

Figure 30: Experiment contour map. (a) Device A, only one clear beam can be observed. (b) Device B, multiple beams can be observed in the main region. The color represents the readout from the sensor with a range of (0, 255).

Figure 30 is the contour map of the experiment result. The beam shows an obvious intensity fluctuation with wavelength variations. This is due to the cumulative dispersive effect from all the optical components in the measurement setup. Despite the fluctuation, Device A emits only one distinguishable beam, which steers from -9.2° at 1563 nm to -17.2° at 1535nm. On the other hand, Device B generates two beams in the contour map; one steers from -8.8° to -16.5° and the other steers from 2.3° to -4.8°. In addition, the trace of the 3rd beam can be found at -20.0° at 1563 nm, and vanished at 1551 nm, again, due to the lens' limited NA. A very rough trace of the 4th beam

can also be found at approximately 13° at 1563 nm to 6.0° at 1535 nm, this is exactly where another grating lobe is predicted to be. It can be concluded that in Device A, the lobe should exist at from 2.3° to -4.8° is suppressed by the PCU layer. In Device A, this lobe merges into noise level and becomes indistinguishable, and the aliasing suppression ratio of this lobe is measured to be average 53.76% in the tested wavelength range.

3.5 Conclusion

In this work, we have proposed a phase combining unit (PCU) design to control 2N-1 emitters by using N phase shifters. We analyze the mechanism in theory. In addition, both the numerical simulation and experimental test results agree with the theoretical analysis. Compared to individual phase shifters and grating coupler arrays, we selected wavelength tuning and end-fire emitters for simpler experimental illustration, a proof-of-concept sample has been successfully tested. Additionally, the theoretical analysis explains that the PCU also supports OPA devices with individual phase shifters and grating coupler arrays. In conclusion, PCU can be used as a universal aliasing suppression unit on many types of integrated OPA devices.

Chapter 4 High Efficiency End-Fire 3-D OPA on Multi-Layers Si3N4/SiO2 Platform

4.1 Introduction

With the emerging applications such as solid-state Lidar (light detection and ranging), the beam steering based on integrated optical phased array (OPA) has drawn a lot of research efforts in the past decade [12]. Significant progress has been made including thermal tuning [58], electro-optics tuning [73], high sensitive wavelength tuning [55,105], integrated on-chip light source [6], side lobe suppression by aperiodic or apodized array placement [20,26,47], etc.

The traditional way in on-chip integrated photonic research usually utilizes the single waveguide layer structure, which is also the case of most studies on OPA. For example, in [12,58], the device structure could be sophisticated due to various requirements, while all containing only one waveguide layer, and because of this, the OPA formed by a single layer can only emit the exit beam upward. This is the reason for the relatively low emitting efficiency. When the OPA is placed in an environment that both its front and back side are uniform medium, the interference of light forms a beam not only to its front side, but also to its back side. In our previous work [50], we showed that a portion larger than 50% of light can be emitted to the substrate when an OPA is working in the case where its front side is air and back side is glass. However, as one of the main potential applications of integrated beam steering devices, the solid-state Lidar usually requires a detection range of over at least 100 m. The light emitting efficiency of the beam steering devices,

despite the development of light source and detector, is directly related to detection range of Lidar.

Several works have been attempted to address the relatively low efficiency challenge. In [24], a structure configuration to emit light from the edge of the chip is utilized. An ultra-converged beam is also achieved in [8]. Further works aiming to confine the waveguide spacing to half-wavelength have been done by various approaches [9,37]. However, these four works also employ the configuration of single waveguide layer. This does offer the convenience of tuning the phase of each waveguide [3,24,37], but the beam emitted by such a configuration is indeed a fan-beam, as the single waveguide layer can only form a 1-D OPA on the edge of the chip. The possibility of emitting a 2-D converged beam from the edge (end-fire) requires a 2-D OPA on the edge side. This is discussed in [141,143]. In [143], the performance of a 2-D end-fire OPA is numerically discussed, and a method utilizing nanomembrane transfer printing to fabricate a multi-layer structure with the top Si layer from SOI wafer is proposed and experimentally proved. In [141], a direct writing method based on ultrafast laser inscription (ULI) is applied to achieve a structure for the conversion between single-layer waveguides and 3-D waveguides, therefore, a 2-D OPA can be formed on the edge side.

In this work, we have studied a 3-D structure configuration based on multi-layer Si3N4/SiO2 platform to achieve a 2-D convergent beam emitted from the edge. This configuration can offer a high efficiency (compared to grating coupler based structure [55,58]), 2-D converged beam (compared to single layer end-fire structures [8,9,24,37]), its fabrication process can be CMOS compatible and suitable for mass production (compare to direct writing process [141]), in the

meantime, the pitch between each array elements in both horizontal and vertical direction can be controlled to be small (compare to 3-D OPA using direct writing technique [141]), thus the side lobe is suppressed and is far away from the main lobe; it also can achieve beam steering with only one degree of freedoms (compared to structures which require phase tuning on each waveguide [9,24,37]). We numerically demonstrate the performance of this structure. In part 2, the structure configuration is introduced and the main improvement on the energy efficiency in both the light input end and emitting end is discussed. In part 3, the simulation result of the 2-D converged beam is shown, the influence of vertical crosstalk, the engineering of delay length and the number of waveguide layers are also investigated. In part 4, the fabrication strategy is discussed, and the influence on fabrication error is discussed.

4.2 Structure Configuration

The structure configuration is as shown in Figure 31. The device consists of 6 Si3N4 layers with a thickness of 800nm, 5 SiO2 layers with 500nm thickness are sandwiched by the Si3N4 layers, which is shown as Figure 31 (b). Each Si3N4 layer is patterned, Figure 31 (c) is the top view of each Si3N4 layers, 8 waveguides with 800nm width are placed, the spacing between the center of each waveguide is 2um. In the red circled part, the length of the waveguides is gradually increased by a step of 6200nm.

In this work, we consider 8 waveguides in each layer. We assume that the device is powered by a fiber laser which is edge-coupled into the chip, which is as shown in Figure 31. Then a symmetric splitter tree is used to separate the light to multiple waveguides and ensure same phase

in each waveguide in the meantime. In this case, the waveguide number is limited to a power of 2. It's worth to note that even though only 8 waveguides are considered in this work, it is possible to have more in each layer by using a larger splitter tree [12]. The more waveguides are used, the larger the emitting aperture will be, and the emitting beam will be more converged.

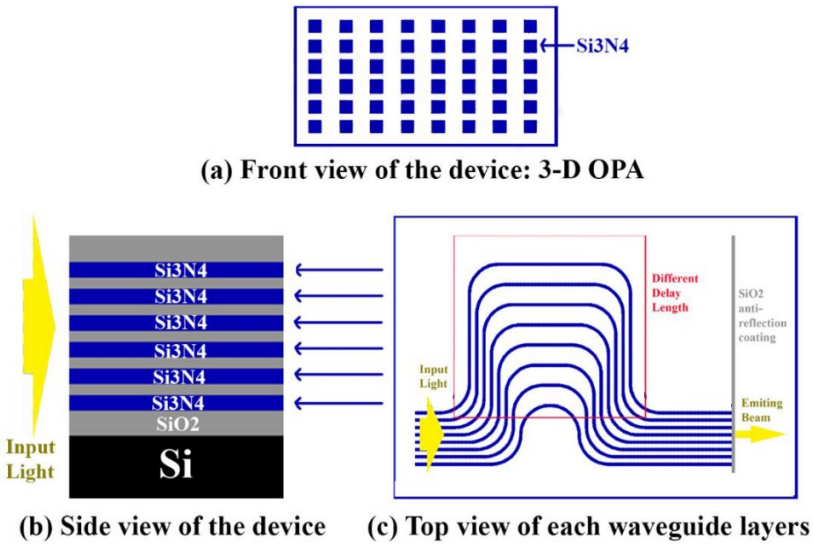

Figure 31: Illustration of the structure. (a) Front view: the 3-D OPA is formed on the front edge of the device, (b) Side view: cross-section of the device, 6 Si3N4 layers of 800nm thickness and 5 SiO2 layers of 500nm thickness, (c) Top view: pattern of each waveguide Si3N4 layers, contains 9 waveguides with 800nm width, spacing 2um.

After the fiber-to-chip coupler and the splitter tree, an Ω shape delay length structure is employed to create phase differences between the waveguides. The difference in the length between each of the waveguides is the same, and the 2μm periodicity can eliminate the crosstalk between waveguides, therefore, the phase difference between each array at the emitting end will be the same, which can satisfy the phased array condition in Equ. (1) in each waveguide layers (horizontal direction). In the vertical direction, since the structure in each of the waveguide layers are exactly the same, the phase difference between each layer is 0, so this also satisfies the phased

array condition between layers (vertical direction). Thus, this structure is able to emit a beam with 2-D convergence from the edge of the device. Equ. 4.1 shows the phase condition:

$$sin\theta = \frac{\lambda_0 \cdot \varphi}{2\pi \cdot d}, \quad (4.1)$$

where θ is the emitting angle, λ0 is the vacuum wavelength, φ and d are the phase difference and spacing between each array element.

The most important improvement of this structure will be the very high energy efficiency. This structure can achieve high efficiency in both input coupling part and the emitting part. In this paper, the input coupling part is discussed theoretically, and the emitting part is demonstrated numerically. First, in most of the previous studies, an external laser with single mode fiber is considered as the light source, however, the light will suffer considerable losses at the input coupling regardless of whether a vertical couple or a butt couple is employed., Particularly in the butt couple, the loss is usually significant because the thickness of the waveguide layer is usually ten times smaller than the mode field diameter (MFD) of a single mode fiber with a common core diameter of 8.2um. In this multi-layer structure, 6 Si3N4 layers and 5 sandwiched SiO2 layers occupy 7.3um vertically, thus, when the light is coupled from the single mode fiber to the on-chip waveguides, the coupling efficiency will be much higher than the coupling efficiency in single waveguide layer structures. There are at least two previous works which prove its high efficiency. Firstly, an edge coupler with silicon-nitride-assisted layers is presented in [164], in this work, two layer of silicon nitride with suitable size is fabricated above the Si waveguide, they perform a support function in the coupling between fiber and Si waveguide, a smallest insertion loss of

0.35dB (~92.3%) is reported. Secondly, a spot size converter using a similar coupling mechanism was presented in [165], it first couples the light from a single mode fiber to a tapered stack of Si3N4/SiO2 layers with similar size, then converts the spot shape to be a vertical line after the taper, and eventually couples the light to a Si waveguide with a much smaller size than the fiber. Based on the results, the mode overlap between the single mode fiber and the multi-layer spot size converter can be as high as 94%-99%. In that work, the thickness of Si3N4 layers is 225nm, while in this work, the thickness of the Si3N4 waveguide layers is 800nm, so the coupling efficiency may not be as high as their result, but we believe it is still obvious that the multiple Si3N4 layers can contribute to high input coupling efficiency.

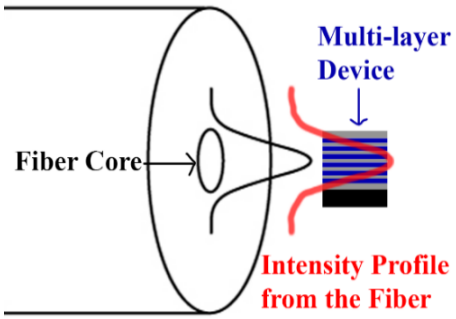

Figure 32: Illustration of the apodized intensity profile of the input coupling. The total thickness of the device is equivalent to the MFD of a common single mode fiber.

In [47], a uniformly distributed OPA is modified to perform a Gaussian-apodized intensity profile, this modification significantly helps the suppression of side lobes. In that work, the apodized field distribution across the array is purposely designed. On the other hand, the structure in this work (Figure 31) can automatically gain the Gaussian-apodized field profile because of the fiber-to-chip coupling. As shown in Figure 32, the single mode fiber contains a Gaussian-distributed profile, when the fiber is coupled to the structure, this profile will be transferred to each

layers, so the third and fourth layers contains equivalent intensity, and the intensity is gradually reduced towards the top and bottom. However, due to the symmetric splitter tree, the intensity in each arrays within same layer will be the same, so the Gaussian-apodized field profile can only be obtained in vertical direction (along layers) but not in horizontal direction (in same layer).

The high efficiency is also contributed by the emitting end. From Figure 31, it can be seen that the OPA is formed on the edge of the device, the front side of the OPA is the antireflection coating and air, which is a uniform medium, and an out-coupling beam can be generated by the interference between each array element. In addition, since the beam is end-fired into the air, the backward emitting is highly suppressed. Unlike the grating coupler based structure [55,58], there will be no leakage beam in the opposite direction with the emitting beam. From the simulation result, the out-coupling efficiency at the emitting end can be as high as 82%, the results will be discussed in part 4.3.

4.3 Results and Discussion

In this work, the FDTD (finite difference time domain) method is utilized to simulate the structure. In the simulation, the model is set exactly same as Figure 31, and a TM-polarized Gaussian pulse is applied as the light source, the pulse illuminates every waveguide. Wavelength range is set to be 1400nm to 1700nm, covering the 100nm wavelength tuning range which is used in [12]. Figure 33 shows the farfield pattern of the device at 1550nm. It shows that the device generates a clear main lobe at -1.41° horizontally and -3.8E-3° vertically, this lobe has a horizontal FWHM (full width at half maximum) of 4.99° and a vertical FWHM of 11.17°. Two side lobes in

horizontal direction can be observed at -52.49° and -47.39°. The formation of the side lobes is a result of the large horizontal pitch, while because of the periodicity (2μm) is not greater than the wavelength (1550nm), the side lobes are far away from the main lobe and not strong. On the other hand, the periodicity in vertical, which is the spacing between the center of each waveguide layers is 1.3μm, so only one clear main lobe is generated in vertical direction. The vertical FWHM is larger than horizontal FWHM, because the OPA covers only 7.3μm vertically, but 18.8μm horizontally, meaning that the horizontal aperture is larger than vertical aperture.

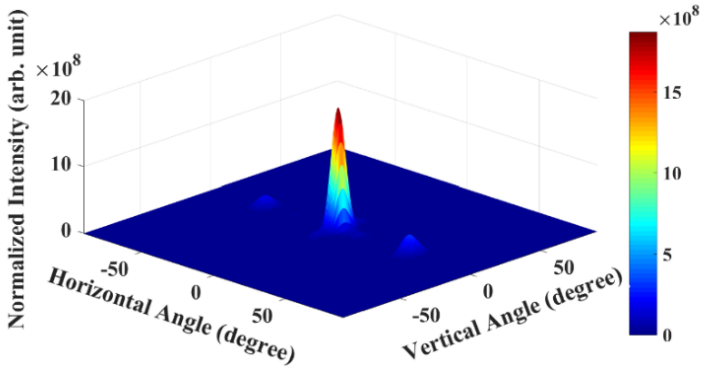

Figure 33: Farfield pattern of the device at 1550nm. A clear 2-D converged beam is emitted by the device.

The wavelength tuning performance of the device is shown in Figure 34. Figure 34 (a) is the horizontal farfield contour map, it shows that the main lobe can be steered by wavelength tuning, the beam is steered from 10.99° at 1500nm to -13.70° at 1600nm, a 24.69° steering range in 100nm wavelength range is achieved. This steering capability is achieved by the delay length structure, the length difference between each waveguide is fixed, so the phase difference between each array element in horizontal direction can be coherently changed by wavelength tuning. Figure 34 (b) is the vertical farfield contour map. There is no length difference between waveguides in different layers, so the phase difference between each array element in vertical direction is always 0 in

wavelength tuning, so the vertical farfield angle changes only slightly in the whole range, it only changes 4.8E-3°. Figure 34 (c) shows a comparison between the horizontal and vertical farfield angle. The beam steers linearly in horizontal direction with the wavelength variation, and the steering is ignorable in vertical direction. Figure 34 (d) shows the variation of horizontal and vertical FWHM, the convergence of the beam keeps in the whole wavelength tuning range, the horizontal FWHM varies less than 16.19%, and the vertical FWHM varies less than 10.18%. Figure 34 (e) shows the coupling efficiency in the tuning range, this efficiency is calculated by using the total energy emitted divided by the energy in all the waveguides right before the emitting OPA. The efficiency at the whole range is higher than 76.96%, a minimum value which appears at a wavelength of 1600nm, a maximum value of 82.41% can be observed at a wavelength of 1570nm. Because the main lobe dominates the whole range, the emitting efficiency of the main lobe is close to the efficiency value in Figure 34 (e). As discussed in part 2, the high efficiency is contributed by both the end-fire mechanism and the SiO2 antireflection coating.

The tuning function with purely horizontal steering is achieved by the wavelength tuning only. In this device, it is not required to have a precise control of the phase in each waveguide, and hence, the number of degrees of freedom required for operation is reduced from N (N is the number of waveguides in each layer) to 1, the operation principle is highly simplified. In the application of Lidar, the traditional mechanical Lidar rotates the whole device to achieve the horizontal field of view (FOV), and the vertical FOV is achieved by utilizing multiple beam lines vertically, this requires each beam to maintain its vertical angle during the rotation. The structure in this work can

satisfy this requirement: it can emit a 2-D converged beam that can be steered purely horizontally by wavelength tuning; so it is possible to utilize multiples of this device together, and setting them to emit in different vertical angle, thus a multi-line Lidar can be achieved.

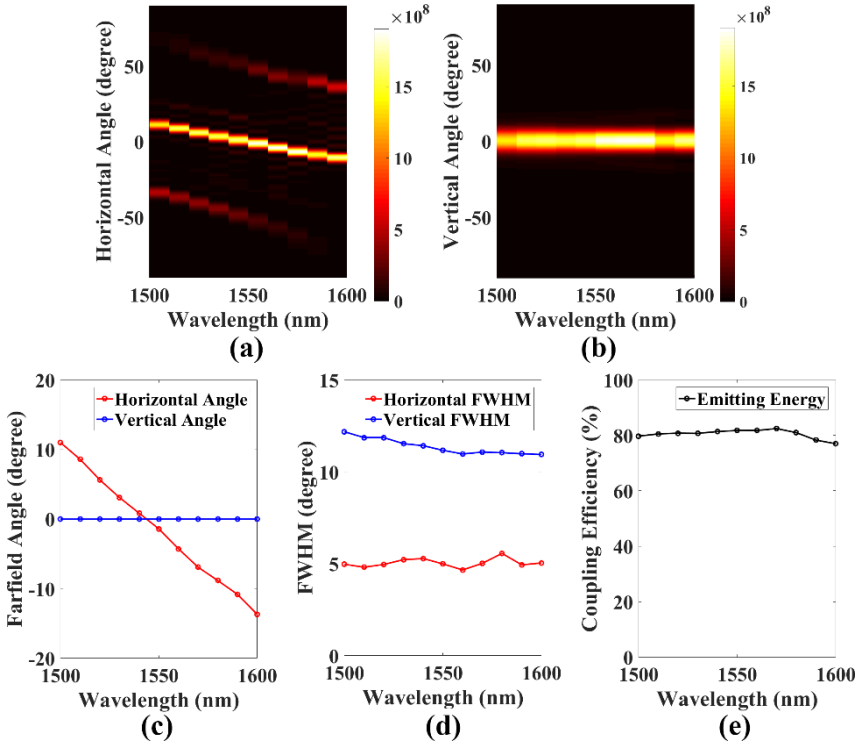

Figure 34: Simulation result of the structure in Figure 31. (a) Horizontal farfield contour map, a clear main lobe steers 24.78°/100nm, two side lobes can be observed, (b) Vertical farfield contour map, only one main lobe exists, no steering vertically (c) Comparison between the horizontal and vertical angle, (d) Comparison between the horizontal and vertical FWHM, (e) Coupling efficiency of the total energy emitted.

4.3.1 Influence of Vertical Crosstalk

The spacing between each waveguide in horizontal is selected to be 2um to eliminate the crosstalk, in consideration of the fact that the phase of light in each horizontal waveguides are different. On the other hand, the thickness of sandwiched SiO2 are set to be 500nm. Indeed, this thickness cannot fully eliminate the crosstalk between the waveguides in different layers. However, thanks to the exact same pattern in each waveguide layer, this crosstalk will not contribute to the

side lobes. This is because the phase difference between each layer is zero, and the intensity of the light in each layer are comparable, so the vertical crosstalk in the whole system is in a dynamic equilibrium. When the main light pulse in one waveguide induces a delayed pulse in the adjacent waveguide, this waveguide will also receive a delayed pulse induced by the main pulse from that adjacent waveguide, and since the main pulse in each waveguide have zero phase difference, the induced delayed pulse in these waveguides also have zero phase difference. In this case, all the induced pulse can also interfere with each other in the same direction with the out-coupling beam, so it also contributes to the main lobe. Another simulation is done to confirm this. The result is shown in Figure 35. In this simulation, we use 8 Si3N4 layers of 650nm, and 7 SiO2 layers of 300nm, so the OPA still covers a 7.3um range vertically, which is the same with the original structure in Figure 31.

The horizontal angle steering range shown in Figure 35 (a) is 23.00°/100nm, this is slightly different from the result in Figure 34, the reason for this difference is the waveguide thickness is changed in this structure, so it will change the effective index of the waveguide; however, the pattern in this structure is the same as the previous one, so the change is not large. Figure 35 (b, c) shows the vertical angle steering of this structure, it can be found, even though the SiO2 layers are only 300nm thick, the vertical angle of the beam is not influenced by the crosstalk. However, the vertical FWHM and efficiency become larger, this is because that even though the OPA covers the same range vertically, the proportion of waveguide layers is higher, so compared to the original structure used for Figure 34, this structure is more close to a thick slab waveguide with thickness

of 7.3μm. While in either case, the results in Figure 35 is a clear evidence to show that the vertical cross-talk between waveguides does not influence the angle of emitting beam.

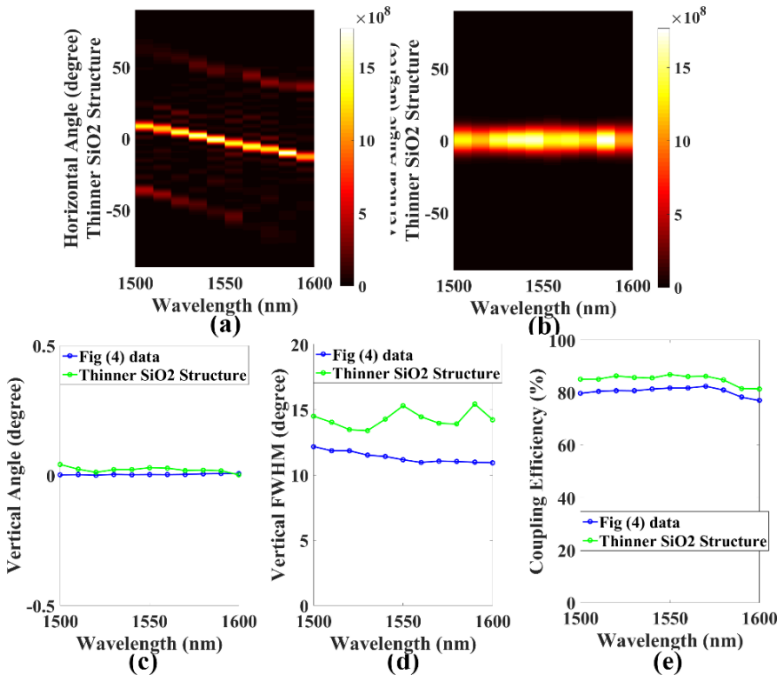

Figure 35: Simulation result of the thinner SiO2 structure (8 Si3N4 layers with 650nm thickness and 7 SiO2 layers with 300nm thickness). (a) Horizontal farfield contour map, (b) Vertical farfield contour map, (c) Comparison of vertical angle between the thinner SiO2 structure and the original structure, (d) Comparison of vertical FWHM, (e) Comparison of coupling efficiency.

4.3.2 Engineering of the Delay Length

We have pointed out that the horizontal convergence of the device can be further enhanced by using more waveguides in each layer. So, in the real case, the detection resolution of a wavelength tuned Lidar depends on the steering sensitivity per wavelength and the wavelength tuning resolution of the light source. In this work, we select 6200nm as the delay length of the structure; while in real application, the delay length can be selected to be larger in order to increase the steering sensitivity. Two simulations with delay length of 5400nm and 7000nm are done, the

results are shown in Figure 36.

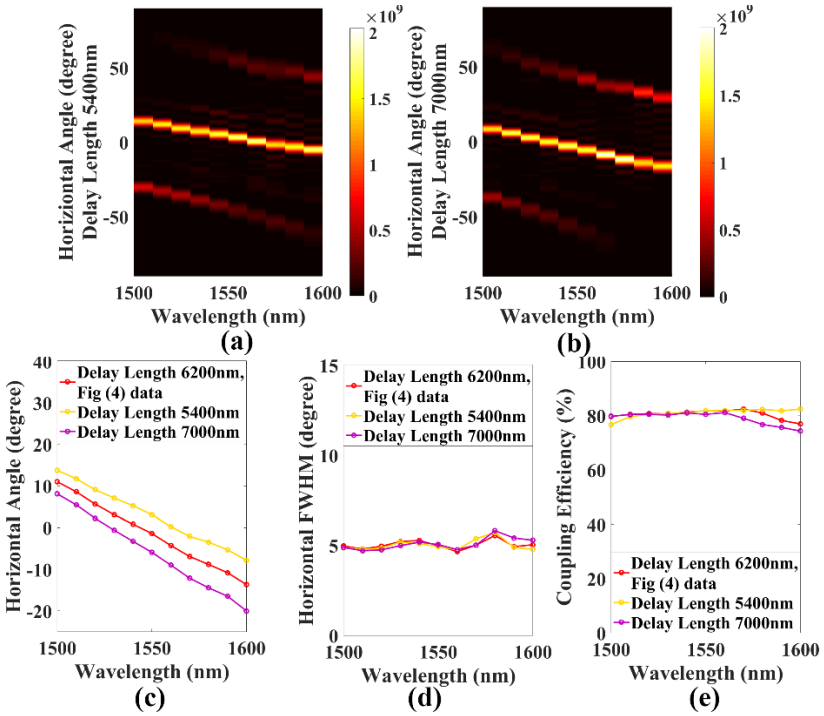

Figure 36: Simulation result of structures with different delay length (5400nm and 7000nm). (a) Horizontal farfield contour map of the structure with delay length of 5400nm, (b) Horizontal farfield contour map of the structure with delay length of 7000nm, (c) Comparison of horizontal angle between the structures with different delay length (original 6200nm, 5400nm, 7000nm), (d) Comparison of horizontal FWHM, (e) Comparison of coupling efficiency.

The difference between the structures in this simulation is in the pattern of each waveguide layer, so only the information about the horizontal angle is plotted in Figure 36. The most important comparison is in (c), where the red curve is the same as that of the red curve in Figure 34 (c), the yellow curve is for the structure with 5400nm delay length and the pink curve is for 7000nm delay length. The steering sensitivity of 5400nm delay length structure is 21.58°/100nm wavelength, is 24.69°/100nm for the original device with delay length of 6200nm and is 28.13°/100nm for delay length of 7000nm. This indicates that the steering sensitivity can be changed by selecting different delay length. In most cases, a larger delay length will be preferred to achieve higher steering

sensitivity, while in some cases, if the wavelength tuning resolution of the light source is limited, it may require a lower steering sensitivity to increase the detection resolution, this can be done by selecting a smaller delay length. In the meantime, the horizontal FWHM and coupling efficiency do not change much, because the spacing between each array element is kept constant in all the three structures.

4.3.3 Selection of the Number of Waveguide Layers

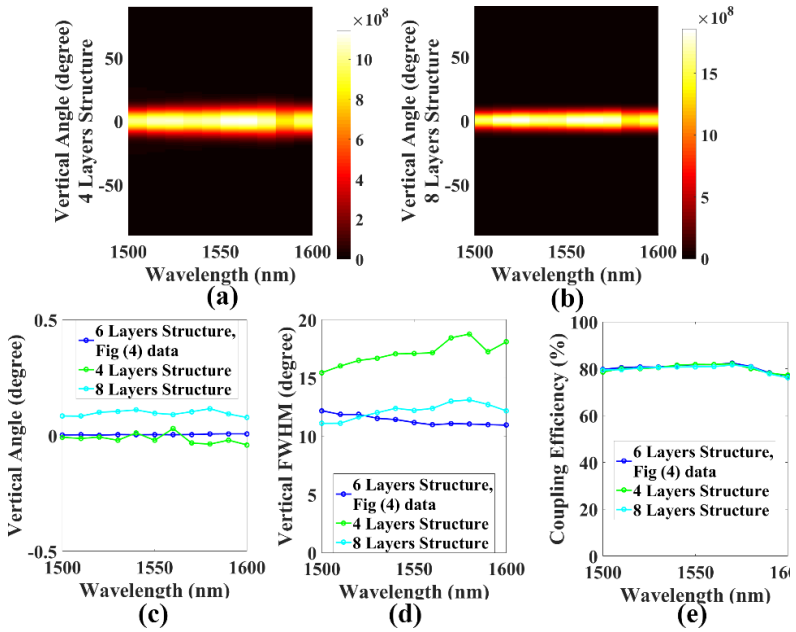

Figure 37: Simulation result of structures with different waveguide layers (4 layers and 8 layers). (a) Vertical farfield contour map of the structure with 4 waveguide layers, (b) Vertical farfield contour map of the structure with 8 waveguide layers, (c) Comparison of vertical angle between the structures with different waveguide layers (original 6 layers, 4 layers, 8 layers), (d) Comparison of vertical FWHM, (e) Comparison of coupling efficiency.

In this work, we select 6 Si3N4 layers to cover a range of 7.3μm in vertical direction, to ensure the total vertical size is not larger than the mode field diameter (MFD) of a common single mode fiber. In this structure, the number of waveguides in each layer can be increased by the beam splitter tree [12], while the number of the waveguide layers is limited by the MFD of the field. On

the other hand, as discussed in Sec. 2, the fabrication of multi-layer structure will become a challenge when more layers are required. So, the selection of how many layers to fabricate will be a tradeoff between the fabrication complexity and the device performance. In this work, we also investigate this parameter. Two structures which are exactly the same as the structure used for Figure 34 but only different in the number of waveguide layers are simulated, the results are shown in Figure 37.

4.4 Discussion on Fabrication Strategy

The fabrication strategy of this device is discussed as follows: This structure can be fabricated on a Si substrate. Firstly, a SiO2 layer of 2μm is deposited as low index substrate; secondly, 6 patterned Si3N4 layers and 5 un-patterned SiO2 layers are fabricated. The 6 patterned Si3N4 layers have exactly the same pattern, which is shown in Figure 31. There are two possible ways to fabricate this multi-layered structure. First, the method proposed in [24] can be utilized in this fabrication. The challenge in this method will be to control the planarization. This step influences the thickness of the sandwiched SiO2 layer, while the precise control of this thickness is crucial in this structure. Secondly, due to the identical patterns on each of the Si3N4 layers, it is possible to utilize the self-aligning method proposed in [143]. The fact that Si3N4 and SiO2 have a low etching selectivity with each other but have a high selectivity against Si also can help this method. The selectivity difference offers a possibility to etch down multiple layers of Si3N4 and SiO2 within the same etching step where a Si is used as the mask. However, the extremely high aspect ratio will be an obstacle here. It is more realistic to fabricate this structure with a combination of

the two methods: to use the self-aligning method to etch down 2-3 Si3N4 layers within one step, and then use the multi-step process proposed in [24] to get the 6 patterned Si3N4 layers eventually. As long as the self-aligning method can handle more than one Si3N4 layer in one step, (the aspect ratio of the hole in the etching step will be 1.2 um /2.1 um=0.57 in the case of etching down two Si3N4 layer and one sandwiched SiO2 layer at once), the total number steps required will be significantly reduced.

After the fabrication of 6 patterned Si3N4 layers and 5 un-patterned SiO2 layers, a final passivation SiO2 layer needs to be deposited. Following this, the wafer will be diced, and the edge of the die will be polished to ensure the input coupling from the external laser source and the output coupling at the emitting end. As the final step, a quarter-wavelength SiO2 layer (T=1550/(4*1.45)=267nm) will be deposited on the edge side, which can perform the antireflection function between Si3N4 waveguides and the air. The whole fabrication process follows the standard microchip fabrication process, so the method is CMOS compatible, and is suited for mass production.

The fabrication error is always an issue in CMOS fabrication process. There are two possible errors that can happen in this structure: waveguide phase error in same layer and the Si3N4 layer thickness error. In this work, we consider both the waveguide width and thickness to be 800 nm, while in real case, we don't require the waveguide to be exactly accurate. What we really need is that all the waveguides should be in same width, and all the Si3N4 layers should have same thickness. In this case, even though there are some phase error in every waveguide or some

thickness error in every Si3N4 layers, the OPA will still present desired phase profile.

The waveguide phase error is related to the quality of mask, photoresist coating, exposure, developing and etching process. In principle, all these factors can be controlled to a fine state, and there are some good works that could be examples to this issue. In [105], the structure contains a delay line region and a grating coupler array region, each of the regions contributes to one dimension of the beam steering, and the testing result shows good agreement with the theory, which suggests a good fabrication on the delay line region.

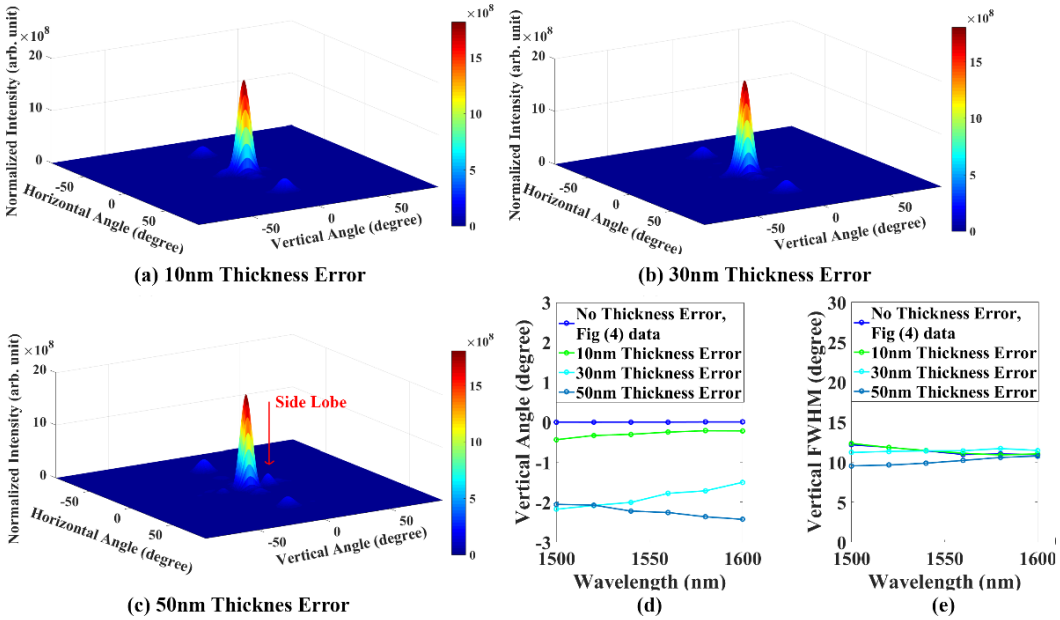

Figure 38: Simulation result of structures with 2 layers having thickness error. (a) Farfield pattern at 1550nm when thickness error is 10nm, (b) Farfield pattern when thickness error is 30nm, (c) Farfield pattern when thickness error is 50nm, (d) Comparison of vertical angle, (e) Comparison of vertical FWHM.

On the other hand, the thickness of each Si3N4 layers contributes to the vertical convergence on the beam, while the control on this factor is a little challenging, which is due to the variation in deposition environment, especially in the case of this structure, the upper layers need to be deposited after the patterning of lower layers, which means the layers cannot be deposited within

one pump down cycle.

To investigate this potential issue, we run a simulation with the same structure as shown in Figure 34 but by varying the thickness of the 2nd and 6th layers to a different value. We set this value to be +10nm, +30nm and +50nm, this is because most of the deposition method used in waveguide deposition (PECVD, LPCVD, magnetic sputtering PVD) can suppress the thickness error to be lesser than 50nm. The result is shown in Figure 38. It can be observed, that the farfield pattern of the thickness error of 10nm and 30nm shows only little difference. The vertical angle shifts a little bit to negative, which is probably because of the phase variation in the two thicker layers; the FWHM also shows only slight difference. However, when the thickness error becomes 50nm, a side lobe in vertical direction can be found right beside the main beam in the farfield pattern. The FWHM data also agree with this, the FWHM of the main beam becomes smaller in 50nm thickness error, this is because of the appearance of the side lobe suppresses the main lobe, due to the emerging side lobe is too close to the main lobe, it may suggest that a thickness error larger than 30nm will affect the performance of the whole structure.

4.5 Conclusion

In this work, a 3-D optical phased array (OPA) with the light exiting from the edge of the device, which is based on multi-layer Si3N4/SiO2 platform, is numerically demonstrated. The multi-layer structure can enable a high efficiency from both the input coupling and emitting coupling, the end-fire emitting efficiency can be as high as 82%. A 2-D converged beam is clearly generated in the farfield pattern of the emitting OPA, which can be steered purely horizontally by

wavelength tuning, which suggests a possibility to apply the device to build a multi-line solid state Lidar. The inter-relationship of the 3-D OPA structure is studied in detail: the vertical crosstalk doesn't affect the out-coupling angle; the length of delay line can be engineered to achieve either high steering sensitivity or high steering resolution; the number of waveguide layers can also be engineered as a trade-off between the fabrication complexity and device performance. The fabrication strategy is also discussed and the influence of fabrication error is investigated. In conclusion, this structure can be fabrication CMOS compatible, making it suitable for mass production. It also offers a 2-D converged beam which can be horizontally steered with control of only one degree of freedom. This work is promising for further study of solid-state beam steering devices and the application of solid-state Lidar, as well as in other emerging areas, such as wireless communication or optical microscope.

Chapter 5 PIC for Broadband High-Efficient 3-D OPA

5.1 Introduction

Photonic integrated circuits (PIC) have been studied for decades. Normal PICs are based on the silicon-on-insulator (SOI) platform, in this case, the top crystalline silicon is utilized to be the waveguide layer, and the electronic contact is fabricated above the waveguides. This method uses the mature CMOS-compatible fabrication process, developed over decades in the electronics integrated circuits (IC) industry. However, this standard process also confines the PICs to be in a single-waveguide-layer configuration, which limits the performance of some devices. A relatively young type of PIC, named optical phased array (OPA), which has drawn a lot of research attention due to its potential in the LiDAR application, is such a device that suffers from the limitation of single-waveguide-layer configuration.

Light Detection and Ranging (LiDAR) systems are used primarily for full dimensional sensing, with applications ranging from navigation for autonomous vehicles to robotics, imaging, unmanned aerial vehicles (UAVs), national security, healthcare, and the Internet of Things (IOTs) [166,167]. LiDAR systems use a light beam steering to capture distance information. LiDAR systems often use time of flight (direct or indirect) or frequency modulated continuous wave (FMCW) to determine distance/velocity for multiple points on the surface of an object [2,168]. To generate a 3-Dimensional (3D) map, the OPA system in a LiDAR must systematically scan an

object, taking into account both the distance and complexity of the object to be mapped. Mechanical systems to do this are slow and require frequent re-calibration, and this, along with the high cost, has limited the viability of LiDAR systems [169,170].

With the rapid development of the silicon-based CMOS-compatible fabrication process, which enabled large-scale integration of individual components on a chip, there is strong interest, in both the research and commercial sector, in developing a LiDAR system with most of the functional components on a single chip. We believe chip-scale LiDAR can provide both the increased range and resolution required for high-speed driving—and other tasks, such as real-time facial recognition—that is beyond the ability of current LiDAR systems. Chip-scale LiDAR can also better classify objects and improve movement tracking, at a lower cost. There are many open research questions that must be addressed to produce a viable chip-scale solution. LiDAR systems are most often discussed with respect to their application in autonomous vehicles, which rely heavily on automated methods for detecting the environment around them [2]. While current autonomous driving (AD) and advanced driver-assistance systems (ADAS) rely primarily on the use of traditional LiDAR, camera, radar, and sonar technologies, there is a growing interest in the use of integrated photonic sensors. Chip-scale LiDARs are well-positioned to play a pivotal role in the development of fully autonomous vehicles, which must continually scan their surroundings and react in real-time as conditions change. It is easy to imagine that the 3D mapping capabilities of chip-scale LiDAR have applications in other fields that would be of great societal benefit, including robotics, the Internet of Things (IoT), public safety, manufacturing, and health care. With

the growing interest from the research community in chip-scale LiDAR, beam steering based on the integrated optical phased array (OPA) has drawn a lot of research effort in the past decade [12]. Significant progress has been made, including thermal tuning [16,58], electro-optics tuning [73], high sensitivity wavelength tuning [55,105], integrated on-chip light source [86,170], and side lobe suppression by aperiodic or apodized array placement [20,26,47]. On-chip integrated photonic research is usually based on an SOI wafer, which forms a single-waveguide-layer structure, and this is used for most of the studies on OPA [12,58]. The OPA formed by a single layer can only emit the beam by a diffractive component such as grating couplers, which results in a narrowband and relatively low emitting efficiency. In previous work [50], we showed that about half of the light can be emitted to the substrate in a normal grating-coupler-based OPA. The optical efficiency of the beam steering devices is directly related to the detection range of LiDAR, and most applications (particularly for AD and ADAS) require a detection range of at least 100 meters. Designs can be applied to suppress substrate leakage of the energy [65,66], but only benefits in a narrow bandwidth.

Previous works have attempted to address the relatively low emitting-efficiency challenge. In [24], a structure configuration to emit light from the edge of the chip is utilized. An ultra-converged beam is also achieved in [8]. Further works aiming to confine the waveguide spacing to half-wavelength have been done using various approaches [9,37]. These works employ the configuration with a single waveguide layer and thus offer the convenience of tuning the phase of each waveguide [9,24,37]. Unfortunately, the beam emitted by such a configuration is a fan-beam

with only 1-D convergence, as the single waveguide layer can only form a 1-D OPA on the edge of the chip. The possibility of emitting a 2-D converged beam from the edge (end-fire) requires a true 3-D OPA on the edge side. In [143], the performance of an end-fire OPA is numerically discussed, and a method utilizing nanomembrane transfer printing to fabricate a multi-layer structure with the top Si layer from an SOI wafer is proposed. In [141], a direct writing method based on ultrafast laser inscription (ULI) is applied to achieve a structure for the conversion between single-layer waveguides and 3-D waveguides; therefore, we know that a 3-D OPA can be formed on the edge side, especially with the current CMOS compatible 3D circuitry on-chip [174]. This is the first reason that a multi-waveguide-layer configuration is helpful in an OPA device.

Another major issue for the optical efficiency is at the input coupling end. In most OPA studies, researchers considered using an external light source such as a pulsed or coherent laser. In such a case, fiber is needed to connect the light source and the OPA chip. In most studies, the frequency of light is usually utilized as one degree of freedom in either beam steering or distance detection (in the case of an FMCW Lidar), so a wideband coupling performance is desired for the fiber-to-chip coupler. As same as the case at the emitting end, the two standard coupler designs also have their issues: the edge coupler shows a wideband performance but usually suffers a significant coupling loss due to the mode mismatch between single-mode fiber and on-chip waveguide (which is generally at least one order smaller in size than the fiber) [175]; the grating coupler can offer a much better mode match, which leads to a high coupling efficiency, but only at a relatively narrower band [176]. To address this issue, wideband high-efficient couplers have been designed

by applying additional waveguide layers (usually Si3N4 layers) on the top of the silicon waveguide layer so that the fiber mode is first coupled to a super-mode in the nitride stack, then gradually coupled to the silicon waveguide by evanescent coupling [164,165]. This is the second reason that a multi-waveguide-layer configuration is helpful in an OPA device.

Using the edge coupler can generally offer a stable efficiency in a broad bandwidth. However, in the particular case of OPA devices, simply applying the edge coupler in the SOI platform will result in two disadvantages: 1. a mode mismatch at the input end, and 2. a beam with only 1D convergence at the emitting end. In this work, we have made one step forward to address both the disadvantages. By applying the multi-waveguide-layer configuration to the whole device, a true 3D Optical Phased Array has been demonstrated for beam steering, fully utilizing current CMOS 3D circuitry compatible processes [174], based on a novel Si3N4/SiO2 platform, with distinct characteristics: a) Vertical multiple-layers provide a broadband high power coupling efficiency to a 2-D converged beam. b) The Ω-shape design in the plane enables a beam steering capability that is unlimited in principle, and the highest proven beam steering is 0.577°/1nm wavelength in the 4-layer sample with 60 μm delay length. This is quite different from all previous standard 2D approaches leveraging grating couplers to synthesize 3D beams. As a proof of concept, we experimentally fabricated the multilayer OPAs and verified the concept with careful cauterizations.

5.2 Device Structure

The proposed device is illustrated in Figure 39. A single-mode fiber (SMF-28) and an on-chip edge coupler are utilized to couple the light from the source (a tunable laser) to the waveguides.

The mode match is supported by multiple waveguide layers so that a high coupling efficiency can be achieved. In addition, the thickness of Si3N4 waveguide layers and SiO2 isolation layers are selected to minimize vertical crosstalk. A taper waveguide is applied to convert the mode-size into single mode waveguides. The Y-splitter tree is then used to split the light into multiple channel (16 channels for every layer in Figure 39) with the phase in each channel to be the same. An Ω-shape delay line region is designed to enable the beam steering capability, a certain delay length is applied between every two waveguides, which creates a dispersion effect in this region, so that the emitting beam can be steered horizontally by wavelength tuning. At the emitting end, a 2D end-fire array is formed on the side of the device, the light is edge-coupled into the free space. The emitting efficiency is relatively high in a broad bandwidth due to the edge coupling. The beam shaping is achieved by the 2D array, in the horizontal direction, the phase profile of the array is controlled by the Ω-shape delay line region; and in the vertical direction, the phase profile inherits the profile from the input fiber as we purposely design every layer to be in the exact same pattern, so there's no phase difference between every layer. Si3N4 and SiO2 are selected to be the waveguide and cladding material with consideration of both device performance [177,178] and fabrication possibility.

As stated above, two disadvantages are generated by applying the edge coupler in the SOI platform, they are addressed in this work by utilizing the multi-waveguide-layer configuration over the whole device. In the rest of this paper, we firstly introduce the design of the input coupler, with the mode match supported by the multi-waveguide layer; then introduce the experimental results,

which is a proof-of-concept to show the broadband high efficiency and the 2D converged beam.

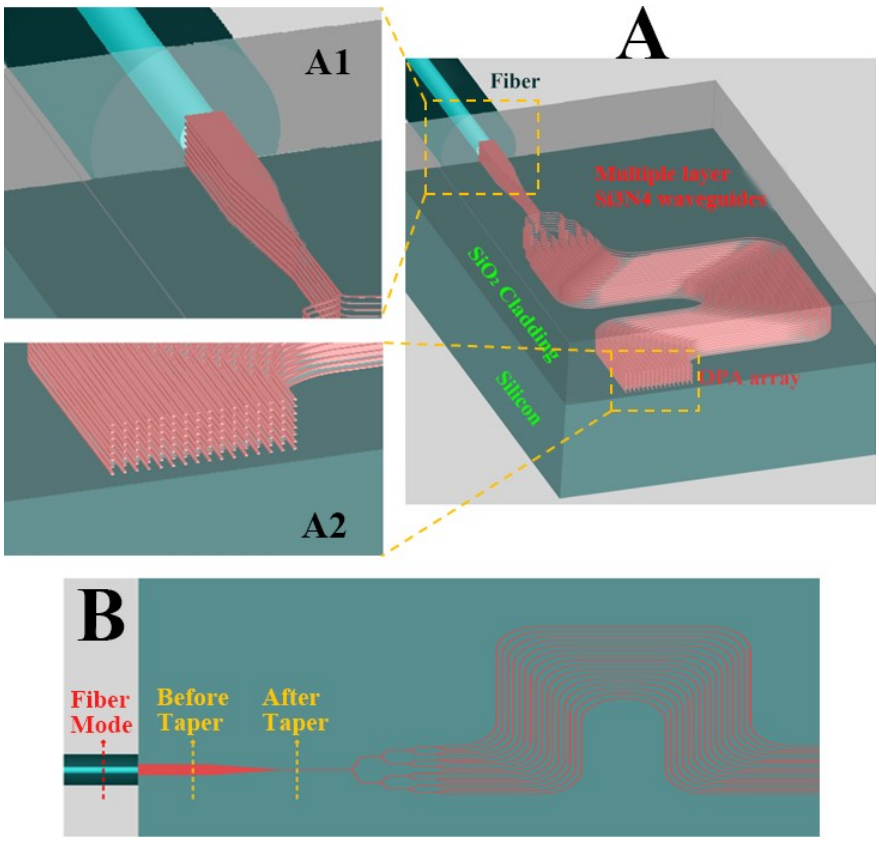

Figure 39: Illustration of the multi-layer Si3N4 3D OPA. (A) Schematic (3D view) of the structure. (B) Top view layout of the waveguide layers.

5.3 Design of the Input Coupler

The input fiber used in this work is SMF-28-J9 (Thorlabs), which has a mode field diameter (MFD) of 10.4μm. The layer thickness of the device is optimized to minimize the vertical crosstalk. With the selected layer thickness, it can be calculated that eight waveguide layers can cover the full MFD. We firstly analyze the mode profile for three positions: the fiber, the coupler before taper, and the single mode waveguide after taper; these positions have been labeled in Figure 39B.

As illustrated in Figure 40, both TE and TM polarization have been simulated. From the comparison between B&E and C&F, it can be found that the TM polarization has the field

distribution more into the cladding SiO2 layers, this is better for the fiber to waveguide coupling as it can offer a better mode match. However, this mode profile is not wanted in two aspects: firstly, it will increase the optical loss for all the components including waveguide, bending, and splitters; secondly, it is not helpful in minimizing the vertical crosstalk. On the other hand, the modes for the TE polarization are much more in the waveguide material, which is desired in this device. Therefore, TE polarization is selected in this work.

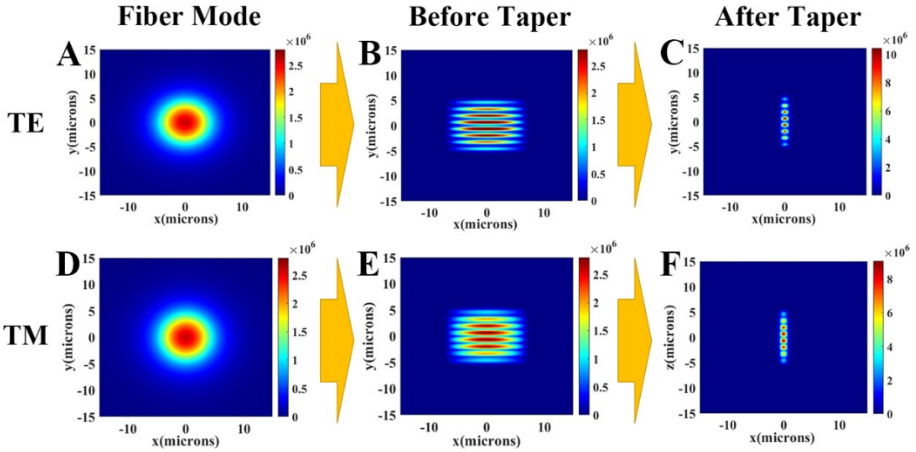

Figure 40: Mode matching at the input coupler. (A, D) Mode profile in the fiber for TE and TM polarization. (B, E) Mode profile before the taper for TE and TM polarization. (C, F) Mode profile after the taper for TE and TM polarization.

The width of the on-chip coupler (labeled as before taper in Figure 39B) and the taper length is then optimized at the wavelength of 1550nm with TE polarization. We purposely designed every layer to be in the same pattern so that the phase profile across the OPA can inherit the profile from the fiber. So that the coupler width for every layer is the same in this design. Figure 41A shows the sweeping results for the coupler width, the first coarse sweeping is done with a step of $0.5\mu m$, then a fine sweeping is followed with a step of $0.1\mu m$ at $13.5\mu m$ to $14.5\mu m$, the results shows that a coupler width (labeled as before taper in Figure 39B) of $13.9\mu m$ offers the best mode match, the

coupling efficiency from fiber to coupler is 74.23%. The coupling loss is contributed by two factors: firstly, Fresnel reflection happens on the interface between fiber and the device; and secondly, the layer thickness is selected to minimize the vertical crosstalk, this selection also makes that the mode profile is nearly zero at the center of every insulation SiO2 layer, which results in a certain mode mismatch.

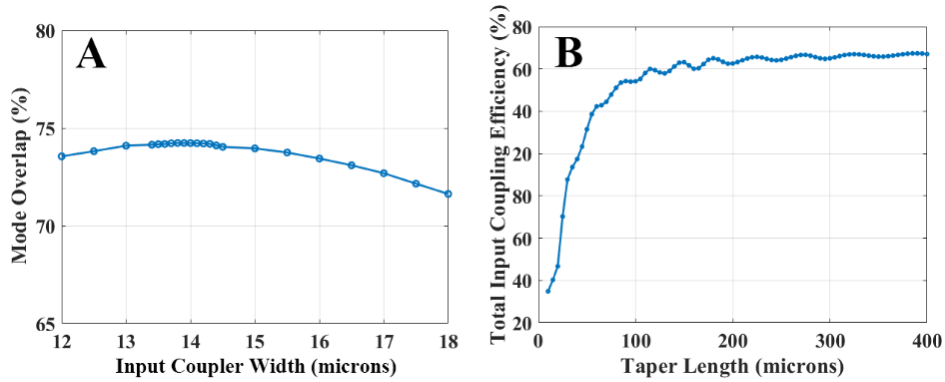

Figure 41: Optimization of the input coupler. (A) Coupler width (labeled as before taper in Figure 39B) sweeping for mode matching between SMF and input coupler. (B) Taper length sweeping for mode size conversion between input coupler and single mode waveguide.

Figure 41B shows the sweeping results of the taper length, note here the vertical axis in this figure is the total coupling efficiency of the edge coupler. The result curve gradually converges to 73.67% when the taper length approaches to 400μm, this corresponds to a 99.25% taper efficiency (73.67% / 74.23% = 99.25%). In this work, the taper length is selected to be 150μm, the corresponding coupling efficiency is 71.24%.

The mode propagation in the coupling region is plotted in Figure 42, 4A shows the side-view cross-section, thanks to the optimized layer thickness, the light propagation in all the eight layers is individual; 4B shows the top-view cross-section, the mode size conversion between the fiber and the single mode waveguide can be clearly observed. As stated above, the coupling efficiency

from an edge coupler is relatively stable in a broad bandwidth, the coupler is optimized at the wavelength of 1550nm, so that the coupling efficiency is tested over the wavelength region of 1500nm to 1600nm. Figure 42C shows the results, the highest efficiency is 71.70% at 1515nm, and the efficiency variation in the whole range is only 0.58%.

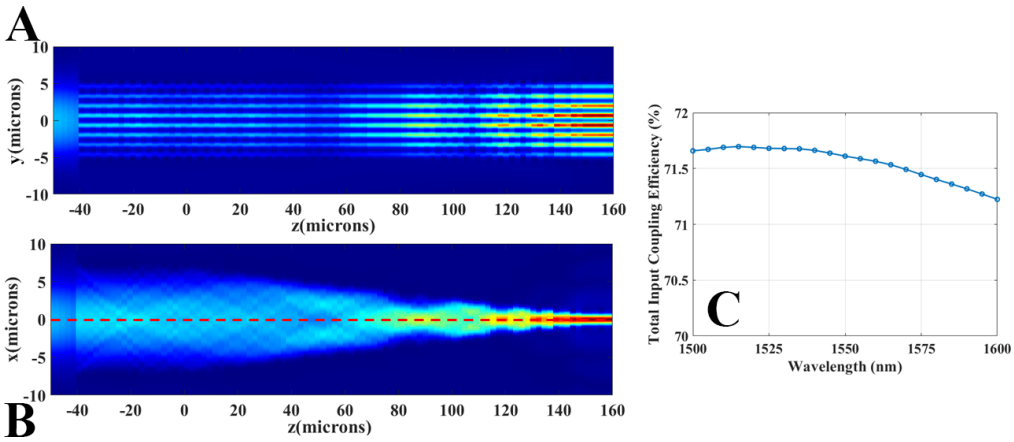

Figure 42: Performance of the whole input coupler. (A) Mode propagation in the whole input coupler from cross-section view at 1550nm. (B) Mode propagation in the whole input coupler from the top view. (C) The simulated coupling efficiency of the whole input coupler at the wavelength range of 1500nm to 1600nm.

5.4 Experimental Proof-of-Concept

The samples are fabricated in the Lurie Nanofabrication Facility (LNF) in Ann Arbor, Michigan, USA. Samples with 1 to 4 waveguide layers have been fabricated for the proof of concept. Note that due to the fabrication capability, we can only fabricate samples with up to 4 waveguide layers. Despite the limited fabrication capability, the experimental results are still effective in the comparison between single-layer and multi-layer configurations. In this part, we are going to present the experimental results, which show clearly that the 4-layer sample is better than the 1-layer sample in the coupling efficiency and beam convergence.

Figure 43 shows the fabricated 4-layer sample, the picture is taken by the dedicated

backscattering SEM imaging. From the picture, part of the Y-splitter tree and the Ω-shape delay line region can be distinguished. The picture is taken from an angle so that the end surface is presented, and the teeth-like shape at every pitch is a result of the PECVD cladding on a high aspect-ratio grating. The zoom-in picture shows 1 horizontal pitch, the four darker boxes are the emitting surface of the Si3N4 waveguides at different layers. Note that the picture is taken from an angle so that the Si3N4 waveguides become unclear from top to bottom.

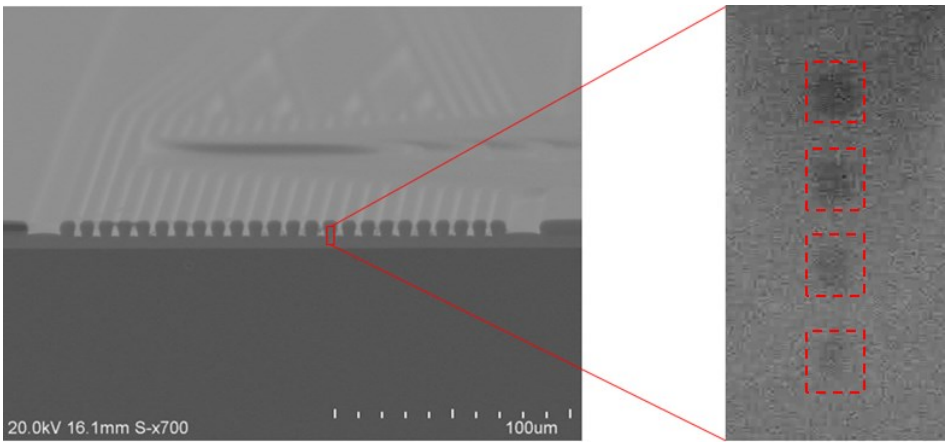

Figure 43: SEM picture for a 4-layer sample. Left: zoom-out picture of the device from an angle. Right: zoom-in picture of one pitch.

The input coupling efficiency is measured with the testing samples in the wavelength range of 1530nm to 1600nm (the wavelength range is C+L band, and the testing tool is Thorlabs TLX1 and TLX2). Figure 44 plotted the tested efficiency. Compared to the typical Gaussian-curve spectrum from a grating coupler, the tested curve for the 1-layer to 4-layer devices are relatively flat, this is due to the edge coupler which couples the light by direct mode match, but not the harmonic wave match (which is the case for the grating coupler). The input coupling efficiency for the 1-layer device is average -8.12 dB with a variance of 0.09 dB^2, and is improved to an

average of -4.57 dB with a variance of 0.13 dB2 for the 4-layer device. Note these tested values includes the taper efficiency. These results clearly show that the multi-waveguide-layer configuration can enhance the fiber-to-chip coupling efficiency. The fluctuation of the curves should be mainly due to the operation variations in the real experiment. Compared to the simulated results (average of -7.58 dB for 1-layer structure and -2.64 dB for 4-layer structure), the tested efficiency of the 1-layer sample is 0.54 dB lower than the simulated value, this is because of the extra-waveguide loss due to the waveguide layer roughness from the fabrication error. This issue is stronger in the 4-layer device, as the roughness of the layers will accumulate in the real sample, and thus results in a larger propagation loss in the 4-layer device. As a result, the tested input coupling efficiency of the 4-layer sample is 1.93 dB lower than the simulated value. It can be expected that this issue will be relieved with the state-of-the-art deposition method in an advanced foundry.

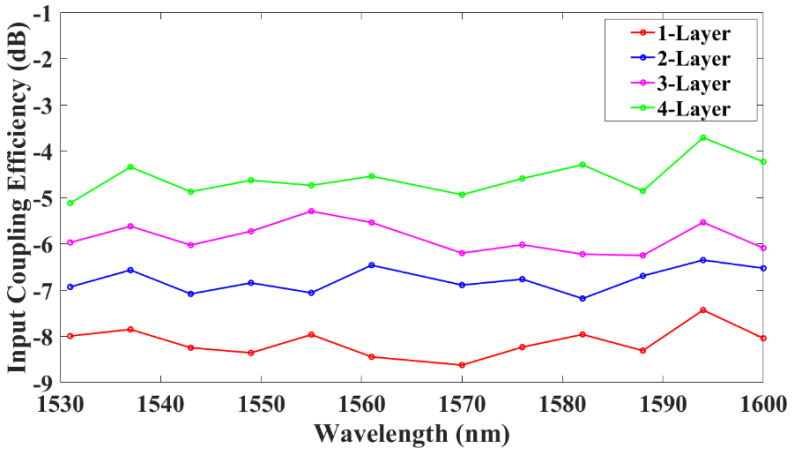

Figure 44: Testing results of the input coupling efficiency. Testing structure with straight waveguide and symmetric coupler is utilized to test the efficiency. The testing is done at the C+L wavelength band (1530nm to 1600nm) with laser sources TLX1 and TLX2 from Thorlabs.

The fiber-to-chip coupling and the emitting coupling are the two parts that contribute most of

the optical loss in a normal OPA device. As stated above, to achieve broadband high efficiency at both ends, we utilize edge couplers over the whole device. At the input end, the multi-waveguide-layer configuration can enhance the mode match between the fiber and the coupler. Each of the waveguide layers matches a part of the fiber mode so that the total mode match is good. The light propagates individually at each layer, then emits through the end-fire emitter and interferes with the light from other layers in the free space, and eventually forms one or a couple (depending on the aliasing effect) of beams. At the input end, the edge coupler relies on the multi-waveguide-layer configuration to achieve a good mode match. At the output end, the light is coupled from OPA to the free space, so there is no issue of mode mismatch, compared to the grating couplers which generate a considerable substrate leakage [50], using edge couplers will increase the emitting efficiency to approximately 70% (-1.55dB) [144], regardless of how many waveguide layers there are. Note this efficiency is obtained when the device has no antireflection coating, so the Fresnel reflection produces that 30% loss. Fresnel reflection can be suppressed by anti-reflection coating, in principle, a correct anti-reflection coating can increase the theoretical emitting efficiency to nearly 100%.

The issue at the emitting end is the beam convergence. As proved in the previous studies [9,24,37], an end-fire OPA with a single-waveguide-layer configuration necessarily means a fan-beam with only 1D convergence. In such a case, even though the OPA can have high optical efficiency, the energy of the beam will be distributed in a vertical line with about 35° FWHM (according to the simulation), which means that the optical efficiency at one particular angle is still

low. This issue is also addressed in this work by the multi-waveguide-layer configuration.

Figure 45 shows the tested farfield pattern at 1550nm wavelength, samples without the Ω-shape delay line region are used for this testing, as they always emit the main lobe to the normal direction. Figure 45A shows the farfield pattern for the 1-layer sample, and Figure 45B shows the pattern for the 4-layer sample. It can be observed that the beams in Figure 45B have obvious better vertical convergence than Figure 45A. This is clear evidence to show the multi-waveguide-layer configuration address the vertical convergence issue. In the 1-layer sample, the emitting aperture is approximately 600nm. On the other hand, in the 4-layer sample, the waveguide layers have the same pattern, which guarantees that there's no extra phase difference created between layers in the device, and the vertical phase profile that the OPA emits can inherit the same vertical phase profile from the fiber mode, with only slight variation caused by the fabrication errors; and in the main time, the emitting aperture has been increased to approximately $4.5\mu m$, which is 9 times than the 1-layer sample. Figure 45C and D show the vertical cross-section of the samples, the red curve in Figure 45C and blue curve in Figure 45D are the simulated results, and the yellow curve in Figure 45C and the green curve in Figure 45D are the tested results. A good fit can be observed between the simulated results and the experimental results, which validate the effectiveness of the design. The tested FWHM for the 1-layer sample is 37.64° (simulated result is 32.12°), and for the 4-layer sample is 17.42° (simulated result is 14.26°). Based on the simulation result, a full 8-layer device should be able to offer a vertical FWHM of approximately 5° [144]. It is also worth noting that the clear aliasing effect can be observed in Figure 45A and Figure 45B, those grating lobes appear at

approximately ±11.20°, which agrees with the horizontal pitch of 8μm that to be used in this work. In addition, it is possible to expect that a further aperiodic design can be applied to suppress the grating lobes.

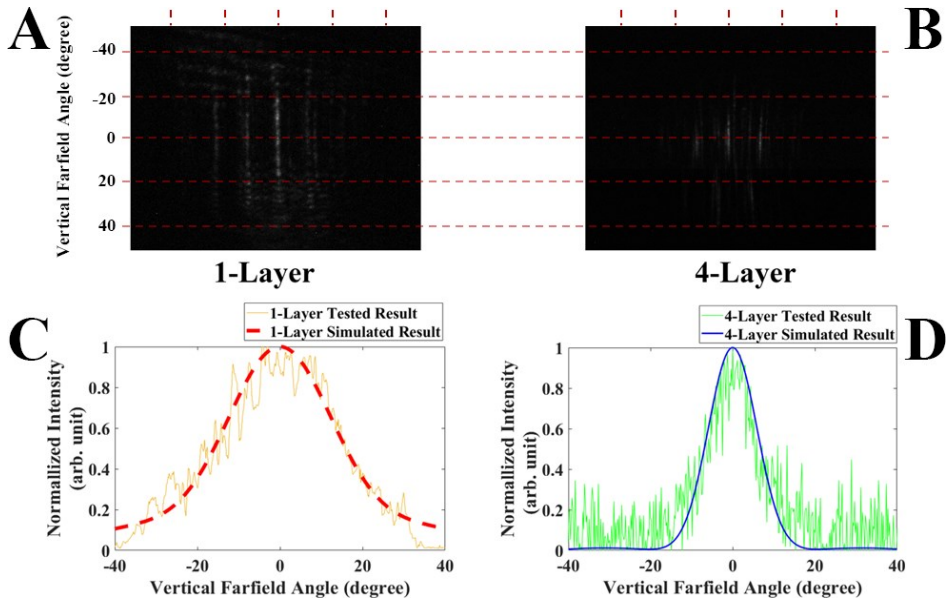

Figure 45: Tested farfield emitting pattern. (A) Farfield pattern for 1-layer structure. (B) Farfield pattern for 4-layer structure. (C) Vertical cross-section of the main lobe for 1-layer structure. Simulated FWHM: 32.12°, tested FWHM: 37.64°. (D) Vertical cross-section of the main lobe for 4-layer structure. Simulated FWHM: 14.26°, tested FWHM: 17.42°.

The beam shaping and steering in the horizontal direction are achieved by the Ω-shape delay line region. This design introduces an extra man-made dispersion effect into the device, which enables a highly sensitive beam steering capability. We have proven in our previous study [144] that the beam steering capability is linearly dependent on the length of the delay line, which can be summarized by the following equation.

$$\Delta\delta = \Delta\lambda * DL * b, \quad (5.1)$$

where Δδ is the beam steering angle, Δλ is the wavelength change, DL is the length of the delay

line, and b is the basic steering sensitivity, which depends on the waveguide dimension.

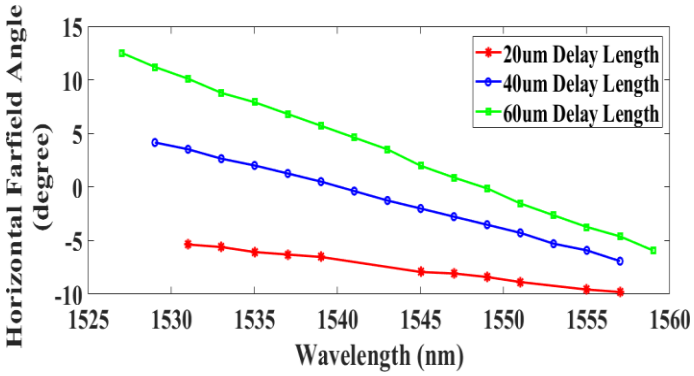

Figure 46: Beam steering capability of the 4-layer structure.

Samples with the delay length of 20μm, 40μm, and 60μm have been tested to validate the beam steering mechanism. Figure 46 plots the tested beam steering capability from the 4-layer devices. The angle shown in the figure is the farfield angle of the main lobe. The red, blue, and green lines are for the samples with the delay length of 20μm, 40μm, and 60μm, respectively. The data show that the 20μm sample can steer the beam from -5.37° at 1531nm to -9.80° at 1557nm, corresponds to -0.170°/nm; the 40μm sample steers the beam from 4.15° at 1529nm to -6.92° at 1557nm, corresponds to -0.395°/nm; the 60μm sample steers the beam from 12.52° at 1527nm to -5.93° at 1559nm, corresponds to -0.577°/nm. It can be concluded that the beam can be steered linearly by wavelength tuning, and the beam steering capability is proportional to the delay length, which agrees with the equation $\Delta\delta = \Delta\lambda * DL * b$. Based on this mechanism, the beam steering capability can be manipulated to any design value from 0° to 180° per nm wavelength. In the case of using a laser source with a high tuning step, a lower steering capability can be selected to increase a scanning resolution; and in the case of a laser source with a narrower wavelength range, a higher steering capability can be selected to increase the field of view (FOV).

5.5 Conclusion

In this work, we have proposed and demonstrated a true 3-D OPA device with a broadband high efficiency. This example presents the possibility of the multi-waveguide-layer configuration in a PIC. The existence of multiple waveguide layers perfectly addresses the two disadvantages of using the edge couplers in a traditional SOI-based OPA device. Thanks to the more waveguide layers, the mode match between the fiber and the on-chip waveguide is enhanced, and the emitting beams are also converged in the vertical direction. With the proof-of-concept experimental results, we found clear evidence to show the advantages of the multi-waveguide-layer configuration. In addition, the beam steering capability, which is enabled by the Ω-shape delay line region, is validated experimentally. In summary, the proposed 3-D OPA device offers high fiber-to-chip-to-beam efficiency, with the beam to be 2-D converged, and with the beam steering capability to be highly sensitive (manipulatable from 0° to 180° per nm wavelength) and simply operated (only one degree of freedom in operation). This design opens a new possibility for OPA devices.

The proposed idea in Figure 39 has been studied and experimentally proved. However, it hasn't presented the best potential of a multi-waveguide-layer PIC. Still taking the OPA device as an example, Figure 47 illustrates an ideal multi-layer OPA. In this device, individual phase shifters will be applied to every single waveguide, in such a case, the emitting beam will be 2-D steerable. In addition, since the phase in every waveguide can be controlled, the input fiber is no longer required to be single mode, multimode fibers have a much larger core diameter (for example, GIF625 from Thorlabs has a core diameter of 62.5μm), they can easily power nearly 50 layers of

the waveguide (in the case of a 1.3μm distance between layers).

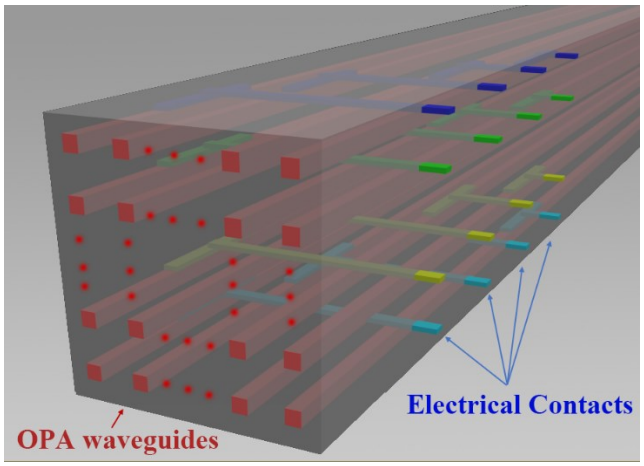

Figure 47: Illustration of an ideal multi-layer OPA. Waveguides are shown in red; one individual phase shifter is applied for every single waveguide. The electrical contacts are colorized for different layers, they can be designed to be at the side wall or the top of the structure.

The fabrication strategy of such a device can also be CMOS-compatible, despite it being far beyond our current fabrication capability. However, if one day such a multi-layer PIC can be easily available to researchers, a brand-new possibility will be added to the current PIC industry.

Chapter 6 The Fabrication of the Self-Aligned Multi-Layer 3-D OPA

6.1 Introduction

Thanks to the unique advantages of photons over electrons, photonic integrated circuits (PICs) have been proposed and studied for decades as the next-generation chip. They have been proven to have various applications in multiple material platforms [178-179]. Most PICs so far inherit the mature CMOS (complementary metal oxide semiconductor) fabrication process from the electronic IC (integrated circuit) industry. In the standard procedure, the basic components (transistors in EICs - electronic integrated circuits, waveguides in PICs) are firstly fabricated on the top surface of a wafer, and then the metal contacts are fabricated above the top surface; thus, the basic components are typically in a single layer. These single-layer fabrication techniques are very mature, but it also limits the performance of the IC in the meantime. In recent years, the EIC industry has developed a trend of converting the memory and computing unit designs from 2-D to 3-D [179,180]. In principle, this idea and the fabrication techniques can also be applied to the 3-D multi-waveguide-layer PICs [165,181，182].

Optical phased array (OPA) is a relatively new type of PIC; it is proposed as a potential solution in the Lidar application for autonomous driving technology. It has drawn considerable research efforts due to its promising capability of solid-state beam steering since 2009 [12]. As a result, tremendous progress has been made [2]. As one type of PICs, most published OPA devices

are based on the single-waveguide-layer configuration [2], which limits the total optical efficiency on both the fiber-to-chip and the chip-to-beam coupling. Works have been done to address this issue. In [141], a direct writing method based on ultrafast laser inscription (ULI) is applied to convert the single-layer waveguides to 3-D waveguides in an OPA device. It forms an edge-coupled 2-D emitting array on the side of the device and thus achieves a high chip-to-beam coupling efficiency. In [143], the idea of a true 3-D OPA with multiple waveguide layers all over the device has been proposed, and the potential fabrication process is discussed.

We have taken one step further by proposing and experimentally demonstrating a true 3-D OPA device [144,145]; a sample with 4X16 OPA on the edge has been fabricated and tested. By applying the multi-waveguide layer configuration, we can utilize the edge coupler for both the fiber-to-chip and the chip-to-beam coupling, which offers the capability of emitting a 2-D converged beam with a broadband high optical efficiency. During this work, we have developed a self-aligned process to address some of the fabrication challenges and significantly reduce the number of process steps. In this paper, we present the development of this process in detail.

6.2 Fabrication Challenges in the Multi-Waveguide-Layer Configuration

Figure 48 illustrates the standard method of fabricating a multi-waveguide-layer device. Figure 48a shows that, in this process, a whole layering-patterning-cladding-polishing cycle is needed for every layer of the waveguides. It is consistent with the back-end process in the electronic IC industry, which fabricates the interconnection metal layers. In the EICs, it is not necessary to have perfect control over the layer spacing and the alignment between layers; however,

in the PICs, especially in the OPA devices, these two issues can mess up the phase profile at the emitting surface and results in a distorted farfield pattern. Figure 48b illustrates an example of the potential fabrication errors, the inadequate control of layer spacing, and the misalignment between layers. In the OPA application, a good emitting farfield pattern relies on the proper arrangement of the array. In a Si 3-D OPA, the waveguide core size is typically around 300 to 500 nm; in such a case, a 10% fabrication error will be about 30 to 50 nm, which may not be acceptable. In a Si3N4 3-D OPA, the fabrication tolerance is slightly relieved but still in the range of around 100nm (~10% feature size). In the current CMOS compatible fabrication process, such a low fabrication tolerance is challenging in either the layer spacing control (relying on the thickness control during a chemical mechanical polishing CMP process) or the alignment between layers (relying on the calibration between multiple exposures) [183,184].

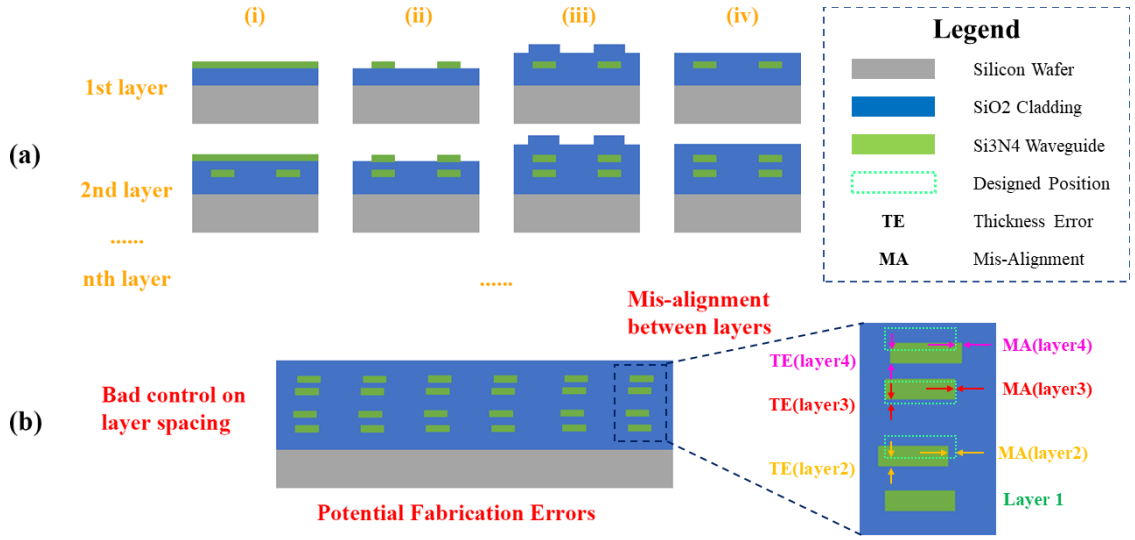

Figure 48: Normal method of fabricating a multi-layer structure. (a) Process flow. i, waveguide layer deposition; ii, patterning; iii, cladding layer deposition; iv, chemical mechanical polishing (CMP). (b) Two potential fabrication errors that can significantly affect the device performance are (1) the bad control of layer spacing, and (2) the misalignment between layers.

A possible method to address these two issues is using a single-lithography process over multiple waveguide layers. Figure 49 illustrates this process; instead of patterning one waveguide layer at a time, this process directly patterns all the waveguide layers together. Apparently, this process requires every waveguide layer to contain the same pattern (or at least a portion of the whole pattern to be the same); fortunately, this is possible in an OPA device [144,145]. In this process, the layer spacing is controlled by CVD (chemical vaper deposition) deposition, which has excellent control over the thickness (the accuracy can be smaller than 10 nm). Hence, the waveguide layers are self-aligned due to the single-lithography process.

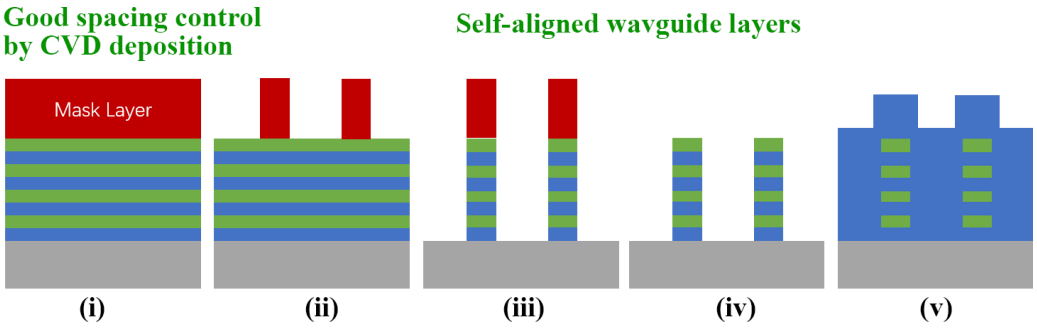

Figure 49: Fabrication process flow with single lithography step. i, layer depositions; ii, mask layer pattering; iii, dry etching over multiple waveguide layers; iv, mask layer removal; v, cladding layer deposition. The layer spacing can be well controlled by CVD deposition, and the waveguide layers are self-aligned.

In summary, a single-lithography process will be a better option for a 3-D PIC which has two characteristics: firstly, it allows every layer to have the whole or a part of the pattern to be the same; and secondly, it is very sensitive to the arrangement of the waveguides between layers. In addition, logically, for the applications which have the first characteristic, most of them should tend to have the second one. On the other hand, for those applications which have the second characteristic, it should be minor, but a still considerable portion of them also have the first one; that is to say, these

two characteristics should have a particular interdepend symbiotic property.

6.3 Fabrication of a 3-D OPA Device

Figure 50 illustrates the design of the 3-D OPA device. Figure 50a is the illustration of the device. We have detailly analyzed the performance of this device in our previous work [144,145]. In summary, thanks to the multi-waveguide-layer configuration, this device can utilize the edge coupling to achieve both the fiber-to-chip and the chip-to-beam coupling, guaranteeing a broadband high optical efficiency. The multi-waveguide-layer design offers two advantages to the device: firstly, at the input coupling end, it enhances the mode-match between the fiber and the on-chip coupler; secondly, at the emitting coupling end, it enhances the vertical convergence to the emitting beam. The beam steering capability is enabled by the Ω-shape design, which purposely generates an extra dispersive effect for the device, so the beam can be steered horizontally by tuning the wavelength of the input light. Utilizing the Ω-shape design allows the device to be simply used by one degree-of-freedom operation. It also frees the device from having individual phase shifters on every waveguide, which is extremely difficult to fabricate in the multi-waveguide-layer configuration.

Figure 50b and c give an example of the effect of the fabrication error presented in Figure 48; they show the simulated farfield emitting pattern of the device with and without fabrication error. In the simulation, all the other parameters are set to be the same. The misalignment and thickness error are set to 0 in Figure 50b; while in Figure 50c, the misalignment is set to 100nm for the 2nd layer, -100nm for the 3rd layer, and 50nm for the 4th layer, and the thickness error are set to 100nm

for the 2nd layer, 50nm for the 3rd layer, and -100nm for the 4th layer. In Figure 50b, the farfield is clear, and several grating lobes can be observed due to the aliasing effect, (which happens when the emitting pitch is larger than half of the emitting wavelength). As a comparison, the farfield in Figure 50c is messed up, and there are a lot of noise-level emitting lobes appearing in the field; this is because the fabrication error messed up the phase profile at the emitting surface.

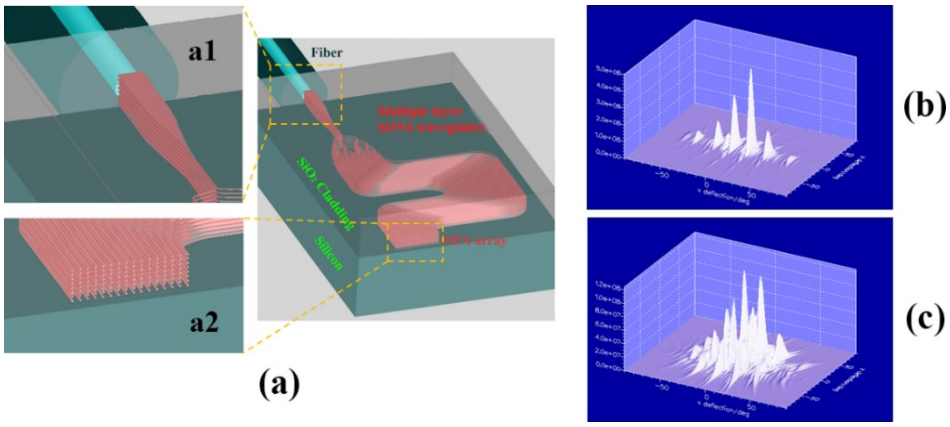

Figure 50: Design of the multi-layer Si3N4 3D OPA. (a) Schematic (3D view) of the structure. (b) Simulation result of the designed structure with no fabrication imperfection, a clear farfield is generated, aliading effect can be observed. (c) Simulation result of the designed structure with fabrication error, a messed farfield is generated because of the phase error.

Our sample is fabricated at the Lurie Nanofabrication Facility (LNF) in Ann Arbor, Michigan, USA. The one-lithography process is developed based on the fabrication capability of LNF. In the following, the development of the process is presented in detail.

6.3.1 Photoresist Recipe

In the one-lithography process, a strict vertical etching is required to maintain the same pattern over all the layers, so wet etching is not applicable. However, when using an RIE (reactive ion etching) dry etching, any mask layer will also be depleted during the etching. Therefore, the

number of waveguide layers that can be etched in one lithography depends on the thickness of the mask layer, which essentially depends on the thickness of the photoresist. The thickness of the PR layer is limited by the feature size of the device or the waveguide width, in our case. Here, width is related to the single-mode condition. As a result of its lower refractive index, Si3N4 is selected as the waveguide material in this device due to its better performance in passive devices than Si [178]. SiO2 is chosen as the cladding material. According to the simulation results, 1100 nm is the maximum width that allows the Si3N4 waveguide to maintain the single mode. So, the first thing we do is to determine the thickest PR that can constantly offer 1100nm resolution.

The photoresist we used is a standard positive photoresist SPR220 [185]. ACS 200 cluster tool is used for the coating, baking, and developing of the PR, and GCA AutoStepper is used for exposure. The spin rate in the coating step is tuned to achieve different PR thicknesses, and the exposure matrix method is utilized to determine the best exposure time and offset. In this method, multiple dies are exposed on the same wafer with a step-increased exposure time or offset; then, by comparing the color of every die after PR developing, the best exposure time and offset can be found. According to the experiment result, we have found that the thickest PR offering 1100 nm resolution is approximately 4um. Figure 51 shows examples of the developing results. Figure 51a is the end of the input taper and the 1st Y-splitter of the device at 4um PR. The picture is focused when a clear boundary of the larger triangles is observed. At this focus, the narrow waveguides are also in focus, indicating that the small and large features are at the same thickness after PR development. Figure 51b shows the same part at the 5um PR setting. The larger triangular parts

can be developed well, but the narrow waveguide lines are not in focus; this means that when the large features are sufficiently developed, the small features are already over-developed. We conclude this is an indication of a too-thick PR. Therefore, we have determined that the thickest PR configuration for the 1.1um feature size is approximately 4um.

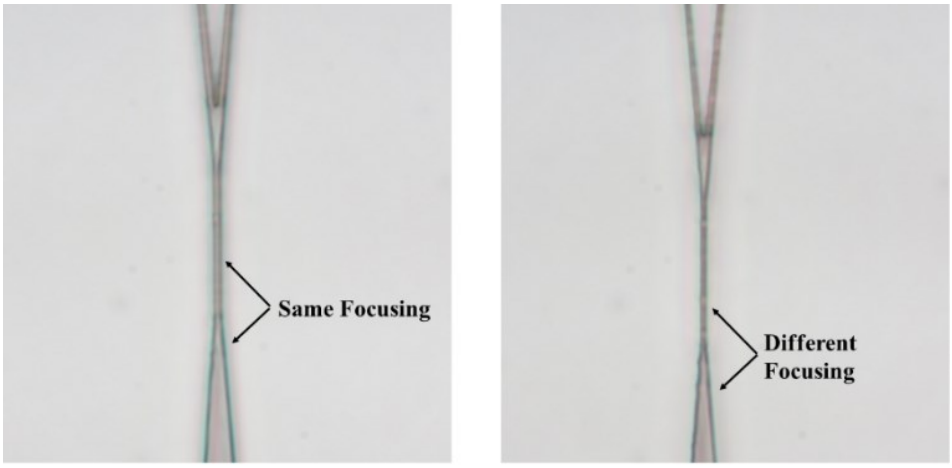

Figure 51: Illustration of the limited PR thickness. (a) Y-splitter on 4um PR. (b) Y-splitter on 5um PR.

6.3.2 RIE Etching Profile

The etching is the most critical step in the one-lithography process. In this work, we have tested 3 different etching methods, which are: A. using only PR as the mask, with etchant composition to achieve the best directionality; B. Using only PR as the mask, with etchant composition to achieve the best selectivity; C. Using a-Si as the hard mask, this method requires a two-step etching, the a-Si is firstly etched by PR, then the Si3N4/SiO2 stack is etched by a-Si. In the experiment, the tool we used is the STS Glass Etcher at LNF, the gas mixture consists of a large amount of helium of 174 sccm and a small portion of etchant gas of a maximum of 40 sccm. A mixture of CF4, C4F8, and H2 is used as the etchant to achieve different selectivity and

directionality; HBr is used to etch the a-Si (in a different tool). Table 2 summarizes the etching rate in the 3 different etching methods, and the data are tested on blank wafers.

In the fluorocarbon-based etch processes, the reaction depends on: 1) a combination of surface passivation of the fluorocarbon; 2) ion bombardment that breaks the bonds in the etched material so they can combine with the fluorocarbon, creating a volatile byproduct. The etching process is highly dependent on the respective rates of these two factors. In short, the higher the carbon content in the gas mixture used, the faster the passivation rate. This will slow the etching process since more energy is required to break through the passivation layer. This effect is stronger on the photoresist than on SiO2 and Si3N4; thus, it leads to a higher selectivity. On the other hand, this effect also leads to a more tapered etching profile. Since ion bombardment tends to be weaker at the edge of features, some of the ions will be shadowed by the passivation layer, and their trajectories will not be perfectly perpendicular to the wafer surface. Moreover, adding H2 could reduce free fluorine content in plasma, creating a similar effect to higher carbon content.

From the data in Table 2, with the knowledge of the maximum thickness of PR to be 4um, we can easily calculate the number of waveguide layers that can be etched in one lithography. Method A has the highest fluorine content, which leads to the best directionality; yet, on the other hand, the selectivity is lower, so the maximum number of layers that can be etched in one lithography is 4 layers. Method B has the highest carbon content (H2 further reduces the fluorine content), so it has the best selectivity; it is possible to etch 14 layers of waveguides at one time. Method C uses a hard mask, which results in an even larger overall selectivity, so etching 50 layers are possible

in one lithography.

Methods			Etchant	Flow rate (sccm)	Etching rate (A/s)			
					Si_3N_4	SiO_2	PR	a-Si
A	Best Directionality		CF_4	40	55.7	53.1	41.7	-
B	Best Selectivity		C_4F_8	10	45.1	32.0	8.3	-
			H_2	30				
C	Using a-Si Hard Mask	1st etching	HBr	100	-	-	4.6	20.0
		2nd etching	CF_4	20	20.6	55.7	-	8.4
			C_4F_8	20				

Table 2: Summary of the etching rate in the 3 cases. Case 1, to have the best directionality when using PR as the mask. Case 2, to have the best selectivity when using PR as the mask. Case 3, using a-Si as the hard mask.

These estimations are calculated based on the etching rate from the blank wafer. In the practical case, we also need to check the etching profile since we expect the same pattern at every layer. We tested the etching profile from methods A, B, and C with all the other parameters (pressure, RF power, and temperature) set to be identical. Figure 52 shows the results of the etching profile check. Figure 52a and b are the profile for Method A and B, respectively; the test is done on the substrate with 3-SiN-layer Si3N4/SiO2 stacks. It can be seen that the etching profile in Figure 52a from Method A is very vertical. This is due to the chamber configuration and gas mixture of the STS Glass Etcher. Because of the relatively small portion of the etchant in the gas mixture, the etching process is highly ‘diluted’, inhibiting excessive passivation. The tool also runs under very low pressure, which helps with the etching profile.

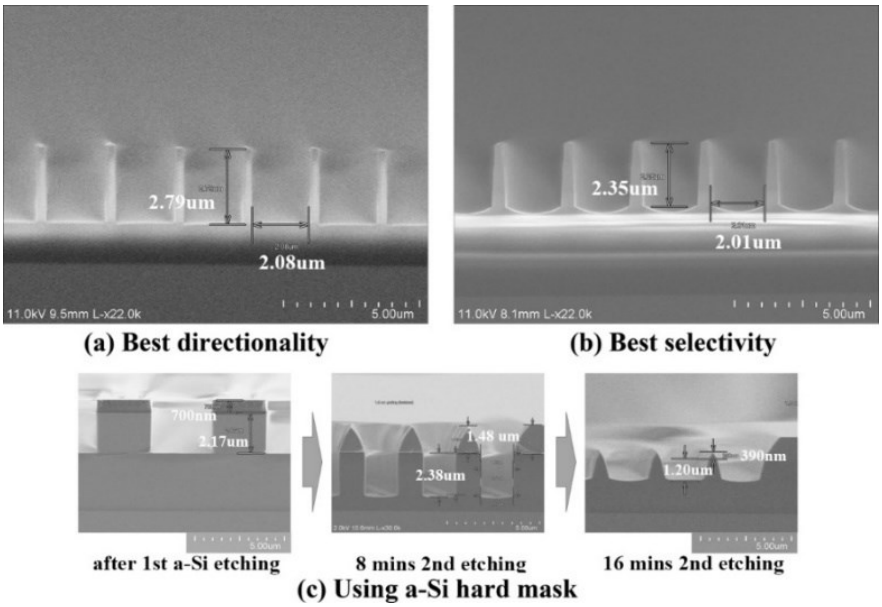

Figure 52: Etching profile of the 3 cases. (a) Best directionality; (b) Best selectivity, a clear taper can be found on the gratings; (c) Using a-Si hard mask, faceting effect happens in the 2nd etching step, resulting in degraded gratings.

Figure 52b shows the etching profile of Method B (best selectivity with PR); it is evident that the gratings are tapered. This phenomenon is caused by the relatively fast growth of the passivation layer, as explained above. Although the taper is already obvious in the 3-SiN-layer substrate, it can be estimated that the tapering effect will be significantly stronger in a 14-SiN-layer substrate, and the top layers will not be able to maintain the dimensions, which is not acceptable in the 3-D OPA devices.

Figure 52c is the tested etching results of Method C; the test is done on a substrate with 3um SiO2, 2um a-Si, and 0.97um PR. Figure 52c left is the etching profile after the 1st step of a-Si etching; it can be seen that the etching of a-Si is relatively vertical, and the etching stopped on the surface of SiO2 perfectly. This is due to the significant selectivity difference between Si and SiO2, and about 270nm PR is consumed. Figure 52c middle is taken 8 mins after the 2nd etching; at this

time, the etching on the SiO2 is vertical, but the a-Si hard mask has already started to degrade because of the faceting effect. This effect usually happens in the etching, which is dominated by physical sputtering but not a chemical reaction; in such a process, there is a strong sputter yield dependence on the incidence angle of the incoming ions. In the 2nd step of Method C, a-Si's etching rate is low, indicating that this etching is dominated by physical sputtering. At the corner of a feature, which is typically slightly (maybe not even visibly) rounded, a specific angle will be developed where the sputter yield is highest, resulting in a degradation of the features. This degradation hadn't merged into SiO2 layers in 5c middle, so the SiO2 features are still vertical; but in Figure 52c right, the profile is taken after 16 mins of the 2nd etching, and the degradation had merged into SiO2. In the OPA sample, Method C eventually results in only a few layers of Si3N4 waveguide being maintained after a long etching, so this method is also not acceptable in a 3-D OPA device.

In summary, we found that only Method A is acceptable for the 3-D OPA device.

6.3.3 RIE Etching Rate at Small Openings

The etching rate in Table 2 is tested on blank wafers. However, in the small openings, the etching rate is usually slower because etchant ions are hard to enter. When using Method A, we have calculated that 4 layers of Si3N4 waveguides are possible to be etched in one lithography. To achieve a full etching on the 4 layers, we need to avoid the small openings. Figure 53 shows the etching profile at small openings, the pictures are taken from a testing wafer containing isolated gratings with different openings, and the grating width is 500nm. A relatively shallow etching is

proceeded in the testing to observe the etching differences in small openings. From Figure 53, the etching depth at large openings is approximately 1.2um over the whole wafer, while the etching depth is obviously shallower at small openings; it is etched approximately 290nm at 1um openings, 1030nm at 2.5um openings, and 1040nm at 4um openings. Eventually, when the opening size reaches 5.5um, the etching depth at the center of the openings becomes roughly as same as the depth at large openings.

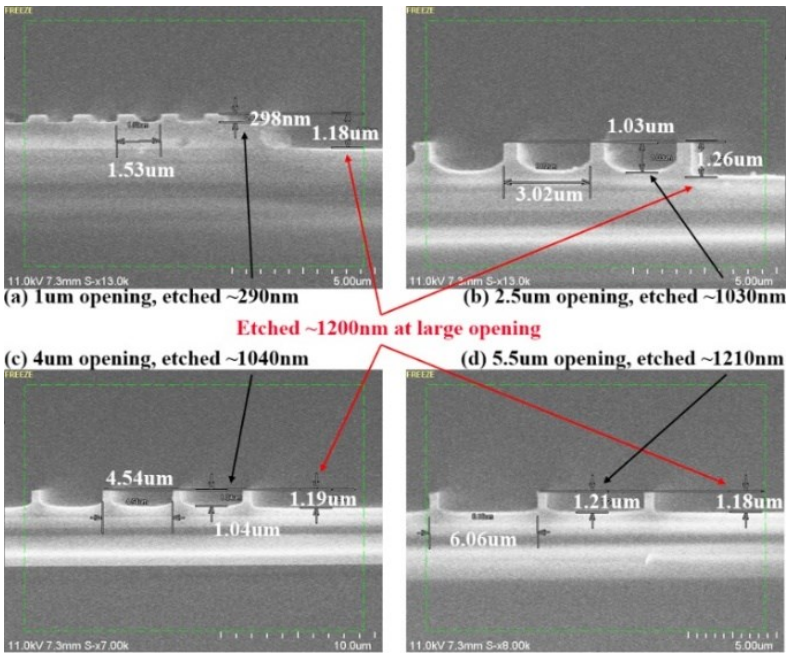

Figure 53: Illustration of slower etching in small openings. The etching depth at the large openings is approximately 1.2um, while at small openings are: (a) 290nm at 1um openings; (b) 1030nm at 2.5um openings; (c) 1040nm at 4um openings; (d) 1200nm at 5.5um openings.

6.4 Fabrication Result

In summary, we used 4um PR as the mask layer, Method A for etching, and 6.9 um as the smallest openings in the device. During the etching, time control is utilized to ensure it is sufficient to etch through the four Si3N4 layers. Figure 54a shows the image of the emitting end of a

completed 4-layer sample; the dedicated backscattering SEM (scattering electronic microscope) imaging takes the picture. The image is taken from an angle so that the end surface is presented, and the tooth-like shape at every pitch is the result of the PECVD (plasmonic enhanced chemical vapor deposition) cladding on a high aspect-ratio grating. Figure 54b is a zoom-in picture showing three horizontal pitches; the four brighter boxes are the emitting surface of the Si3N4 waveguides at different layers. A slight inverse taper (the top of the grating is wider than the bottom of the grating) can be observed in the figure; the reason for this should be that during the RIE process, the charge will accumulate on the etching surface, which enhances the horizontal etching right close to the etching surface. Therefore, as the etching becomes deeper, the grating shows a slight inverse taper. In addition, the image is taken from an angle, which also visually enhances the extent of the inverse taper.

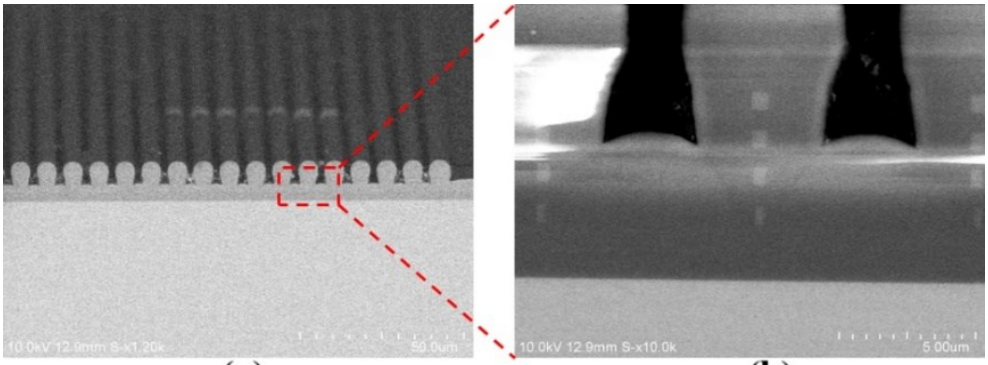

Figure 54: SEM picture for a 4-layer sample. (a): zoom-out view of the device from an angle. The Y-splitter tree and the delay line region can be distinguished from the picture. (b): zoom-in view of three pitches, four Si3N4 end-fire emitters in every pitch can be distinguished.

The optical performance of the fabricated device is tested using a commercial tunable laser and the Fourier optics measurement. The results show that the 3-D OPA device can emit a beam

with vertical convergence of 17.42° [145], which indicates that the spacing and calibration between layers are fabricated as designed.

6.5 Conclusion

In this work, we demonstrated a single lithography fabrication process to address the layer spacing and calibration issues in the normal multi-layer process. In this process, the layer spacing is controlled by CVD deposition, so the accuracy of the spacing thickness can be much better than the control in a CMP process; layer calibration is achieved by self-alignment. In addition, an etching method with a very vertical etching profile is selected. Therefore, it ensures that the pattern at every waveguide layer is sufficiently similar. It is also worth mentioning that our process is developed at the LNF; if one wants to develop such a process somewhere else, the detailed process parameters and the etching possibility may differ. However, the basic idea of this process is valid in any place, that is, controlling the layer spacing by CVD deposition (which is more accurate than the control in a CMP process) and calibrating multiple layers by self-alignment. This method is more suitable than the normal method for a multi-waveguide-layer PIC if it: 1) requires the same pattern on every waveguide layer; and 2) is sensitive to the fabrication errors in layer spacing and calibration.

Chapter 7 Conclusion

This dissertation introduced the research projects on the integrated optical phased array (OPA) devices completed by the author. The conclusion for each project is summarized at the end of each chapter. As the overall conclusion, here's a summary of the entire dissertation. Chapter I of this dissertation offers a detailed review to the OPA research. Chapter II proposes and numerically demonstrates the compound period grating coupler to enhance the beam steering capability of wavelength-tuned waveguide grating couplers. Chapter III proposes the phase combining unit (PCU) to allow using N phase shifters to control 2N-1 emitters. Chapter IV-VI are all for the 3-D OPA project, Chapter IV proposes the idea of 3-D OPA, which uses multi-layer end-fire array for the OPA. A detailed numerical investigation is presented. Chapter V upgrades this idea into a whole 3-D OPA device by proposing the design of input coupler. Experimental proof-of-concept is made, and the testing results suggest that the multi-waveguide-layer configuration enhances the input coupling and the vertical convergence of the emitting beam. Chapter VI introduces the fabrication process for the demonstrated 3-D OPA, where a single-lithography process is applied to achieve good control on layer thickness and gap, and the calibration between layers.

References

[1] Heck, M.J.R. Highly integrated optical phased arrays: photonic integrated circuits for optical beam shaping and beam steering. *NanoPhotonics* 2017, 6, 93-107.

[2] Sun, X.; Zhang, L.; Zhang, Q.; Zhang, W. Si Photonics for Practical LiDAR Solutions. *Appl. Sci.* 2019, 9, 4225.

[3] Hashemi, H. A Review of Semiconductor-Based Monolithic Optical Phased Array Architectures. *IEEE Jour. Sol. Stat. Cir.* 2021, 1, 222-234.

[4] Guo, Y.; Guo, Y.; Li, C.; Zhang, H.; Zhou, X.; Zhang, L. Integrated Optical Phased Arrays for Beam Forming and Steering. *Appl. Sci.* 2021, 11, 4017.

[5] Kim, I.; Martins, R.J.; Jang, J.; Badloe, T.; Khadir, S.; Jung, H; Kim, H.; Kim, J.; Genevet, P.; Rho, J. Nanophotonics for Light Detection and Ranging Technology. *Nat. Nanotech.* 2021, 16, 508-524.

[6] Hsu, C.Y.; Yiu, G.Z.; Chang, Y.C. Free-Space Applications of Silicon Photonics: A Review. *Micromachines* 2022, 13, 990.

[7] Wight, D.R.; Heaton, J.M.; Hughes, B.T.; Birbeck, J.C.H.; Hilton, K.P.; Taylor, D.J. Novel Phased Array Optical Scanning Device Implemented Using GaAs / AlGaAs Technology. *Appl. Phys. Lett.* 1991, 59, 899

[8] Qin, C.; Shang, K.; Feng, S.; Liu, G.; Liu, G.; Pathak, S.; Yoo, S.J.B. 1X256 Multi-layer, Low-loss, Si3N4 Waveguide Optical Phased Arrays with 0.050 Instantaneous-Field-of-View. *CLEO* 2017, STh1M.2.

[9] Kossey, M.R.; Rizk, C.; Foster, A.C. End-fire Silicon Optical Phased Array with Half-Wavelength Spacing. *APL Photon.* 2018, 3, 011301.

[10] Bhandari, B.; Wang, C.; Gwon, J.Y.; Heo, J.M.; Ko, S.Y.; Oh, M.C.; Lee, S.S. Dispersive Silicon-nitride Optical Phased Array Incorporating Arrayed Waveguide Delay Lines for Passive Line Beam Scanning. *Sci. Rep.* 2022, 12, 18759

[11] Vasey, F.; Reinhart, F.K.; Houdre, R.; Stauffer, J.M. Spatial Optical Beam Steering with an AlGaAs Integrated Phased Array. *Appl. Opt.* 1993, 32, 3220-3232.

[12] Acoleyen, K.V.; Bogaerts, W.; Jagerska, J.; Thomas, N.L.; Houdre, R.; Baets, R. Off-chip Beam Steering with a One-Dimensional Optical Phased Array on Silicon-on-insulator. *Opt. Lett.* 2009, 34, 1477-1479.

[13] Acoleyen, K.V.; Komorowska, K.; Bogaerts, W.; Baets, R. One-dimensional Off-chip Beam Steering and Shaping Using Optical Phased Arrays on Silicon-on-insulator. *J. Light. Tech.* 2011, 29, 3500-3505.

[14] Doylend, J.K.; Heck, M.J.R.; Bovington, J.T.; Peters, J.D.; Coldren, L.A.; Bowers, J.E. Two-dimensional Free-Space Beam Steering with an Optical Phased Array on Silicon-on-insulator. *Opt. Exp.* 2011, 19, 21595-21604.

[15] Kwong, D.; Hosseini, A.; Covey, J.; Zhang, Y.; Xu, X.; Subbaraman, H.; Chen, R.T. On-chip Silicon Optical Phased Array for Two-dimensional Beam Steering. *Opt. Lett.* 2014, 39, 941-944.

[16] Sun, J.; Timurdogan, E.; Yaacobi, A.; Hosseini, E.S.; Watts, M.R. Large-scale Nanophotonic Phased Array. *Nat.* 2013, 493, 195-199.

[17] Sun, J.; Timurdogan, E.; Yaacobi, A.; Su, Z.; Hosseini, E.S.; Cole, D.B.; Watts, M.R. Large-Scale Silicon Photonic Circuits for Optical Phased Arrays. *IEEE J. Sel. Top. Quan. Elec.* 2014, 20, 8201115.

[18] Zhang, H.; Zhang, Z.; Lv, J; Peng, C.; Hu, W. Fast Beam Steering Enabled by a Chip-Scale Optical Phased Array with 8X8 Elements. *Opt. Commun.* 2020, 461, 125267.

[19] Xu, W.; Zhou, L.; Lu, L.; Chen, J. Aliasing-free Optical Phased Array Beam-Steering with a Plateau Envelope. *Opt. Exp.* 2019, 27, 3354-3368.

[20] Komlhenovic, T.; Helkey, R.; Coldren, L; Bowers, J.E. Sparse Aperiodic Arrays for Optical Beam Forming and LIDAR. *Opt. Exp.* 2017, 25, 2511-2528.

[21] Zhuang, D.; Zhang, L.; Han, X.; Li, Y.; Li, Y.; Liu, X.; Gao, F.; Song, J. Omnidirectional Beam Steering Using Aperiodic Optical Phased Array with High Error Margin. *Opt. Exp.* 2018, 26, 19154-19170.

[22] Yang, B.; Chen, H.; Yang, S.; Chen, M. An Improved Aperiodic OPA Design based on Large Antenna Spacing. *Opt. Commun.* 2020, 475, 125852.

[23] Du, K.; Wang, R.; Guo, J.; Jiang, R.; Kan, D.; Zhang, Y. Design of a Sparse Array for a One-Dimensional Non-Uniform Optical Phased Array. *J. Opt. Soc. Am. B.* 2022, 39, 1141-1146.

[24] Kwong, D.; Hosseini, A.; Zhang, Y.; Chen, R.T. 1X12 Unequally Spaced Waveguide Array

for Actively Tuned Optical Phased Array on a Silicon Nanomembrane. *Appl. Phys. Lett.* 2011, 99, 051104.

[25] Shin, M.C.; Mohanty, A.; Watson, K.; Bhatt, G.R.; Phare, C.T.; Miller, S.A.; Zadka, M.; Lee, B.S.; Ji, X.; Datta, I.; etc. Chip-Scale Blue Light Phased Array. *Opt. Lett.* 2020, 45, 1934-1937.

[26] Hutchison, D.N.; Sun, J.; Doylend, J.K.; Kumar, R.; Heck, J.; Kim, W.; Phare, C.T.; Feshali, A.; Rong, H. High-Resolution Aliasing-Free Optical Beam Steering. *Optica* 2016, 3, 887-890.

[27] Shin, D.; Shin, G.; Lee, J.; Hwang, I.; Otsuka, T.; Byun, H.; Lee, C.; Shim, D.; Lee, E.; Ha, K.; etc. Aperiodic Optical Phased Array based on Number Theory. *Submitted* 2023.

[28] Fatemi, R.; Khachaturian, A.; Hajimiri, A. A Nonuniform Sparse 2-D Large-FOV Optical Phased Array with a Low-Power PWM Drive. *IEEE Jour. Sol. Stat. Cir. Soc.* 2019, 54, 1200-1215.

[29] Kazemian, A.; Wang, P.; Zhuang, Y.; Yi, Y. Optimization of the Silicon-Based Aperiodic Optical Phased Array Antenna. *Opt. Lett.* 2021, 46, 801-804.

[30] Xue, Y.; Zhang, Q.; Ren, Y.; Lei, Y.; Sun, X.; Zhang, L. Two-Dimensional Single-Lobe Si Photonic Optical Phased Array with Minimal Antennas Using a Non-Uniform Large Spacing Array Design. *Appl. Opt.* 2022, 61, 7158-7162.

[31] Zhang, F.; Zhang, D.; Pan, S. Fast and Wide-Range Optical Beam Steering with Ultralow Side Lobes by Applying an Optimized Multi-Circular Optical Phased Array. *Appl. Opt.* 2018, 57, 4977-4984.

[32] Wang, P.; Luo, G.; Li, Y.; Wang, M.; Meng, F.; Yang, W.; Yu, H.; Zhou, X.; Zhang, Y.; Pan, J. Two-Dimensional Large-Angle Scanning Optical Phased Array with Single Wavelength Beam. *CLEO* 2019, HTh2A.72.

[33] Liu, X.; Xiong, B.; Sun, C.; Hao, Z.; Wang, L.; Wang, J.; Han, Y.; Li, H.; Luo, Y. Circular Optical Phased Array for 360 Constant Amplitude Scanning. *Tenth Int. Conf. Infor. Opt. Pho.* 2018, 10964, 1044-1048.

[34] Liu, Q.; Benedikovic, D.; Smy, T.; Atieh, A.; Cheben, P.; Ye, W.N. Circular Optical Phased Arrays with Radial Nano-Antennas. *Nanomater* 2022, 12, 1938.

[35] Benedikovic, D.; Liu, Q.; Postigo, A.S.; Atieh, A.; Smy, T.; Cheben, P.; Ye, W.N. Circular Optical Phased Array with Large Steering Range and High Resolution. *Sensors* 2022, 22, 6135.

[36] Zhang, Y.; Ling, Y.C.; Zhang, K.; Gentry, C.; Sadighi, D.; Whaley, G.; Colosimo, J.; Suni, P.; Yoo, S.J.B. Sub-Wavelength-Pitch Silicon-Photonic Optical Phased Array for Large-Field-of-

Regard Coherent Optical Beam Steering. *Opt. Exp.* 2019, 27, 1929-1940.

[37] Phare, C.T.; Shin, M.C.; Miller, S.A.; Stern, B.; Lipson, M. Silicon Optical Phased Array with High-Efficiency Beam Formation over 180 Degree Field of View. *arXiv* 2018, arXiv:1802.04624.

[38] Yi, X.; Zeng, H.; Gao, S.; Qiu, C. Design of an Ultra-Compact Low-Crosstalk Sinusoidal Silicon Waveguide Array for Optical Phased Array. *Opt. Exp.* 2020, 28, 37505-37513.

[39] Yi, X.; Zhang, Y.; Zeng, H.; Gao, S.; Guo, S.; Qiu, C. Demonstration of an Ultra-Compact 8-Channel Sinusoidal Silicon Waveguide Array for Optical Phased Array. *Opt. Lett.* 2022, 47, 226-229.

[40] Liang, D.; Li, W.; Wang, X.; Zhao, X.; Guo, Z.; Han, X.; Chen, J.; Dai, D.; Shi, Y. Grating Lobe-Free Silicon Optical Phased Array with Periodically Bending Modulation of Dense Antennas. *Opt. Exp.* 2023, 31, 11423-11430.

[41] Kong, Z. Design and Characterization of Optical Phased Array with Half-Wavelength Spacing. *Diss. Purdue University Graduate School* 2021.

[42] Zhang, L.; Li, Y.; Hou, Y.; Wang, Y.; Tao, M.; Chen, B.; Na, Q,; Li, Y.; Zhi, Z.; Liu, X.; etc. Investigation and Demonstration of a High-Power Handling and Large-Range Steering Optical Phased Array Chip. *Opt. Exp.* 2021, 29, 29755-29765.

[43] Liu, Y.; Hu, H. Silicon Optical Phased Array with a 180- Degree Field of View for 2D Optical Beam Steering. *Optica* 2022, 9, 903-907.

[44] Lei, Y.; Zhang, L.; Xue, Y.; Ren, Y.; Zhang, Q.; Zhang, W.; Sun, X. Effective Half-Wavelength Pitch Optical Phased Array Design for Aliasing-Free 2D Beam Steering. *Appl. Opt.* 2022, 61, 9423-9428.

[45] Poulton, C.V.; Byrd, M.J.; Raval, M.; Su, Z.; Li, N.; Timurdongan, E.; Coolbaugh, D.; Vermeulen, D.; Watts, M.R. Large-Scale Silicon Nitride Nanophotonic Phased Arrays at Infrared and Visible Wavelengths. *Opt. Lett.* **2017**, 42, 21-24.

[46] Dostart, N.; Zhang, B.; Khilo, A.; Brand, M.; Qubaisi, K.A.; Onural, D.; Feldkhun, D.; Wagner, K.H.; Popovic, M.A. Serpentine Optical Phased Arrays for Scalable Integrated Photonic Lidar Beam Steering. *Optica* **2020**, 7, 726-733.

[47] Sun, J.; Hosseini, E.S.; Yaacobi, A.; Cole, D.B.; Leake, G.; Coolbaugh, D.; Watts, M.R. Two-Dimensional Apodized Silicon Photonic Phased Arrays. *Opt. Lett.* **2014**, 39, 367-370.

[48] Kwong, D.; Hosseini, A.; Covey, J.; Xu, X.; Zhang, Y.; Chakravarty, S.; Chen, R.T. Corrugated Waveguide-based Optical Phased Array with Crosstalk Suppression. *IEEE Photon. Technol. Lett.* **2014**, 26, 991-994.

[49] Im, C.S.; Bhandari, B.; Lee, K.P.; Kim, S.M.; Oh, M.C.; Lee, S.S. Silicon Nitride Optical Phased Array based on a Grating Antenna Enabling Wavelength-Tuned Beam Steering. *Opt. Exp.* **2020**, 28, 3270-3279.

[50] Wu, D.; Guo, W.; Yi, Y. Compound Period Grating Coupler for Double Beam Generation and Steering. *Appl. Opt.* **2019**, 58, 361-367.

[51] Liu, Y.; Hao, Z.; Wang, L.; Xiong, B.; Sun, C.; Wang, J.; Li, H.; Han, Y.; Luo, Y. A Single-Chip Multi-Beam Steering Optical Phased Array: Design Rules and Simulations. *Opt. Exp.* **2021**, 29, 7049-7059.

[52] Zeng, Y.S.; Qu, S.W.; Wu, J.W. Polarization-Division and Spatial-Division Shared-Aperture Nanopatch Antenna Arrays for Wide-Angle Optical Beam Scanning. *Opt. Exp.* **2020**, 28, 12806-12826.

[53] Zhao, S.; Chen, J.; Shi, Y. Dual Polarization and Bi-Directional Silicon-Photonic Optical Phased Array with Large Scanning Range. *IEEE Photon. J.* **2022**, 14, 6620905.

[54] Kondo, K.; Tatebe, T.; Hachuda, S.; Abe, H.; Koyama, F.; Baba, T. Fan-Beam Steering Device using a Photonic Crystal Slow-Light Waveguide with Surface Diffraction Grating. *Opt. Lett.* **2017**, 42, 4990-4993.

[55] Abe, H.; Takeuchi, M.; Takeuchi, G.; Ito, H.; Yokokawa, T.; Kondo, K.; Furukado, Y.; Baba, T. Two-Dimensional Beam-Steering Device using a Doubly Periodic Si Photonic-Crystal Waveguide. *Opt. Exp.* **2018**, 26, 9389-9397.

[56] Takeuchi, G.; Terada, Y.; Takeuchi, M.; Abe, H.; Ito, H.; Baba, T. Thermally Controlled Si Photonic Crystal Slow Light Waveguide Beam Steering Device. *Opt. Exp.* **2018**, 26, 11529-11537.

[57] Gondo, J.; Ito, H.; Tamanuki, T,; Baba, T. Space-Time-Domain Observation of High-Speed Optical Beam Scanning in a Thermo-Optic Si Photonic Crystal Slow-Light Beam Scanner. *Opt. Lett.* **2021**, 46, 3600-3603.

[58] Yaacobi, A.; Sun, J.; Moresco, M.; Leake, G.; Coolbaugh, D.; Watts, M.R. Integrated Phased Array for Wide-Angle Beam Steering. *Opt. Lett.* **2014**, 39, 4575-4578.

[59] Shang, K.; Qin, C.; Zhang, Y.; Liu, G.; Xiao, X.; Feng, S.; Yoo, S.J.B. Uniform Emission, Constant Wavevector Silicon Grating Surface Emitter for Beam Steering with Ultra-Sharp Instantaneous Field-of-View. *Opt. Exp.* **2017**, 25, 19655-19661.

[60] Zadka, M.; Chang, Y.C.; Mohanty, A.; Phare, C.T.; Roberts, S.P.; Lipson, M. On-Chip Platform for a Phased Array with Minimal Beam Divergence and Wide Field-of-View. *Opt. Exp.* **2018**, 26, 2528-2534.

[61] Zhang, Z.; Yu, H.; Chen, B.; Xia, P.; Zhou, Z.; Huang, Q.; Dai, T.; Wang, Y.; Yang, J. A Tri-Layer Si3N4-on-Si Optical Phased Array with High Angular Resolution. *IEEE Photon. Technol. Lett.* **2022**, 34, 1108-1111.

[62] Han, K.; Yurlov, V.; Yu, N.E. Highly Directional Waveguide Grating Antenna for Optical Phased Array. *Curr. Appl. Phys.* **2018**, 18, 824-828.

[63] Wang. P.F.; Luo, G.Z.; Yu, H.Y.; Li, Y.J.; Wang, M.Q.; Zhou, X.L.; Chen, W.X.; Zhang, Y.J.; Pan, J.Q. Improving the Performance of Optical Antenna for Optical Phased Arrays through High-Contrast Grating Structure on SOI Substrate. *Opt. Exp.* **2019**, 27, 2703-2712.

[64] Wang, Q.; Wang, S.; Zeng, Y.; Wang, W.; Cai, Y.; Tu, Z.; Yue, W.; Wang, X.; Fang, Q.; Yu, M. Dual-Layer Waveguide Grating Antenna with High Directionality for Optical Phased Arrays. *Appl. Opt.* **2019**, 58, 5807-5811.

[65] Ravel, M.; Poulton, C.V.; Watts, M.R. Unidirectional Waveguide Grating Antennas with Uniform Emission for Optical Phased Arrays. *Opt. Lett.* **2017**, 42, 2563-2566.

[66] Chen, B.; Li, Y.; Zhang, L.; Li, Y.; Liu, X.; Tao, M.; Hou, Y.; Tang, H.; Zhi, Z.; Gao, F.; etc. Unidirectional Large-Scale Waveguide Grating with Uniform Radiation for Optical Phased Array. *Opt. Exp.* **2021**, 29, 20995-21010.

[67] Kim, S.H.; You, J.B.; Ha, Y.G.; Kang, G.; Lee, D.S.; Yoon, H.; Yoo, D.E.; Lee, D.W.; Yu, K.; Youn, C.H.; etc. Thermo-Optic Control of the Longitudinal Radiation Angle in a Silicon-based Optical Phased Array. *Opt. Lett.* **2019**, 44, 411-414.

[68] Yang, B.; Chen, H.; Yang, S.; Chen, M. A Design Method of Optical Phased Array with Insufficient Phase Tuning Range. *IEEE Photon. J.* **2020**, 12, 6600409.

[69] Wang, Y.; Liang, L.; Chen, Y.; Jia, P.; Qin, L.; Liu, Y.; Ning, Y.; Wang, L.; Improved Performance of Optical Phased Arrays Assisted by Transparent Graphene Nanoheaters and Air Trenches. *RSC. Adv.* **2018**, 8, 8442-8449.

[70] Kim, S.M.; Park, T.H.; Im, C.S.; Lee, S.S.; Kim, T.; Oh, M.C. Temporal Response of Polymer Waveguide Beam Scanner with Thermo-Optic Phase-Modulator Array. *Opt. Exp.* **2020**, 28, 3768-3778.

[71] Larocque, H.; Ranzani, L.; Leatham, J.; Tate, J.; Niechayev, A.; Yengst, T.; Komljenovic, T.; Fodran, C.; Smith, D.; Soltani, M. Beam Steering with Ultracompact and Low-Power Silicon Resonator Phase Shifters. *Opt. Exp.* **2019**, 27, 34639-34654.

[72] Miller, S.A.; Chang, Y.C.; Phare, C.T.; Shin, M.C.; Zadka, M.; Roberts, S.P.; Stern, B.; Ji, X.; Mohanty, A.; Gordillo, O.A.J.; etc. Large-Scale Optical Phased Array using a Low-Power Multi-Pass Silicon Photonic Platform. *Optica* **2020**, 7, 3-6.

[73] Kang, G.; Kim, S.H.; You, J.B.; Lee, D.S.; Yoon, H.; Ha, Y.G.; Kim, J.H.; Yoo, D.E.; Lee, D.W.; Youn, C.H.; etc. Silicon-based Optical Phased Array using Electro-Optic p-i-n Phase Shifters. *IEEE Photon. Technol. Lett.* **2019**, 31, 1685-1688.

[74] Bowers, J.E.; Xie, W.; High-Performance III-V/Si Phase Shifter Arrays for Beam Steering. *IEEE SUM* **2019**, 1-2.

[75] Hirano, Y.; Miyamoto, Y.; Miura, M.; Motoyama, Y.; Machida, K.; Yamada, T.; Otomo, A.; Kikuchi, H. High-Speed Optical-Beam Scanning by an Optical Phased Array using Electro-Optic Polymer Waveguides. *IEEE Photon. J.* **2020**, 12, 6600807.

[76] Poulton, C.V.; Byrd, M.J.; Russo, P.; Moss, B.; Shatrovoy, O.; Khandaker, M.; Watts, M.R. Coherent LiDAR with an 8192-Element Optical Phased Array and Driving Laser. *IEEE J. Sel. Top. Quantum Electron.* **2022**, 28, 1-8.

[77] Vasey, F.; Reinhart, F.K.; Houdre, R.; Stauffer, M. Spatial Optical Beam Steering with an AlGaAs Integrated Phased Array. *Appl. Opt.* **1993**, 32, 3220-3232.

[78] Rabinovich, W.; Goetz, P.; Pruessner, M.; Mahon, R.; Ferraro, M.; Park, D.; Fleet, E.; DePrenger, M.J. Free Space Optical Communication Link using a Silicon Photonic Optical Phased Array. *FS Lase. Com. and Atm. Propagation XXVII* **2015**, 9354, 96-101.

[79] Poulton, C.V.; Yaacobi, A.; Cole, D.B.; Byrd, M.J.; Raval, M.; Vermeulen, D.; Watts, M.R. Coherent Solid-State LIDAR with Silicon Photonic Optical Phased Arrays. *Opt. Lett.* **2017**, 42, 4091-4094.

[80] Li, W.; Chen, J.; Liang, D.; Dai, D.; Shi, Y. Silicon Optical Phased Array with Calibration-Free Phase Shifters. *Opt. Exp.* 2022, 30, 44029-44038.

[81] Ashtiani, F.; Aflatouni, F. N X N Optical Phased Array with 2N Phase Shifters. *Opt. Exp.* **2019**, 27, 27183-27190.

[82] Wu, D.; Yu, B.; Yi, Y. Phase-Combining Unit for Aliasing Suppression in an Optical Phased Array. *Opt. Lett.* **2022**, 47, 1996-1999.

[83] Doyleng, J.K.; Heck, M.J.R.; Bovington, J.T.; Peters, J.D.; Davenport, M.L.; Coldren, L.A.; Bowers, J.E. Hybrid III/V Silicon Photonic Source with Integrated 1D Free-Space Beam Steering. *Opt. Lett.* **2012**, 37, 4257-4259.

[84] Guo, W.; Binetti, P.R.A.; Althouse, C.; Masanovic, M.L.; Ambrosius, H.P.M.M.; Johansson, L.A.; Coldren, L.A. Two-Dimensional Optical Beam Steering with InP-based Photonic Integrated Circuits. *IEEE J. Sel. Top. Quantum Electron.* **2013**, 19, 6100212.

[85] Hulme, J.C.; Doyleng, J.K.; Heck, M.J.R.; Peters, J.D.; Davenport, M.L.; Bovington, J.T.; Coldren, L.A.; Bowers, J.E. Fully Integrated Hybrid Silicon Free-Space Beam Steering Source

with 32 Channel Phased Array. *Smart Photonic Optoelectron. Integ. Circuits XVI* **2014**, 8989, 898907.

[86] Hulmer, J.C.; Doyleng, J.K., Heck, M.J.R.; Peters, J.D.; Davenport, M.L.; Bovington, J.T.; Coldren, L.A.; Bowers, J.E. Fully Integrated Hybrid Silicon Two Dimensional Beam Scanner. *Opt. Exp.* **2015**, 23, 5861-5874.

[87] Notaros, J.; Li, N.; Poulton, C.V.; Su, Z.; Byrd, M.J.; Magden, E.S.; Timurdogan, E.; Baiocco, C.; Fahrenkopf, N.M.; Watts, M.R. CMOS-Compatible Optical Phased Array Powered by a Monolithically-Integrated Erbium Laser. *J. Lightwave Technol.* **2019**, 37, 5982-5987.

[88] Yue, J.; Cui, A.; Wang, F.; Han, L.; Dai, J.; Sun, X.; Lin, H.; Wang, C.; Chen, C.; Zhang, D. Design of Monolithic 2D Optical Phased Arrays Heterogeneously Integrated with on-Chip Laser Arrays based on SOI Photonic Platform. *Micromachines* 2022, 13, 2117.

[89] Misugi, Y.; Okayama, H.; Kita, T. Compact and Low Power-Consumption Solid-State Two-Dimensional Beam Scanner Integrating a Passive Optical Phased Array and Hybrid Wavelength-Tunable Laser Diode. *J. Lightwave Technol.* **2023**, accepted.

[90] Zhou, J.; Sun, J.; Yaacobi, A.; Poultion, C.V.; Watts, M.R. Design of 3D Hologram Emitting Optical Phased Arrays. *Adv. Photon.* **2015**, IT4A.7.

[91] Guerber, S.; Fowler, D.; Tovar, J.F.; Carim, K.A.; Delplanque, B.; Szelag, B. Wafer-Level Calibration of Large-Scale Integrated Optical Phased Arrays. *Opt. Exp.* **2022**, 30, 35246-35255.

[92] Komljenvoic, T.; Pintus, P.; On-Chip Calibration and Control of Optical Phased Arrays. *Opt. Exp.* **2018**, 26, 3199-3210.

[93] Zhang, W.; Li, L.; Chen, W. A Chaotic Stochastic Parallel Gradient Descent Algorithm for Fast Phase Correction of Optical Phased Array. *CIOP* **2019**, 11209, 1120956.

[94] Jin, J.; Lee, E.S.; Chun, K.W.; Lee, S.S.; Oh, M.C. Fast-Running Beamforming Algorithm for Optical Phased Array Beam Scanners Comprised of Polymeric Waveguide Devices. *Opt. Exp.* 2022, 30, 768-779.

[95] Zhang, Q.; Zhang, L.; Li, Z.; Wu, W.; Wang, G.; Sun, X.; Zhang, W.; Zhang, W. An Antenna Array Initial Condition Calibration Method for Integrated Optical Phased Array. *arXiv* **2019**, arXiv:1902.06203.

[96] Sung, J.Y.; Lee, S.L.; Fast Phase Error Calibration through Radix-P Optimization Processing. *Opt. Exp.* **2021**, 29, 41776-41787.

[97] Huang, Y.; Wang, K.; Yan, Q.; Wang, Y.; Wang, X.; Liu, H.; Feng, J.; Zhang, F.; Feng, Z.; Siviloglou, G.A. Universal Dimension Reduced Phase Compensation Algorithm for an Optical Phased Array. *Opt. Lett.* **2022**, 47, 2871-2874.

[98] Li, L.J.; Chen, W.; Zhao, X.Y.; Sun, M.J. Fast Optical Phased Array Calibration Technique for Random Phase Modulation LiDAR. *IEEE Photon. J.* **2019**, 11, 6900410.

[99] Zhang, H.; Zhang, Z.; Peng, C.; Hu, W. Phase Calibration of on-Chip Optical Phased Arrays via Interference Technique. *IEEE Photon. J.* **2022**, 12, 6600210.

[100] Yepez, P.A.K.; Scholz, U.; Zimmermann, A. Temperature Dependence of the Steering Angles of a Silicon Photonic Optical Phased Array. *IEEE Photon. J.* **2020**, 12, 6800813.

[101] Shim, J.; You, J.B.; Rhee, H.W.; Yoon, H,; Kim, S.H.; Yu, K.; Park, H.H. On-Chip Monitoring of Far-Field Patterns using a Planar Diffractor in a Silicon-based Optical Phased Array. *Opt. Lett.* **2020**, 45, 6058-6061.

[102] Xiao, F.; Hu, W.; Xu, A. Optical Phased-Array Beam Steering Controlled by Wavelength. *Appl. Opt.* **2005**, 44, 5429-5433.

[103] Kim, J.Y.; Yoon, J.; Kim, J.; Kwon, N.H.; Rhee, H.W.; Baek, M.; Lee, Y.; Park, H.H.; Yoon, H. Demonstration of Beam Steering using a Passive Silica Optical Phased Array with Wavelength Tuning. *Opt. Lett.* **2022**, 47, 4857-4860.

[104] Acoleyen, K.V.; Rogier, H.; Baets, R. Two-Dimensional Optical Phased Array Antenna on Silicon-on-Insulator. *Opt. Exp.* **2010**, 18, 13655-13660.

[105] Acoleyen, K.V.; Bogaerts, W.; Baets, R. Two-Dimensional Dispersive Off-Chip Beam Scanner Fabricated on Silicon-on-Insulator. *IEEE Photon. Technol. Lett.* **2011**, 23, 1270-1272.

[106] Yoon, H.; Rhee, H.W.; Kwon, N.H.; Kim, J.Y.; Kim, J.; Yoon, J.; Park, H.H. Demonstration of Two-Dimensional Beam Steering through Wavelength Tuning with One-Dimensional Silicon Optical Phased Array. *MDPI Photon.* **2022**, 9, 812.

[107] Martin, A.; Dodane, D.; Leviandier, L.; Dolfi, D.; Naughtom, A.; O'Brien, P.; Spuessens, T.; Baets, R.; Kepage, G.; Verheyen, P.; etc. Photonic Integrated Circuit-based FMCW Coherent LiDAR. *J. Lightwave Technol.* **2018**, 36, 4640-4645.

[108] Zhang, L.; Li, Y.; Chen, B.; Wang, Y.; Li, H.; Hou, Y.; Tao, M.; Li, Y.; Zhi, Z.; Liu, X.; etc. Two-Dimensional Multi-Layered SiN-on-SOI Optical Phased Array with Wide-Scanning and Long-Distance Ranging. *Opt. Exp.* **2022**, 30, 5008-5018.

[109] Suyama, S.; Ito, H.; Kurahashi, R.; Abe, H.; Baba, T. Doppler Velocimeter and Vibrometer FMCW LiDAR with Si Photonic Crystal Beam Scanner. *Opt. Exp.* **2021**, 29, 30727-30734.

[110] Zhang, M.; Wang, Y.; Zhang, L.; Hu, Q.; Zhao, S.; Liang, L.; Chen, Y.; Qin, L.; Song, J.; Wang, L. Phase-Modulated Continuous-Wave Coherent Ranging Method for Optical Phased Array Lidar. *Opt. Exp.* **2023**, 31, 6514-6528.

[111] Fantoni, A.; Lourenco, P.; Costa, J.; Vieira, M. Amorphous Silicon Photonic Optical Phased Array for Beam Steering. *Physics and Simulation Optoelectron. Devices XXXI* **2023**, 12415, 124150G.

[112] Sabouri, S.; Jamshidi, K. Design Considerations of Silicon Nitride Optical Phased Array for Visible Light Communications. *IEEE J. Sel. Top. Quan. Elec.* **2018**, 24, 8300707

[113] Zhu, S.; Hu, T.; Li, Y.; Xu, Z.; Zhong, Q.; Dong, Y.; Singh, N. CMOS-Compatible Integrated Silicon Nitride Optical Phase Array for Electrically Tunable Off-Chip Laser Beam Steering. *IEEE EDTM* **2019**, 228-230.

[114] Sun, C.; Li, B.; Shi, W.; Lin, J.; Ding, N.; Tsang, H.K.; Zhang, A. Large-Scale and Broadband Silicon Nitride Optical Phased Arrays. *IEEE J. Sel. Top. Quan. Elec.* **2022**, 28, 8200710.

[115] Tyler, N.A.; Fowler, D.; Malhouitre, S.; Garcia, S.; Grosse, P.; Rabaud, W.; Szelag, B. SiN Integrated Optical Phased Arrays for Two-Dimensional Beam Steering at a Single Near-Infrared Wavelength. *Opt. Exp.* **2019**, 27, 5851-5858.

[116] Wang, P.; Luo, G.; Xu, Y.; Li, Y.; Su, Y.; Ma, J.; Wang, R.; Yang, Z.; Zhou, X.; Zhang, Y. Design and Fabrication of a SiN-Si Dual-Layer Optical Phased Array Chip. *Photonics Res.* **2020**, 8, 912-919.

[117] Wang, Q.; Wang, S.; Jia, L.; Cai, Y. Yue, W.; Yu, M. Silicon Nitride Assisted 1 X 64 Optical Phased Array based on a SOI Platform. *Opt. Exp.* **2021**, 29, 10509-10517.

[118] Li, Y.; Chen, B.; Na, Q.; Xie, Q.; Tan, M.; Zhang, L.; Zhi, Z.; Li, Y.; Liu, X.; Luo. X.; etc. Wide-Steering-Angle High-Resolution Optical Phased Array. *Photonics Res.* **2020**, 8, 2511-2518.

[119] Zhang, L.; Li, Y.; Hou, Y.; Wang, Y.; Tao, M.; Chen, B.; Na, Q.; Li, Y.; Zhi, Z.; Liu, X. etc. Investigation and Demonstration of a High-Power Handling and Large-Range Steering Optical Phased Array Chip. *Opt. Exp.* **2021**, 29, 29755-29765.

[120] Prost, M.; Ling, Y.C.; Cakmakyapan, S.; Zhang, Y.; Zhang, K.; Hu, J.; Zhang, Y.; Yoo, S.J.B. Solid-State MWIR Beam Steering using Optical Phased Array on Germanium-Silicon Photonic Platform. *IEEE Photon. J.* **2019**, 11, 6603909.

[121] Midkiff, J.; Yoo, K.M.; Shin, J.D.; Dalir, H.; Teimourpour, M.; Chen, R.T. Optical Phased Array Beam Steering in the Mid-Infrared on an InP-based Platform. *Optica* **2020**, 7, 1544-1547.

[122] Sun, J.; Moresco, M.; Leake, G.; Coolbaugh, D.; Watts, M.R. Generating and Identifying Optical Orbital angular Momentum with Silicon Photonic Circuits. *Opt. Lett.* **2014**, 39, 5977-5980.

[123] Notaros, J.; Poulton, C.V.; Byrd, M.J.; Raval, M.; Watts, M.R. Integrated Optical Phased Arrays for Quasi-Bessel-Beam Generation. *Opt. Lett.* **2017**, 42, 3510-3513.

[124] Notaros, J.; Poulton, C.V.; Raval M.; Watts, M.R. Near-Field-Focusing Integrated Optical Phased Arrays. *J. Lightwave Technol.* **2018**, 36, 5912-5920.

[125] Raval, M.; Yaacobi, A.; Watts, M.R. Integrated Visible Light Phased Array System for Autostereoscopic Image Projection. *Opt. Lett.* **2018**, 43, 3678-3681.

[126] Kohno, Y.; Komatsu, K.; Tang, R.; Ozeki, Y.; Nakano, Y.; Tanemura, T. Ghost Imaging using a Large-Scale Silicon Photonic Phased Array Chip. *Opt. Exp.* 2019, 27, 3817-3823.

[127] Wang, Z.; Sun, Y.; Liao, J.; Wang, C.; Cao, R.; Cao, C. High-Resolution Dynamic Imaging System based on a 2D Optical Phased Array. *Opt. Exp.* **2021**, 29, 39342-39351.

[128] Fatemi, R.; Abiri, B.; Khachaturian, A.; Hajimiri, A. High-Sensitivity Active Flat Optics Optical Phased Array Receiver with a Two-Dimensional Aperture. *Opt. Exp.* **2018**, 26, 29983-29999.

[129] Acoleyen, K.V.; O'Brien, D.C.; Payne, F.; Bogaerts, W.; Baets, R. Optical Retroreflective Marker Fabricated on Silicon-on-Insulator. *IEEE Photon. J.* **2011**, 3, 789-798.

[130] Abiri, B.; Fatemi, R.; Hajimiri, A.; A 1-D Heterodyne Lens-Free Optical Phased Array Camera with Reference Phase Shifting. *IEEE Photon. J.* **2018**, 10, 6601712.

[131] Abediasl, H.; Hashemi, H. Monolithic Optical Phased-Array Transceiver in a Standard SOI CMOS Process. *Opt. Exp.* **2015**, 23, 6509-6519.

[132] Zhang, Y.; Wang, R.; Wei, M. Two-Dimensional High-Efficiency Transceiver Integrated Optical Phased Array with Dual-Port Antenna. *IEEE Photon. J.* **2022**, 14, 5047605.

[133] Dostart, N.; Zhang, B.; Brand, M.; Qubaisi, K.A.; Onural, D.; Feldkjun, D.; Popovic, M.; Wagner, K. Vernier Optical Phased Array Lidar Transceivers. *Opt. Exp.* **2022**, 30, 24589-24601.

[134] Poulton, C.V.; Vermeulen, D.; Hosseini, E.; Timurdogan, E.; Su, Z.; Moss, B.; Watts, M.R. Lens-Free Chip-to-Chip Free-Space Laser Communication Link with a Silicon Photonics Optical Phased Array. *Frontiers in Optics* **2017**, FW5A.3.

[135] Poulton, C.V.; Byrd, M.; Russo, P.; Timurdogan, E.; Khandaker, M.; Vermeulen, D.; Watts, M.R. Long-Range LiDAR and Free-Space Data Communication with High-Performance Optical Phased Arrays. *IEEE J. Sel. Top. Quan. Elec.* **2019**, 25, 7700108.

[136] Foster, A.C.; Kossey, M.; MacFarlane, N.; Rizk, C.; Kott, T.; Osiander, R.; Mosavi, N. Chip-Scale Optical Phased Arrays for Inter-Spacecraft Communications. *Micro- Nanotech. Sens. Syst. Appl. XI* **2019**, 10982, 109820H-1.

[137] Rhee, H.W.; You, J.B.; Yoon, H.; Han, K.; Kim, M.; Lee, B.G.; Kim, S.C.; Park, H.H. 32 Gbps Data Transmission with 2D Beam-Steering using a Silicon Optical Phased Array. *IEEE Photon. Technol. Lett.* **2020**, 32, 803-806.

[138] Chow, C.W.; Chang, Y.C.; Kuo, S.; Kuo, P.C.; Wang, J.W.; Jian, Y.H.; Ahmad, Z.; Fu, P.H.; Shi, J.W.; Huang, D.W.; Hung, T.Y.; etc. Actively Controllable Beam Steering Optical Wireless Communication (OWC) using Integrated Optical Phased Array (OPA). *J. Lightwave Technol.* **2023**, 41, 1122-1128.

[139] Kossey, M.R.; Alt, S.; Rizk, C.; Foster, A.C.; Integrated Photonic Arrays as a Platform for Infrared Neural Stimulation. *Opt. Life Sci.* **2017**, BoS2A.8.

[140] Sacher, W.D.; Liu, X.; Chen, F.D.; Chameh, H.M.; Almog, I.F.; Lordello, T.; Chang, M.; Naderian, A.; Fowler, T.M.; Segev, E.; etc. Beam Steering Nanophotonic Phased-Array Neural Probes. *CLEO* **2019**, ATh4l.4.

[141] Guan, B.; Qin, C.; Scott, R.P.; Ercan, B.; Fontaine, N.K.; Su, T.; Yoo, S.J.B. Hybrid 3D Photonic Integrated Circuit for Optical Phased Array Beam Steering. *CLEO* **2015**, STU2F.1.

[142] Hosseini, A.; Kwong, D.; Zhao, Y.; Chen, Y.S.; Crnogorac, F.; Pease, R.F.W.; Chen, R.T. Unequally Spaced Waveguide Arrays for Silicon Nanomembrane-based Efficient Large Angle Optical Beam Steering. *IEEE J. Sel. Top. Quan. Elec.* **2009**, 15, 1439-1446.

[143] Hosseini, A.; Kwong, D.; Zhang, Y.; Chandorkar, S.A.; Crnogorac, F.; Carlson, A.; Fallah, B.; Bank, S.; Tutuc, E.; Rogers, J.; etc. On the Fabrication of Three-Dimensional Silicon-on-Insulator based Optical Phased Array for Agile and Large Angle Laser Beam Steering Systems. *J. Vac. Sci. Technol. B* **2010**, 28, C6O1-C6O7.

[144] Wu, D.; Yi, Y.; Zhang, Y. High-Efficiency End-Fire 3D Optical Phased Array based on a Multi-Layer Si3N4/SiO2 Platform. *Appl. Opt.* **2020**, 59, 2489-2497.

[145] Wu, D.; Yu, B.; Kakdarvishi, V.; Yi, Y. Photonic Integrated Circuit with Multiple Waveguide Layers for Broadband High-Efficient 3D OPA. *Opt. Lett.* **2023**, 48, 968-971.

[146] Wang, P.; Kazemian, A.; Zeng, X.; Zhuang, Y.; Yi, Y. Optimization of Aperiodic 3D Optical Phased Arrays based on Multilayer Si3N4/SiO2 Platforms. *Appl. Opt.* **2021**, 60, 484-491.

[147] Wu, D.; Owen, K.; Yu, B.; Yi, Y. Fabrication of a Self-Aligned Multi-Waveguide-Layer Passive Si3N4/SiO2 Photonic Integrated Circuit for a 3-D Optical Phased Array Device. *Opt. Mater. Exp.* **2023**, accepted.

[148] E. Garmire, J. M. Hammer, H. Kogelnik, and F. Zernike. Integrated Optics, 2013.[149] T. Tamir and S. T. Peng, "Analysis and design of grating couplers," *Appl. Phys.* 14, 235–254 (1977).

[150] M. G. Moharam and T. K. Gaylord, "Diffraction analysis of dielectric surface-relief gratings," *J. Opt. Soc. Am.* 72, 1385–1392 (1982).

[151] S. Selvaraja, P. Jaenen, W. Bogaerts, P. Dumon, D. Van Thourhout, and R. Baets, "Fabrication of photonic wire and crystal circuits in silicon-on-insulator using 193 nm optical lithography," *J. Lightwave Technol.* 27, 4076–4083 (2009).

[152] R. Waldhäusl, B. Schnabel, P. Dannberg, E.-B. Kley, A. Bräuer, and W. Karthe, "Efficient coupling into polymer waveguides by gratings," *Appl. Opt.* 36, 9383–9390 (1997).

[153] J. Yang, Z. Zhou, H. Jia, X. Zhang, and S. Qin, "High-performance and compact binary blazed grating coupler based on an asymmetric subgrating structure and vertical coupling," *Opt. Lett.* 36, 2614–2617 (2011).

[154] Z. Cheng and H. K. Tsang, "Experimental demonstration of polarization-insensitive air-cladding grating couplers for silicon-on-insulator waveguides," *Opt. Lett.* 39(7), 2206–2209 (2014).

[155] J. H. Song, F. E. Doany, A. K. Medhin, N. Dupuis, B. G. Lee, and F. R. Libsch, "Polarization-independent nonuniform grating couplers on silicon-on-insulator," *Opt. Lett.* 40(17), 3941-3944 (2015).

[156] C. Alonso-Ramos, L. Zavargo-Peche, A. Ortega-Moñux, R. Halir, I. Molina-Fernández, and P. Cheben, Polarization-independent grating coupler for micrometric silicon rib waveguides. *Opt. Lett.* 37(17), 3663–3665 (2012).

[157] W. S. Zaoui, A. Kunze, W. Vogel, M. Berroth, J. Butschke, F. Letzkus, and J. Burghartz, Bridging the gap between optical fibers and silicon photonic integrated circuits. *Opt. Exp.*, 22(2), 1277–1286 (2014).

[158] X. Dan-Xia, J. H. Schmid, G. T. Reed, G. Z. Mashanovich, D. J. Thomson, M. Nedeljkovic, C. Xia, D. Van Thourhout, S. Keyvaninia, and S. K. Selvaraja, Silicon photonic integration platform-Have we found the sweet spot? *IEEE J. Sel. Top. Quantum Electron.* 20(4), 189–205 (2014).

[159] L. Zhu, W. Yang, and C. Chang-Hasnain, Very high efficiency optical coupler for silicon nanophotonic waveguide and single mode optical fiber. *Opt. Exp*. 25(15), 18462–18473 (2017).

[160] H. Wang, T. Luo, H. Song, and J. B. Christen. On-chip sensor for light direction detection. *Opt. Lett.* 38(22), 4554-4557 (2013)

[161] H. T. Chorsi, Y. Lee, A. Alu, and J. X. J. Zhang, Tunable plasmonic substrates with ultrahigh Q-factor resonances. *Sci. Rep.*, 7(1), 1–9 (2017)

[162] H. T. Chorsi, and S. D. Gedney, Tunable plasmonic optoelectronic devices based on graphene metasurfaces. *IEEE Pho. Tech. Lett.*, 29(2), 228-230 (2016)

[163] T. Kim, P. Bhargava, C. V. Poulton, J. Notaros, A. Yaacobi, E. Timurdogan, C. Baiocco, N. Fahrenkopf, S. Kruger, T. Ngai, Y. Timalsina, and M. R. Watts, A Single-Chip Optical Phased

Array in a Wafer-Scale Silicon Photonics/CMOS 3D-Integration Platform. *IEEE Jour. of Sol. Cir.*, 54(11), 3061-3074 (2019)

[164] X. Wang, X. Quan, M. Liu, and X. Cheng, Silicon-nitride-assisted edge coupler interfacing with high numerical aperture fiber. *IEEE Photonics Tech. Lett.*, 31(5), 349-352 (2019).

[165] N. Kohli, M. Ménard, and N.Y. Winnie, Efficient TE/TM spot-size converter for broadband coupling to single mode fibers. *OSA Continuum*, 2(8), 2428-2438 (2019).

[166] V.C. Coffey, Integrated Lidar: Transforming Transportation. *Opt. & Pho. News* 30, 40-47 (2019).

[167] J. Hecht, Lidar for Self-Driving Cars. *Opt. & Pho. News* 29, 26-33 (2018).

[168] T. Fersch, R. Weigel, A. Koelpin, A CDMA Modulation Technique for Automotive Time-of-Flight LiDAR Systems. *IEEE Sen. J.* 17, 3507-3516 (2017).

[169] B. Luey, S.R. Davis, S.D. Rommel, D. Gann, J.D. Gamble, M.P. Ziemkiewicz, M.H. Anderson, R. Paine, A Lightweight, Cost-Efficient, Solid-State Lidar System Utilizing Liquid Crystal Technology for Laser Beam Steering for Advanced Driver Assistance. Apr 1, 9 (2017).

[170] G. Smolka, Market Trends in Automotive Lidar. *Pho. Media*, (2020).

[171] L. Zhang, X. Sun, W. Zhang, G. Wang, N. Feng, W. Zhao, Compact Optical Phased Array Using a Serial Grating Antenna Design. *arXiv* 1903.04573 (2019).

[172] M.J. Heck, J.F. Bauters, M.L. Davenport, J.K. Doylend, S. Jain, G. Kurczveil, S. Srinivasan, Y. Tang, J.E. Bowers, Hybrid Silicon Photonic Integrated Circuit Technology. *IEEE Jour. of Sel. Top. in Quan. Elec.* 19, 610011 (2013).

[173] J.A. Zuclich, D.J. Lund, B.E. Stuck, Wavelength Dependence of Ocular Damage Thresholds in the Near-IR to Far-IR Transition Region: Proposed Revisions to Revisions to MPEs. *Heal. Phys.* 92, 15 (2007).

[174] W.R. Davis, J. Wilson, S. Mick, J. Xu, H. Hua, C. Mineo, A.M. Sule, M. Steer, P.D. Franzon, Demystifying 3D ICs: The Pros and Cons of Going Vertical. *IEEE Des. and Test of Com.* 5, 498 (2005)

[175] A. Dewanjee, J.N. Caspers, J.S. Aitchison, M. Mojahedi, Demonstration of a Compact Bilayer Inverse Taper Coupler for Si-Photonics with Enhanced Polarization Insensitivity. *Opt. Exp.* 24, 28194 (2016).

[176] T. Dirk, P. Bienstman, Roel Baets, Compact efficient broadband grating coupler for silicon-

on-insulator waveguides. *Opt. Lett.* 29, 2749 (2004).

[177] S. Tarun, J. Wang, B.K. Kaushik, Z. Cheng, R. Kumar, Z. Wei, X. Li, Review of recent progress on silicon nitride-based photonic integrated circuits. *IEEE Access* 8, 195436 (2020).

[178] X. Chao, W. Jin, J.E. Bowers, Silicon nitride passive and active photonic integrated circuits: trends and prospects. *Pho. Res.* 10, A82 (2022).

[179] J. Bowers, T. Komljenovic, M. Davenport, J. Hulme, A. Liu, C. Santis, A. Spott, S. Srinivasan, E. Stanton, and C. Zhang, Recent advances in silicon photonic integrated circuits. *Next-Generation Optical Communication: Components, Sub-Systems, and Systems V* 9744, 977402 (2016).

[180] Q. Hao, Y. Yang, Y. Wang, D. Lei, X. Fu, Q. Ren, X. Xu, Q. Luo, G. Xing, C. Chen, X. Si, H. Wu, Y. Yuan, Q. Li, X. Li, X. Wang, M. Chang, F. Zhang, and M. Liu, "A Computing-in-Memory Macro based on Three-Dimensional Resistive Random-Access Memory," *Nat. Elec.* 5, 1-9 (2022).

[181] W. D. Sacher, J. C. Mikkelsen, Y. Huang, J. C. C. Mak, Z. Yong, X. Luo, Y. Li, P. Dumais, J. Jiang, D. Goodwill, E. Bernier, P. G. Q. Lo, and J. K. S. Poon, "Monolithically integrated multilayer silicon nitride-on-silicon waveguide platforms for 3-D photonic circuits and devices," *Proc. of the IEEE* 106, 2232-2245 (2018).

[182] F. Ashtiani, and F. Aflatouni, "2-D Optical Phased Arrays with Multilayer Antenna Elements and Off-Aperture Phase Control." *CLEO: Sci. and Inno.*, pp. STh2G-2, (2022).

[183] T. Bibby, and K. Holland, "Endpoint detection for CMP," *Jour. of Elec. Mat.* 27(10), 1073-1081 (1998).

[184] Z. Qu, Q. Zhao, Q. Yu, D. Zhao, H. Li, X. Lu, and Y. Meng, "Cu layer thickness monitoring in CMP process by using eddy current sensor," *ICPT 2012-Inter. Conf. on Plan. /CMP Tech.*, (2012)

[185] LNF wiki – SPR 220, https://lnf-wiki.eecs.umich.edu/wiki/SPR_220#3.C2.B5m_-_SPR_220_.283.0.29.